Modeling and Simulation of Grid-connected Superconducting Wind Turbine Generators

Loïc Quéval

Department of Advanced Energy

The University of Tokyo

A thesis submitted for the degree of

Doctor of Science

December 12th, 2012

Acknowledgements

Firstly, I would like to express my utmost gratitude to my supervisor, Prof. Hiroyuki Ohsaki, for his confidence, advice, guidance and constant support during this research. He always gave me the freedom to explore my own ideas, whilst ensuring that I reach the goal of my research on time.

I would also like to thank Prof. Masaki Sekino for his many suggestions, informative discussions and appropriate criticism. And the members of Ohsaki laboratory for welcoming me into their group.

I am extremely grateful to those who have shared openly their technical expertise: Dr. Yutaka Terao for providing the data for the generator designs in this thesis ; and Dr. Victor Rodriguez-Zermeno and Dr. Mark Ainslie for their assistance with HTS tape numerical modeling.

I should also mention that this work was supported by The University of Tokyo and the Japanese Government (Monbukagakusho: ministry of education, culture, sports, science and technology).

Finally, I must thank all of my friends and family for their love and support.

Abstract

Superconducting machines have been proposed to solve the problem of upscaling wind turbine generators. In order to design such machines, since prototyping would be very expensive, it is crucial to be able to simulate the interactions between them and the external systems. Within this framework, this thesis addresses the problem of modeling and simulating grid-connected superconducting wind turbine generators.

The adopted method is a multiscale simulation constituted by three models with unidirectional couplings: the wind energy conversion system model, the machine model and the HTS tape model. The multiscale simulation allows us to obtain the desired level of accuracy, while the unidirectional couplings bring high efficiency. The models are implemented in a flexible way using commercial softwares (Matlab/Simulink and Comsol Multiphysics), a key to bringing development of superconducting machines from the laboratory scale to the industrial level.

The wind energy conversion systems model includes the direct-drive superconducting generator, the power converter, the external mechanical systems, the external electrical circuits and associated control strategies. Considering special requirements of offshore superconducting machines, we adopt a back-to-back converter, and summarize the equations for its dimensioning and systematic control.

To model the superconducting machine, we use a nonlinear coupled finite element phase-domain model. Its main advantage is to provide a reasonable simulation speed with the same accuracy as a full finite element model. On the one hand, the machine is represented by a

nonlinear phase-domain model that can naturally include both space harmonics and saturation, two important features of multi-MW superconducting wind turbine generators. On the other hand, the machine parameters are obtained from static nonlinear finite element analysis. We present and validate a novel general derivation and flexible implementation of this model using N-dimensional lookup tables.

The HTS tape model is a finite element model of only one tape with H-formulation and edge elements. It takes into consideration the properties and the real thickness of the tape.

Finally, we demonstrate the versatility of the adopted method by simulating 10 MW class grid-connected superconducting wind turbine generators. The analysis focuses on estimating critical parameters for the design of the machine such as resulting torque, transient current margins, and steady-state AC losses. The estimations include effects linked to the turbine inertia, the shaft stiffness, the generator space harmonics and saturation, the exciter control, and the AC/DC/AC converter PWM and control.

Contents

List of Figures

Chapter 1

Introduction

1.1 Motivation

Although wind energy had an average growth rate of 25% between 2006 and 2011 and a production of around 583 TWh in 2011, it still represents only 3.5% of the world electricity supply. Reference scenarios estimate that the wind energy production should reach 4264 TWh to 12651 TWh by 2050 according to policies adopted by the governments to regulate their release of CO_2 (Fig.1.1). Therefore, even the lowest estimation, corresponding to the IEA's "New Policies Scenario", predicts the need to multiply wind energy production by 7.3 by 2050 [1; 2].

Against this background, offshore wind farms have recently drawn the attention because of their numerous advantages: constant winds, location in large deserted areas, and insignificant visual impact. Those farms currently under construction have an average turbine size of 3.2 MW with a significant number of 5 MW turbines [3]. Following the UpWind project [4], multi-MW wind turbine generators are especially desirable as the cost of the wind turbine is only about one quarter of the wind farm lifecycle cost, with installation and yearly operation and maintenance being the other major costs (Fig.1.2).

The most popular configurations for variable speed multi-MW wind energy conversion systems (WECS) are partial-scale power converter with doubly-fed induction generator (DFIG), and full-scale power converter with direct-drive synchronous generator (DDSG). DFIG is currently the mainstream technology in the

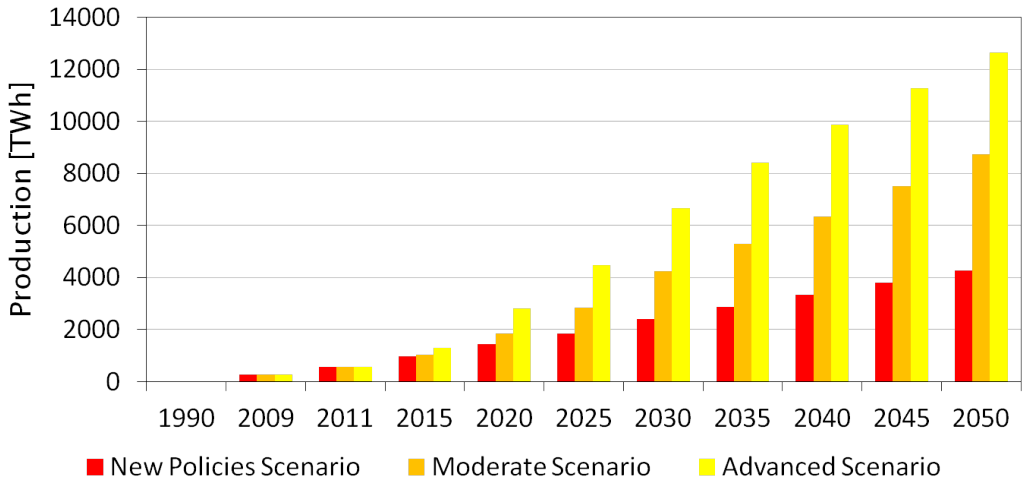

Figure 1.1: World wind electricity production [1; 2].

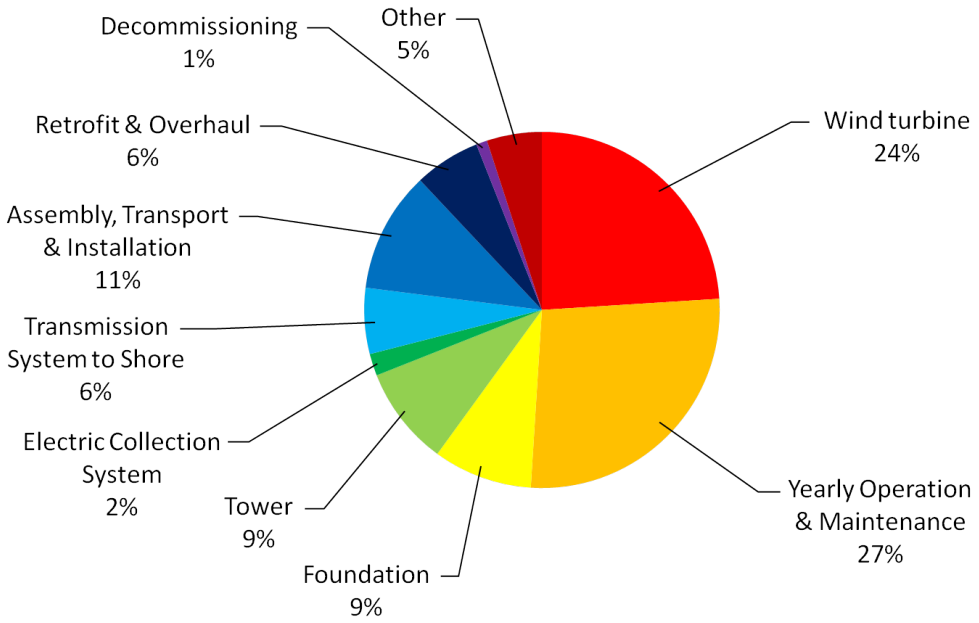

Figure 1.2: Lifecycle cost breakdown of the 500 MW DOWEC reference offshore windfarm [5].

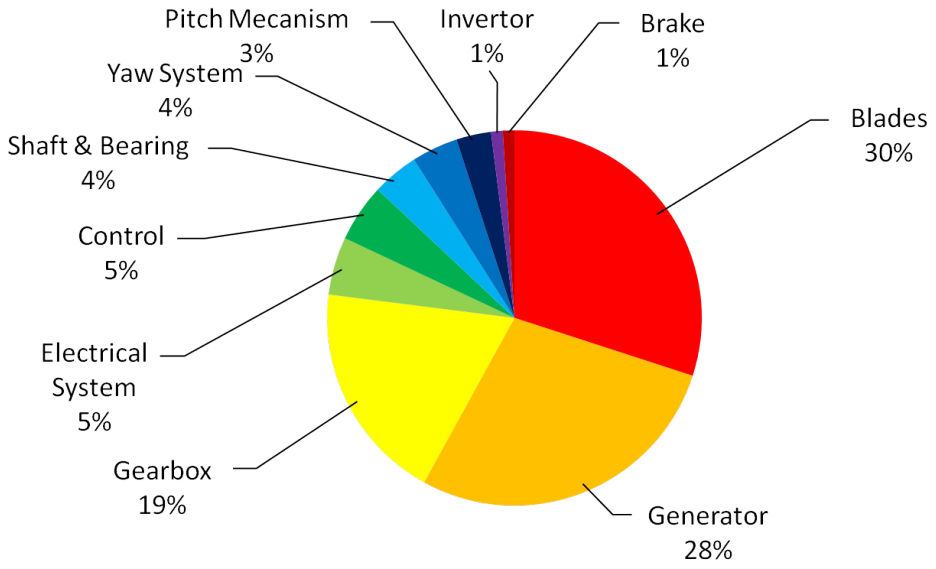

Figure 1.3: Yearly operation & Maintenance cost breakdown of the 500 MW DOWEC reference offshore windfarm [6].

market for large wind turbine generators (WTG), largely thanks to the fact that the power converter rating is only about 25% of that of the generator. However, its use may be limited in the future due to difficulties to comply with grid-fault ride-through requirements and reliability problems associated with the gearbox (Fig.1.3) [19]. DDSG is considered as a promising technology for multi-MW offshore WECSs. It has no gearbox, and thus it has high efficiency, high reliability, as well as low installation and maintenance costs. In addition, the full-scale converter provides satisfactory low-voltage ride-through capability. On the other hand, multi-MW DDSGs tend to be large and heavy (Fig.1.4) [19]. This can be problematic if planning to install them on floating foundations in deep water areas [56].

High temperature superconducting (HTS) machines have been proposed to solve this problem [47; 56; 68]. Indeed the high magnetic field density produced by superconducting coils can provide a more lightweight and compact design than what can be done with copper coils, permanent magnets and magnetic iron [69; 76].

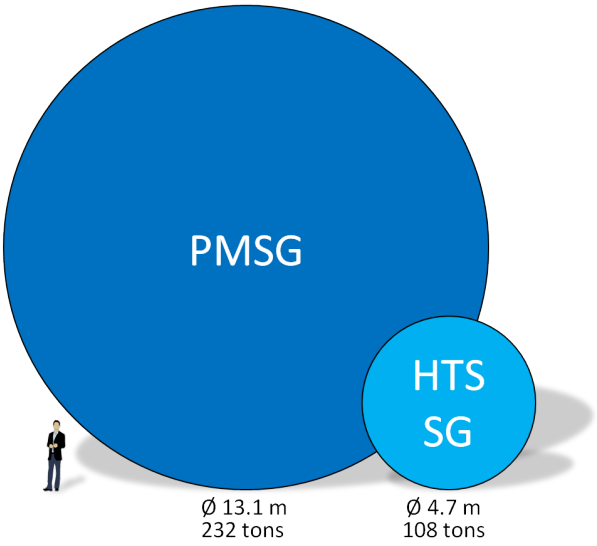

Figure 1.4: Size comparison of 10 MW class permanent magnet and HTS DDSG [76].

Within this framework, distinctive aspects of superconducting wind turbine generators design should be emphasized:

Lack of experience: The designer might face a lack of experience when considering superconducting machines design. First, such machines have particular designs and highly nonlinear materials [81; 82]. As a consequence, one cannot always rely on conventional machines design methods or empirical values. Secondly, because of the cost of HTS machine prototype development, there is a lack of experimental data [83]. It is then difficult for designers to estimate critical parameters such as resulting torque, transient current margins, or steady-state AC losses. But advanced simulations could provide some guidelines.

Integrated design: Various superconducting wind turbine generator designs have been proposed [47; 48; 55; 56]. But these studies mainly focus on the electromagnetic properties of the machine. They do not consider the external mechanical systems (blades, shaft), the external electrical systems (exciter, power converter), the control strategies, or the operating conditions (wind turbulence, grid fault). Therefore the generator is always designed

as an isolated system, operating under ideal conditions. But in reality, the machine interacts with external systems. It is integrated to the rest of the power network. And only few efforts have been made to study the grid integration of superconducting wind turbine generators, or more generally superconducting machines. Lewis and Mueller [47] mentioned of a grid-connected superconducting wind turbine generator simulation to study the influence of wind turbulence on rotor losses. Kim *et al.* [48] simulated a grid-connected 10 MW class superconducting wind turbine generator under slow wind variations only. Sivasubramaniam *et al.* [57] investigated losses of a 100 MVA HTS generator field coil resulting among others from the AC ripple from the exciter. Mijatovic *et al.* [49] addressed on a general level AC losses in wind turbines applications resulting from field PWM modulation and wind turbulences. Sivasubramaniam *et al.* [50] analyzed the field coil thermal transient response of a 100 MVA HTS generator connected to the grid through a step up transformer. Hence, a model which studies the interactions between superconducting machines and external electrical or mechanical systems would be a precious tool for system designers.

1.2 Aim of the thesis

Considering the need for superconducting machine designers of an accurate, efficient and flexible tool to study the interactions between the machine and external systems, the objective of this thesis is to develop a numerical model for the steady-state and transient analysis of grid-connected superconducting wind turbine generators.

1.3 Issues

1.3.1 Multiscale system simulation

The modeling of grid-connected superconducting wind turbine generators is complex because of its multiscale nature. On the one hand, the wind turbine of a 10 MW wind energy conversion system is 180 m in diameter, whereas the super-

conducting tape is only several micrometers in thickness. On the other hand, the time constant of the mechanical parts of the system is a few seconds, whereas the switching frequency of the power converter is several kilohertz. A multiscale simulation can provide an accurate yet efficient way to simulate such a complex system. It would use multiple models at different scales with different level of detail to describe the whole system.

Therefore, the system decomposition, the level of detail of each model and their couplings should be defined depending on the simulation goals.

1.3.2 Superconducting coil model

HTS machine windings modeling is challenging because of the nonlinear characteristics and high aspect ratio of the tapes used. But recent efforts made it possible to simulate those materials under a wide range of operating conditions in commercial FEM softwares [58; 59]. Another obstacle arises when considering that multi-MW machines require several thousand turns of superconducting tapes. We underline that the computation of a stack of several hundreds of tapes is to be avoided because of the prohibitively high number of element required and because of the overlong computation time. Note that various promising mathematical methods have been proposed to calculate AC losses of a stack of hundreds of tapes [60; 61; 67]. But as they introduce additional assumptions, it should be made clear whether they can be applied to an array of tapes. Therefore they are not considered further.

Therefore, an effective way to simulate superconducting coil wound with several thousand turns of HTS tapes should be introduced.

1.3.3 Superconducting offshore WECS design

Power electronics systems for the grid integration of conventional wind turbine generators have been extensively discussed for both onshore and offshore applications [9; 14; 19; 24; 42; 43; 44; 62]. But, little effort has been made to our knowledge to study if state-of-the-art conversion systems developed for conventional wind turbines are suitable for multi-MW offshore superconducting wind turbine generators.

Therefore, power electronics for the grid integration of superconducting wind turbine generators should be discussed.

1.3.4 Back-to-back converter design and control

Because of requirements for superconducting generators and offshore systems, we will adopt a back-to-back power converter for the grid connection (see section 2.3.1). When considering the design and control of such a converter, one might be confused by the absence of design guidelines and reference model. Indeed detailed modeling, simulations and field tests of such a system have been reported by various authors [14; 15] but no indication could be found on how to choose the value of the converter components. Besides, many approaches have been proposed for the design of voltage source converters [13; 16] but most of them have no direct link to back-to-back converters, or wind energy conversion. Finally, we found only sparse information on the systematic determination of the PI parameters for the converter controller [18]. This makes it difficult to compare different systems, especially as controller parameters can have a great influence on the dynamic of the system.

Therefore, system designers can benefit from a step-by-step method for the systematic design and control of back-to-back converter for direct-drive electrically-excited synchronous generator-based WECS. It would directly contribute to speed up the development process of superconducting wind turbine generators.

1.3.5 Superconducting machines modeling

When considering time domain transients simulation of grid-connected superconducting machines, a fundamental problem is the choice of the machine model. It should notably be able to capture the machine characteristics with the required precision.

Therefore, it should be clarified which machine model should be used in time domain transients simulation to represent superconducting machines with accuracy.

1.3.6 Nonlinear phase-domain model implementation

Because of superconducting machine design pecularities, we will model the superconducting generator with a nonlinear coupled finite element phase-domain model (see section 2.3.4). The implementation of the phase-domain model can be quite challenging because of the varying inductance matrix, as well as the preliminary calculation, the storage and the handling of its parameters [32; 34; 35].

Therefore, there is the need to develop a simple nonlinear phase-domain model that could represent naturally and accurately superconducting machines features.

1.4 Proposed method

The proposed method is a multiscale simulation constituted by three models with unidirectional couplings as shown on Fig.1.5.

The first model is the wind energy conversion system (WECS) model. This is a lumped-parameter model implemented in Matlab/Simulink with the SimPowerSystem toolbox. It includes the superconducting generator, the external mechanical systems, the external electrical circuits and associated control strategies. We model the superconducting synchronous machine using a novel nonlinear coupled finite element phase-domain model. The inputs of this model are the WECS parameters and the operating conditions (wind, grid voltage, etc.).

The second model is the machine model. This is an A-formulation 2D finite element model of the machine. It does not take into consideration the properties or the geometry of the superconducting tapes. The inputs of this model are the HTS machine parameters, the HTS machine geometry and the WECS model simulation results.

The third model is a HTS tape model. This is an H-formulation 2D finite element model of only one superconducting tape. It takes into consideration the properties and the actual geometry of the superconducting tape. The inputs of this model are the HTS tape properties, the HTS tape geometry and the machine model simulation results.

These three models allow us to estimate the steady-state and transient response for various operating conditions. We use them to determine operating

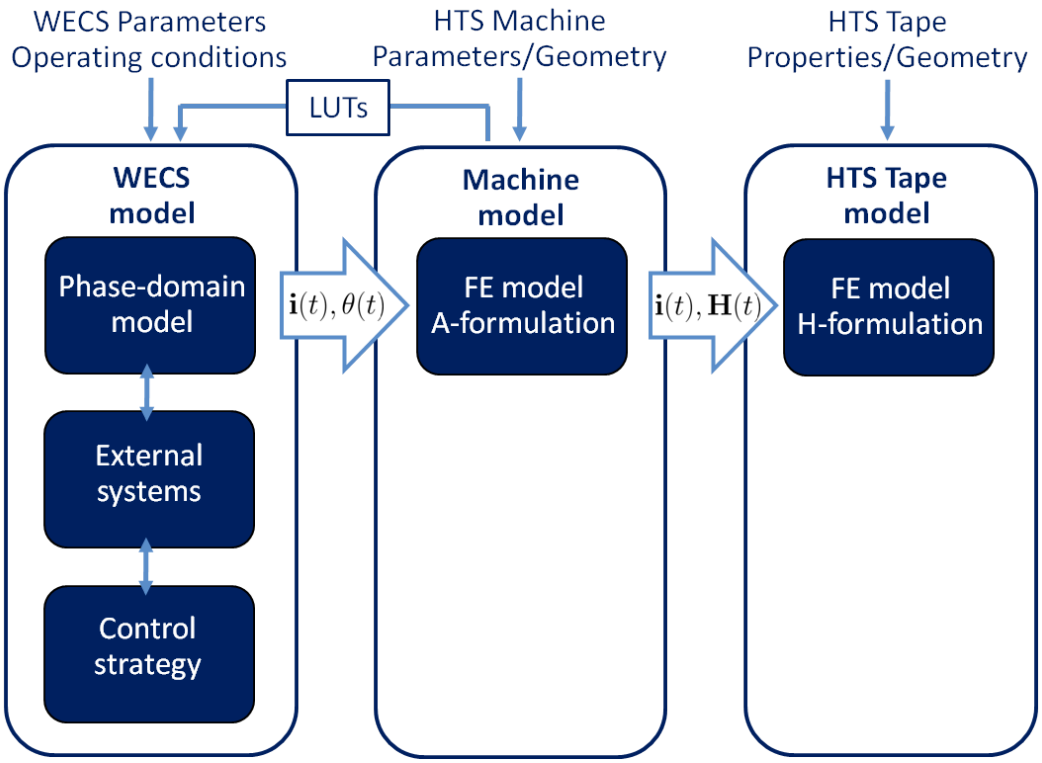

Figure 1.5: Overview of multiscale simulation.

characteristics such as resulting torque, transient current margins, and steady-state AC losses.

1.5 Outline of the thesis

This thesis is structured in four chapters. Chapter 2 introduces the adopted multiscale simulation. We underline the key points for offshore superconducting WECS design, and for superconducting machines modeling. We describe in detail the three models of the multiscale simulation: the wind energy conversion system model, the machine model, and the HTS tape model. And we discuss how they are coupled. Chapter 3 summarizes equations for the dimensioning and control of the adopted WECS. And we simulate a WECS using a 2 MW conventional generator that will be used as a reference model. Chapter 4 describes the machine nonlinear coupled finite element phase-domain model. We introduce the phase-

domain model and we report on its implementation with N-dimensional lookup tables. We build a coupled finite element phase-domain model. And we show how to calculate the phase-domain model parameters by finite element analysis. Finally, chapter 5 presents simulation and analysis of grid-connected 10 MW class superconducting wind turbine generators. We estimate the machine resulting torque, the transient current margins, and the steady-state AC losses.

Chapter 2

Multiscale simulation

Objectives: Introduce a multiscale simulation for the steady-state and transient analysis of grid-connected superconducting wind turbine generators.

Motivations: Need for an accurate, efficient and flexible tool aiming at studying the interactions between superconducting machines and external systems (see section 1.1 and 1.3.1). Lack of previous discussion about the power electronics required for the correct operation and optimal grid integration of offshore superconducting WECS (see section 1.3.3). Lack of previous discussion about which machine model should be used to represent with accuracy superconducting machines in time domain transient simulations (see section 1.3.5). Need for an effective way to simulate superconducting coils wound with a large number of tapes (see section 1.3.2).

Contributions: Development of a multiscale simulation for electrical machines with unidirectional couplings. Discussion on the design of superconducting offshore wind energy conversion systems. Discussion on the modeling of superconducting machines.

2.1 Overview

The proposed method is a multiscale simulation constituted by three models with unidirectional couplings: the wind energy conversion system model, the machine model, the HTS tape model. An overview of the multiscale simulation is shown in Fig.1.5.

2.2 Key points for design and modeling

To be relevant, each model should be build keeping in mind the system main characteristics. We detail bellow the key points for the design and modeling of offshore superconducting wind turbine generators.

2.2.1 Key points for superconducting WECS design

2.2.1.1 Losses in the cold parts

Heat loads from AC currents and fields is an important factor for superconducting electrical machines design and operation. Indeed losses in the cold parts are, because of the efficiency of the cooling system, amplified by a factor from 50 up to 1000 for temperatures in the 80 K-20 K range [51]. Because of AC losses in the superconductors, superconductors are mainly used in synchronous generators for the DC field winding. But even if the field winding carries nominally DC current, significant AC currents and fields are introduced during steady-state operation. This has been underlined by various authors. Lewis and Mueller [47] discussed AC losses in superconducting wind turbine generators caused by wind turbulences. Sivasubramaniam *et al.* [57] investigated losses of a 100 MVA HTS generator field coil resulting among others from the AC ripple from the exciter. Mijatovic *et al.* [49] addressed on a general level AC losses in wind turbines applications resulting from field PWM modulation and wind turbulences.

To show the influence of the power converter on the field current, we simulate the steady-state operation of a conventional WECS. The system overview is shown on Fig.2.1. The generator is a conventional 2 MW/60 Hz synchronous machine (Appendix B). The AC/DC/AC converter has a diode bridge rectifier

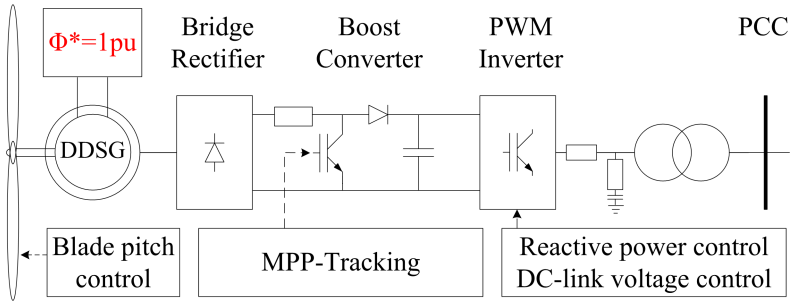

Figure 2.1: Conventional WECS with diode bridge rectifier.

in the generator side and a PWM inverter in the grid side [19]. Note that both Enercon and Britannia 10 MW WECS have adopted this kind of converter. Besides to guaranty the optimal conditions of operation, the field current of the conventional machine is regulated so that the resultant airgap flux remains at 1 pu during normal operation with flux weakening for overspeed operation [54]. The control design implemented is similar to the one used for existing multi-MW wind turbines [19]. Simulated field AC currents frequencies and magnitudes normalized by its DC value are summarized in Table 2.1. We underline that AC fields should be taken into account too for AC losses calculation, but they cannot be estimated with the considered lumped parameter model. Nevertheless, this illustrates the importance of choosing an appropriate converter topology and control strategy that can help to keep AC losses as low as possible in the superconductor and cold parts of the generator.

2.2.1.2 Quench

During fast transients, the field coil peak current can be much higher than the steady-state current. This could result in a coil quench and a thermal run away. Sivasubramaniam *et al.* [50] underlined this point by analyzing the field coil thermal transient response of a 100 MVA HTS generator connected to the grid through a step-up transformer. But variable-speed synchronous machine-based WECS are connected to the grid through full-scale converters. Therefore, we simulate here again the system introduced in section 2.2.1.1 during a grid voltage drop from 1 pu to 0 pu during 0.5 s. The field current variation is shown on Fig.2.2. It is observed that field current is not tightly kept to its nominal value. To

Table 2.1: Field winding AC currents of conventional wind turbine generator

Source	Frequency / Magnitude
Diode rectifier	360 Hz / 6.4 %
	720 Hz / 1.0 %
	1080 Hz / 0.6 %
	1440 Hz / 0.4 %
	1800 Hz / 0.3 %
	2160 Hz / 0.3 %
	2520 Hz / 0.3 %
	2880 Hz / 0.2 %
	3240 Hz / 0.2 %
DC/DC converter	2000 Hz / 0.2 %

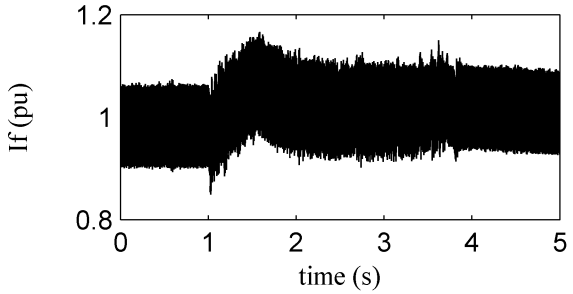

Figure 2.2: Conventional WTG field current during grid voltage dip.

prevent quench, superconducting coils are usually designed with enough current margin to ride through the overcurrent without going normal. But because of the high price of HTS tape, the converter should be able to limit the overcurrent in the superconductors in case of fault.

2.2.1.3 Mechanical vibrations

Since HTS is produced as a rather rigid and brittle tape, only simple geometry coils (pancake coils, racetrack coils) can be manufactured with the present technology and provide the necessary strength and protection for the superconductor in rotating applications. Besides, typical superconducting generators are air-cored with armature windings supported by non-magnetic material [55; 56]. With these constraints, the airgap flux distribution has significant space harmon-

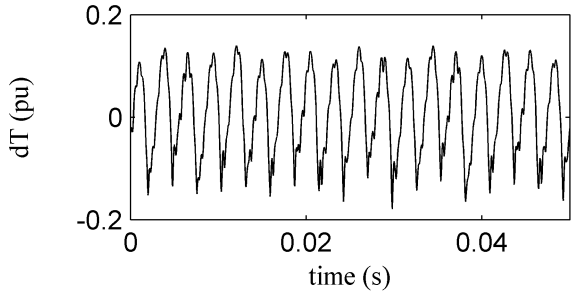

Figure 2.3: Conventional WTG resulting torque in steady-state operation.

ics. As the flux in superconducting machines is much larger than in conventional machines, space harmonics could be a source of mechanical vibrations. Mijatovic *et al.* [49] investigated tendency of HTS synchronous machine towards mechanical oscillations caused by space harmonics. Another source of mechanical vibration can be the time harmonics injected by the generator-side converter on the stator side. The resulting torque acting on the shaft of the machine in steady-state operation for the system introduced in section 2.2.1.1 is shown on Fig.2.3. Note the 360 Hz resulting torque pulsation as a consequence of the use of the diode bridge rectifier. Therefore, an adapted converter topology is required to ensure good machine performance.

2.2.1.4 Low synchronous reactance

From the electrical point of view, the biggest difference between conventional and air-cored HTS synchronous generator suited for wind turbines is the low value of the synchronous reactance of a superconducting generator. It is typically 2 to 20 times lower than the one of a conventional machine [49]. If this is an advantage for control purpose, this could amplify the torque ripple observed above or lead to very high forces during fast transient that could damage the mechanical system.

2.2.1.5 Low output electrical frequency

Conventional direct-drive wind turbine generators have a high number of pole pairs. But usually this is not the case in superconducting wind turbine generators where a small pole pitch would result in important flux leakages due to the

relatively large air gap. Therefore non-salient pole superconducting wind turbine generators have generally between 8 and 30 poles [55; 56; 76]. Moreover they operate at low speed because of the direct-drive concept, usually around 10 RPM. The output electrical frequency is therefore approximately 1 Hz. Such a low operation frequency could lead to a thermal cycle of the switches that should therefore be chosen adequately. Further considerations are out of the scope of this thesis.

2.2.1.6 Cooling power

The operating temperature has to be kept under the superconductor critical temperature. The power required for the cooling system is normally supplied by the wind farm. Therefore the system must be able to provide power for the cooling of the superconducting windings even during no wind conditions.

2.2.2 Key points for offshore WECS design

We detail the key points for the design of offshore wind energy conversion systems.

2.2.2.1 Size and weight

A constraint that must be addressed in any offshore electrical installation include limited size and weight. A small and lightweight nacelle can be transported and lifted to the tower in one piece. It allows savings in the cost of the tower, of the foundation/platform, and of the installation [56]. Then power electronics and generator should be as compact and lightweight as possible.

2.2.2.2 Reliability and survivability

When a power electronics device failure occurs, it usually requires tripping the converter and then isolating it from the grid to avoid further serious damages. For offshore installations, it might stop the electricity production for a considerable time until the weather conditions permit a repair. Such a standstill is very costly. Besides, offshore repairs are extremely expensive and difficult. With these constraints, the requirement of reliability and survivability of the system is very

important. This is usually achieved by redundancy of the critical systems. For the same reasons, long maintenance intervals are desirable.

2.2.2.3 Grid codes

In the future, large wind farms are expected to represent a significant contribution to the grid, and therefore their impact on the operation and performance of the network becomes more and more significant. Consequently, new grid codes have high technical demands for them, such as frequency and voltage control, active and reactive power regulation, and quick responses under power system transients. For example, a restrictive requirement is the low-voltage ride-through (LVRT) capability. It implies that when the voltage at the grid coupling point drops but stays above the line shown on Fig.A.1, the wind turbine generator must stay on line, ride through the fault, and be able to take full rated field current when the fault is cleared. The WECS design should allow operation to meet grid code requirements.

2.2.3 Key points for superconducting machine modeling

We detail the key points for the modeling of superconducting machines focusing on multi-MW superconducting wind turbine generators.

2.2.3.1 Space harmonics

Space harmonics are the harmonics of the airgap flux distribution. They are linked to the magnetic circuit geometry: discrete nature of the windings, slotting, saliency, windings fractional pitch, stator phase windings asymmetry, etc. They generate unwanted effects including losses in the rotor/stator magnetic cores [73], and noise/vibrations [72; 74].

For conventional machines, the space harmonics mitigation is usually achieved by two techniques: magnetic iron shape optimization [73], and distributed windings [72; 74]. In addition, advanced mitigation techniques can be applied [75]. For superconducting machines, the space harmonics mitigation strategy depends on the design concept.

Superconducting generators without magnetic material [55]: This design has been proposed because the superconducting field windings can produce airgap magnetic fields over 2 T without magnetic iron. It allows a reduction of the machine weight by eliminating the magnetic iron [78]. And the efficiency is increased by removing the core losses. With this concept design, the airgap flux distribution has significant space harmonics (Fig.2.2.3.1), and magnetic iron shape optimization cannot be used. One possibility could be to optimize the shape of the superconducting coil itself [77]. But since HTS is produced as a rather rigid and brittle tape, and since the magnetic forces will act directly on the coil, only simple geometry coils (pancake or racetrack coils) can be manufactured with the present technology.

Superconducting generators with magnetic material [56; 76]: This design allows a reduction of the required superconductor tape length. Another advantage is that the magnetic core shape could be optimized to reduce the space harmonics. But considering the high forces at play in multi-MW direct-drive machines, such an optimization might be limited.

Fully superconducting generators [76]: This design has been proposed to further reduce the size and weight of the generator. Above considerations apply to those machines too. In addition, the stator windings design is limited by the mechanical properties of the superconducting windings. It might be difficult to use distributed windings in this case.

Besides, as the flux in superconducting machines is much larger than in conventional machines, space harmonics could be a source of mechanical vibrations [49]. This effect could be amplified because of the low value of the synchronous reactance of a superconducting generator (refer to section 2.2.1.4).

To summarize, state of art space harmonics mitigation techniques for superconducting machines are limited, and synchronous machines may have a tendency towards mechanical oscillations. Therefore, a key point for superconducting machines modeling is to correctly include the space harmonics.

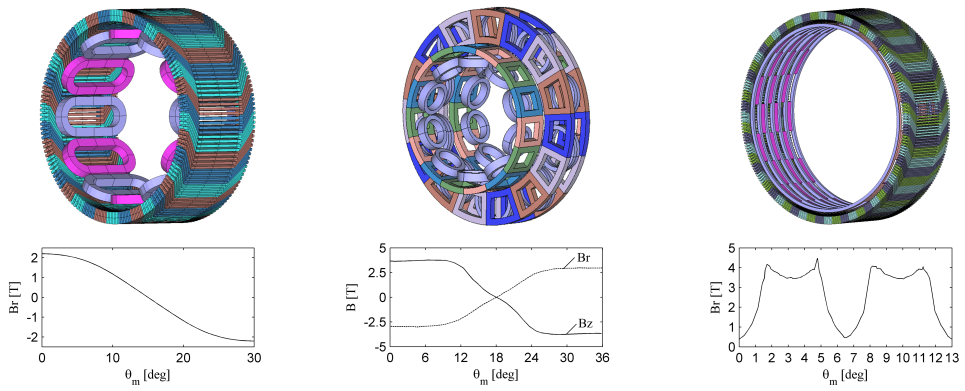

(a) Racetrack coil design [55] (b) Transverse flux [79] (c) Coils and bulk design [80]

Figure 2.4: Space harmonics of various air-cored superconducting generators.

2.2.3.2 Saturation

The magnetic flux density produced by the superconducting coil can be up to 9 T. Superconducting generators having a rotor core and/or magnetic teeths will therefore operate in the saturated region (Fig.2.2.3.2). The resulting cross-saturation can probably not be neglected under such operating conditions.

Therefore, a key point for superconducting machine modeling is to correctly include (cross-)saturation.

2.3 Wind Energy Conversion System Model

The wind energy conversion system model is a lumped-parameter model implemented in Matlab/Simulink with the SimPowerSystems toolbox. It includes the wind turbine, the drive-train, the electrically-excited synchronous generator, the exciter, the AC/DC/AC converter, the line reactor, the step-up transformer, and the associated control strategies.

2.3.1 WECS design

In sections 2.2.1 and 2.2.2, we underlined the key point for superconducting off-shore wind energy conversion design. Taking this into account, we design the

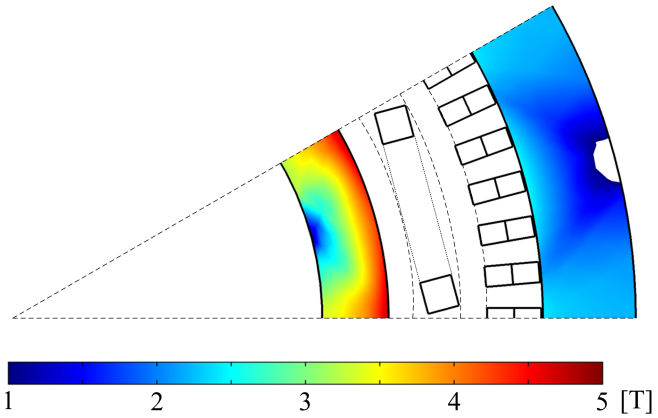

(a) Non-salient pole generator [76]

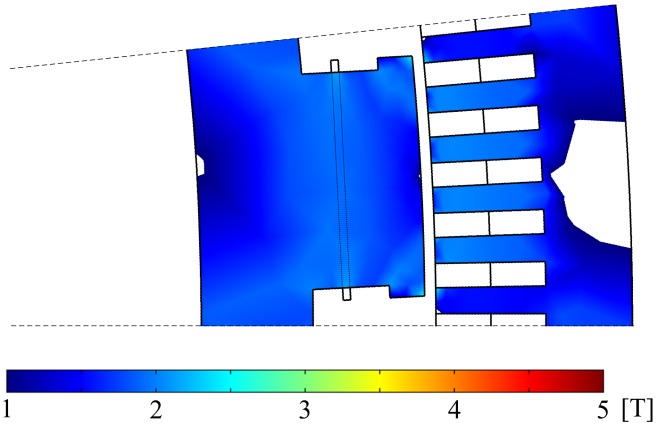

(b) Salient pole generator [76]

Figure 2.5: Saturation characteristics of various superconducting generators. The norm of the magnetic flux density is plotted only in the magnetic domains.

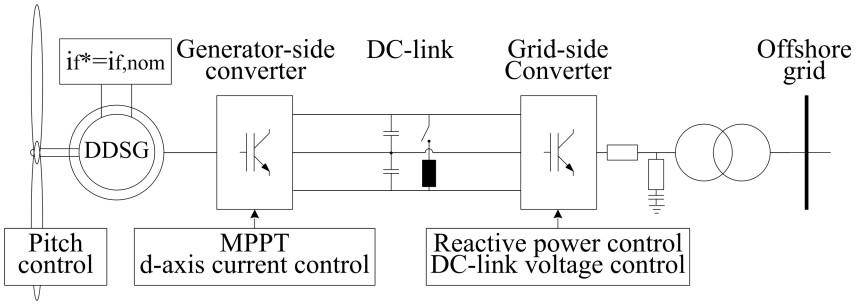

Figure 2.6: Overview of the WECS model.

wind energy conversion system. An overview of the adopted system is shown in Fig.2.6.

2.3.1.1 Preliminary considerations

The grid integration of offshore superconducting wind turbine generator is a serious challenge. Therefore successful grid integration of such machines will depend on the choice of reliable, existing technology. For this reason, even if they are promising solutions we didn't investigate: matrix converters, reverse-conducting IGBT, IGCT, or novel power converter topologies.

2.3.1.2 Drive train

To increase the reliability and the efficiency of the system, and to reduce the weight of the nacelle and the price of the installation (see section 2.2.2 and Fig.1.3), we adopt the direct-drive generator concept.

2.3.1.3 Field excitation

For conventional machines optimal operation, the field current is usually regulated so that the resultant air gap flux ϕ remains at 1 pu during normal operation with flux weakening for overspeed operation [54]. Other options are to use an automatic voltage regulator (AVR) to control the stator voltage, or to maintain a constant DC voltage [19]. But such excitation controllers induce unwanted field current variations or harmonics that can generate AC losses in the superconductor (see sections 2.2.1.1 and 2.2.1.2). Therefore, we choose that the exciter controls

the field current of the superconducting generator to its nominal value. It will help to reduce the AC losses in the superconductor while protecting the field coil from transient overcurrent [84].

2.3.1.4 AC/DC/AC converter

We underlined in section 2.2.1.1 that high magnitude low frequency harmonics can be injected on the generator-side and propagate through the air gap to the field winding when a diode rectifier is used. This would be inacceptable for superconducting field winding and therefore generator-side low frequency harmonics would have to be suppressed by bulky AC-filters. Considering offshore installation requirements in term of compactness (see section 2.2.2.1), we adopt a PWM voltage source converter (VSC) instead of the bridge rectifier on the generator side. It is more compact, generates lower total harmonic distortion in the generator side thus allowing us to remove the generator side filters and has a better controllability. The impact of the low magnitude high frequency harmonics injected on the stator side by the PWM inverter on the superconducting field winding will be evaluated by simulation (see section 5.3).

To connect the DC output of the generator-side converter to the offshore grid, we adopt a PWM voltage source converter. As the generator-side converter is a PWM converter too, this configuration is called a back-to-back converter.

The IGBT-based three-phase back-to-back 3-level neutral-point-clamped (NPC) converter topology is selected because it is currently the standard system for medium-voltage and high-power applications. The IGBTs are operated through pulse width modulation (PWM). We underline that WECS using this configuration are commercially available for medium-voltage applications up to 8 MW [19].

The DC-link capacitor needs to be protected from overvoltage during severe transients. For simplicity, we adopt a braking resistor similar to the one proposed by Conray *et al.* [24].

2.3.1.5 AC/DC/AC converter control

The converter control strategy should be compatible with the requirement for constant field current. This can be easily achieved by using the well-known zero d-axis control (ZDC) for the generator-side converter: if the field current is kept constant and the d-axis stator current reference is kept to zero, then the generator speed can be controlled via the q-axis. The grid-side converter should then be able to regulate the DC-link voltage to its rated value. Finally, to comply with grid codes, the grid-side converter should control the reactive power injected to the grid too.

2.3.1.6 Filter, line reactor and transformer

The WECS is connected through a line reactor and a step-up transformer to the offshore grid. The line reactor is used as protection and to filter high frequency harmonics generated by the grid-side converter. The step-up transformer is used for voltage conditioning and galvanic isolation. Additional LC filters can be used to reduce the harmonics injected to the grid. Such filters are out of the scope of this thesis.

2.3.1.7 Wind farm grid connection

In this section, we discuss the wind farm connection in order to justify our AC/DC/AC converter choice. But the wind farm is not simulated in this thesis. We simulate only one WECS connected to the offshore grid.

For an offshore wind farm with a rated capacity of 500 MW, consisting of 50x10 MW superconducting wind turbine generators, each generator is connected to an 110 kV/50 Hz offshore grid [52; 53] in star configuration through its own back-to-back converter and transformer (Fig.2.7). The offshore grid is finally connected to the 220 kV/50 Hz onshore grid [52; 53] by a 150 km long submarine VSC-HVDC transmission line with a rated voltage of 150 kV.

We consider and HVDC topology for the wind farm connection because superconducting wind turbines have been proposed primarily for large wind farms situated at more than 100 km from the shore. In the light of this, HVAC transmission systems are not adapted [44]. Besides even if VSC-HVDC has higher

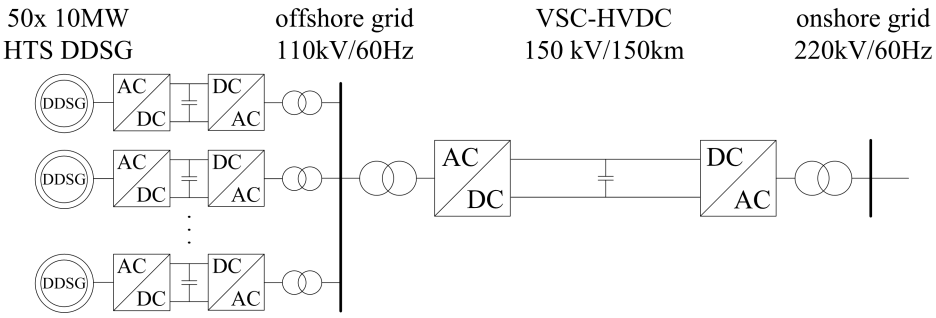

Figure 2.7: Single-line diagram of the 500 MW wind farm.
The wind farm is not simulated in this thesis.

cost, higher converter losses and lower maximal power rating per converter than LCC-HVDC, this is acceptable in view of its flexibility to provide no wind cooling power, to ensure grid code requirements, and in view of its smaller footprint and its suitability for multi-terminal systems [43; 44]. Finally, further developments are expected to improve VSC-HVDC systems.

Note that it seems that some redundancy is caused by using a full-scale converter for the generator and a VSC-HVDC for the transmission, as the AC/DC/AC conversion is performed twice. For this reason, Lu and Ooi [45] have proposed to connect in parallel the DC output of the generator side converters directly to the common HVDC bus. If this configuration permits to reduce the number of converters, it requires transformers between the stator and the generator side converter. If very low frequency output DDSG were used, the transformers would have prohibitively large cores. In order to increase the frequency, such interconnection would likely make use of generators with gearboxes in which case DFIG might be the most suitable option. Finally other configurations [46] can integrate the power conversion stages for machine control and high-voltage DC transmission. But issues, including machine-to-ground insulation or large scale DC/DC voltage transformation, need to be further addressed and thus they are not investigated further.

2.3.2 WECS modeling

In this section, we describe the modeling of the wind energy conversion system designed in section 2.3.1. The implementation is done with the Matlab/Simulink SimPowerSystem toolbox.

2.3.2.1 Wind

Wind speed varies in all time scales. Previous simulations [14] show that second-by-second wind effect can be neglected because of the large inertia of the wind turbine shaft H_{WT}. Indeed even if the wind fluctuates rapidly, the power P_m extracted is only a function of the average wind speed. Therefore, we model the wind as a constant with step variations.

2.3.2.2 Wind turbine

Detailed modeling of the wind turbine can be found in [24]. Usually, the wind turbine efficiency is controlled by a pitch angle control system to ensure that the extracted power P_{out} will not exceed the rated power P_{max} of the system. It could be used for load control [4] or low-voltage ride-through enhancement [24]. For simplicity, in this thesis, we set the blade pitch angle β constant to 0 degree.

2.3.2.3 Drive-train

Previous simulations [10] have shown that a one-mass drive train model gives significant errors when representing direct-drive wind turbine generators. Therefore, we use a direct-drive two-mass model drive train. Detailed modeling can be found in [71].

2.3.2.4 Generator

Two electrically-excited synchronous generator models are considered depending on the required precision.

Linear dq-model with saturation factors: The dq-model is available in the Matlab/Simulink SimPowerSystem toolbox. Its parameters are approximated by finite element analysis.

Nonlinear coupled FE phase-domain model: We discuss why we use this model in section 2.3.4. The model equations and implementation are described in details in chapter 4.

2.3.2.5 Exciter

The exciter is modeled with an ideal averaged voltage source. Its voltage is regulated by a PI controller as explained in section 3.2. A detailed model of the exciter is out of the scope of this thesis.

2.3.2.6 Back-to-back converter

Two back-to-back converter are considered depending on the required precision.

Averaged full WECS: We model both the grid-side and the generator-side converters with equivalent averaged 2-level voltage source converters. The generated AC voltage is averaged over one cycle of the switching frequency. It does not represent harmonics, but the dynamics resulting from control system and power system interaction is preserved. Therefore, the DC-link can be modeled by only one equivalent capacitor C. Its value is the same as the the two-level back-to-back converter capacitor (see Eq. 3.3).

Detailed half WECS: We model only the generator-side converter with a detailed three-phase three-level NPC converter consisting of 6 pairs of IGBT-diode. The DC-link is modeled by two DC voltage sources of $v_{dc}^*/2$ (see Eq.3.2).

2.3.2.7 Line reactor, filter and transformer

The focus of this thesis being the generator-side part of the system, the grid-side part of the system is modeled with a low level of detail. The line reactor is required for the grid-side converter control (see section 3.2). It is modeled with a RL load. The LC filters are not modeled. The step-up transformer windings configuration is Δ/Yg (Δ on high side) [26].

2.3.2.8 Offshore grid

The offshore grid is modeled by a programmable three-phase zero-impedance voltage source. We do not model the HVDC-link or the onshore grid.

2.3.3 WECS model parameters

WECS parameters are summarized in Table A.1. For the converter control, the machine dq-model parameters are obtained from the machine model (see section 2.4). The machines dq-model parameters can be found at Appendix C and D. The N-dimensional lookup tables for the phase-domain model are obtained from the machine model (see section 2.4) using formulas summarized in section 4.4. The machines phase-domain model data can be found at Appendix C and D.

2.3.4 Superconducting machine model choice

The choice of a machine model for time domain transients simulations is a trade-off between the speed of the simulation and the accuracy of the model.

A first option is to use a finite element model. In this case, it must be connected to external mechanical and electrical systems [7]. This method is accurate and well established, but it is computationally expensive.

A second option is to use the lumped-parameter dq-model [66]. It is well known, fast and often readily available in time domain transients simulation softwares. Space harmonics are usually neglected in the classical derivation of the dq-model [66]. The inductance matrix is then a sinusoidal function of the rotor angle. By using the qd0 transformation, we can transform this matrix into a constant one in the synchronous reference frame. Having a constant matrix, the dq-model is considered to be easy to implement, which explains its wide use [28]. Moreover, saturation is generally reintroduced in the linear dq-model with mathematical factors. But these factors neglect cross-saturation [37] and armature reaction [66]. When space harmonics and saturation cannot be neglected, the application of the qd0 transformation does not result anymore in a constant inductance matrix, and therefore offers little advantage.

A third option is to use the lumped-parameter phase-domain (PD) model, also

known as "abc-model". It can provide reasonable simulation speed with the same performance level as a full finite element model [33]. Its main advantage is that it can inherently take space harmonics and (cross-)saturation into account. Besides, because it is not necessary to use the qd0 transformation, its parameters are physical values and its derivation is straightforward. But, having rotor position and winding currents dependant coefficients, it is often considered to be harder to implement than the dq-model [28]. Moreover, the preliminary calculation, the storage and the handling of its parameters can represent additional complexity[32; 34; 35].

We underlined in section 2.2.3 that a key point for superconducting machines modeling is to correctly include both space harmonics and saturation. Therefore, we model superconducting machines using a phase-domain model. As the machine parameters are obtained from a nonlinear static finite element (FE) analysis, this model is called "nonlinear coupled FE phase-domain model". To cope with the implementation problems mentioned above, we present a novel general derivation and flexible implementation of this model using N-dimensional lookup tables in chapter 4.

2.4 Machine model

The machine model is a 2D finite element model with A-formulation rotating machinery model available with COMSOL Multiphysics AC/DC module. This model neither takes into consideration the actual conductor geometry nor the properties of the superconductor: the current density in the field coil is assumed uniform.

In this thesis, we use two different 10 MW class superconducting wind turbine generator designs.

Ironless generator [55]: It is an air-cored 10 MW/1 HZ class wind turbine generator with superconducting field windings and copper double layer distributed three-phase armature windings. Data can be found at Appendix C.

Non-salient pole generator [76]: It is 10 MW/1 HZ class wind turbine gen-

erator with inner iron core, back iron core, superconducting field windings and copper double layer distributed three-phase armature windings. Data can be found at Appendix D.

2.5 HTS tape model

The HTS tape model is a finite element model of only one tape with H-formulation and edge elements implemented with Comsol Multiphysics PDE mode application. This model takes into consideration the actual conductor geometry and the properties of the superconductor. Details on equations, implementation and comparison with analytical formulas can be found in [59]. Experimental validation is presented in [64; 65]. An overview of the HTS tape model is shown on Fig.2.5.

We consider that the machines field coils are wound with YBCO tapes of 4 mm in width and 0.1 mm in thickness [63]. We assume a packing factor of 0.5 and an insulation layer of 70 μm between two tapes. In the HTS tape model, we model only the HTS layer. It is 4 mm in width and 1 μm in thickness. The properties of the superconductor are modeled by a $E - J$ power law. We use E_0=1e-4 V/m. Generally, J_c and n both depend on the magnetix flux density magnitude and angle. For simplicity, we assume here that they are isotropic and constant. We set n=30 [64] and J_c=3.625e10 A/m^2 (I_c=145 A) [63].

2.6 Unidirectional couplings

First, we calculate the rotor mechanical angle θ_m, the stator currents i_{abc} and field current i_f with the WECS model. And we use them as constraints for the machine model (Fig.2.9). Secondly, we calculate the two components of the magnetic flux H_x and H_y with the machine model. And we use them as constraints, together with i_f, for the HTS tape model (Fig.2.10(b)). Thirdly, we solve the HTS tape model.

Ideally we would like to calculate the AC losses of all the tapes modeled in one coil model (Fig.2.10(a)). But such generators field coils are wound with a large number n_t of HTS tapes : 40204 tapes for the ironless generator, and 17625 tapes for the non-salient pole generator (see appendix D.4). Therefore, this is

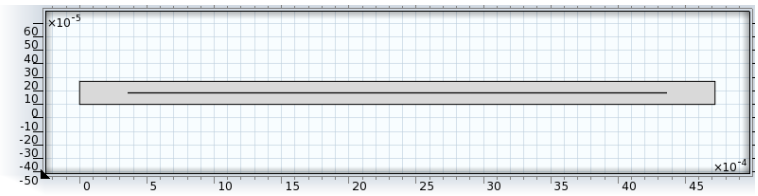

(a) Geometry

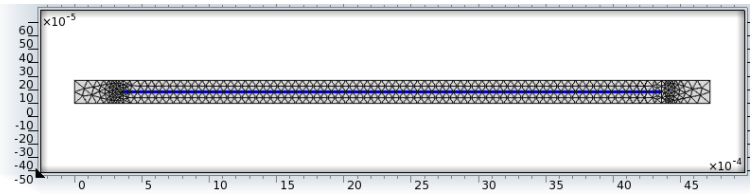

(b) Mesh

Figure 2.8: Overview of the HTS tape model.

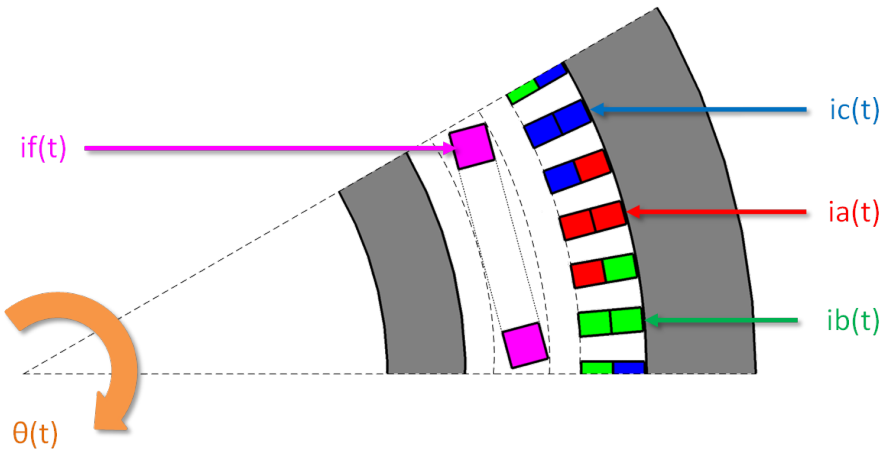

Figure 2.9: Coupling between the WECS model and the machine model.

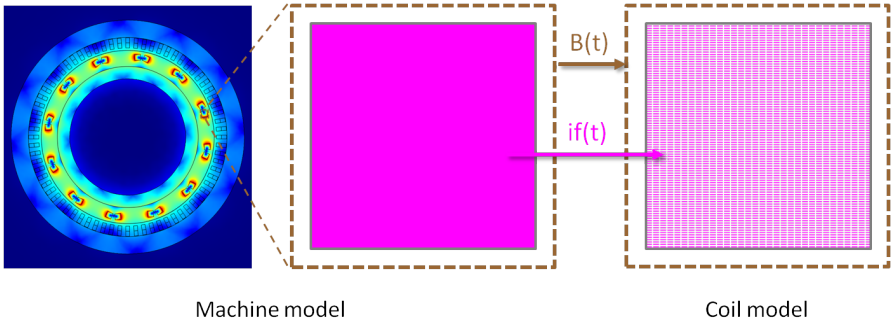

(a) Coupling with coil model

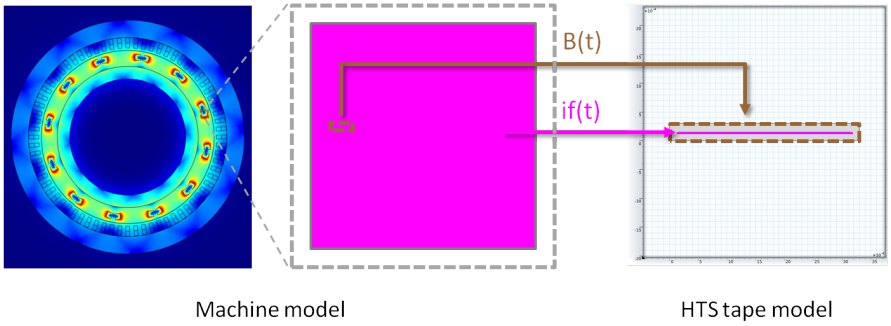

(b) Coupling with HTS tape model

Figure 2.10: Coupling between the HTS machine model and the HTS tape model. (a) Ideally we would like to use a coil model with a coupling boundary far from the coil edges. (b) But considering memory needs and computation time, we use an HTS tape model with a coupling boundary inside the coil and between the tapes.

not possible because the number of elements would be too high, requiring a very large memory. Instead of calculating one time n_t tapes, we propose to calculate n_t times the AC losses of one tape alone (Fig.2.10(b)). This approximation is discussed in section 5.3.3. Doing this, the number of elements per calculation can be kept low but the computation time is still very high. Therefore, assuming that neighboring wires have similar instantaneous AC losses, we calculate only $n_{t,0} < n_t$ times the AC losses of one tape alone, and we interpolate the results to the other $(n_t - n_{t,0})$ tapes. The $n_{t,0}$ tapes are selected arbitrarly. To do so, H_x and H_y are exported from the machine model along a coupling boundary lying at equal distance between the tapes. It is then applied to the HTS tape model as a time-varying Dirichlet boundary condition. An integral constraint is used to impose the total current in the superconducting tape i_t. It is equal to the superconducting coil current i_f divided by the number of tapes.

The unidirectional coupling between the WECS model and the machine model is a justified because the lumped-parameter nonlinear coupled FE phase-domain model used in the WECS model is a good representation of the machine model. Indeed, it can describe the machine characteristics with accuracy, including space harmonics and cross-saturation (see chapter 4). And therefore, a bidirectional coupling is not required. Note that the classical dq-model could be used for generators satisfying the hypothesis used to build the dq-model (no space harmonics, no saturation [66]).

The unidirectional coupling between the machine model and the HTS tape model would be fully justified if the coupling boundary were far from the superconducting coil [67]. But the fact that the coupling boundary is near the tape has a non-trivial effect on the estimated AC losses. This approximation is discussed in section 5.3.3.

2.7 Summary

In this chapter, we have underlined the key points for the design of an offshore superconducting wind energy conversion system. The design should notably be take into consideration: losses in the cold parts, quench, mechanical vibrations, low synchronous reactance, low output electrical frequency, cooling power, size

and weight, reliability and survivability, grid codes. From those considerations, we discussed an adapted power converter topology, excitation system and wind farm grid connection with their associated control strategies.

Then, we have underlined the key points for the modeling of superconducting machines. An accurate model should notably be able to correctly include both space harmonics and (cross-)saturation. Therefore, we proposed to use a coupled finite element phase-domain model.

Finally, we have introduced a multiscale simulation method for the study of grid-connected superconducting wind turbine generators. We considered unidirectional couplings between a wind energy conversion system model, an A-formulation machine FE model, and an H-formulation HTS tape FE model.

Chapter 3

WECS dimensioning and control

Objectives: Present a step-by-step method for the design and control of a full-scale back-to-back converter for variable speed wind turbine generators using direct-drive electrically excited synchronous machines.

Motivations: Absence of guidelines for the design and control of back-to-backconverter for synchronous generator-basedWECS (see section 1.3.4).

Contributions: Comprehensive step-by-step method for the design and control of a back-to-back converter for synchronous generator-based wind turbines, derivation of analytical formulas for the systematic determination of PI controller parameters, and definition of a WECS reference model.

3.1 WECS dimensioning

In this section, we dimension the wind energy conversion system modeled in section 2.3.2.

3.1.1 DC-link voltage

Each converter has to produce an AC voltage at least equal to the AC-side nominal voltage in order to properly control the injected AC-side current. Assuming an ideal converter with large frequency modulation ratio, naturally sampled sinusoidal PWM and a balanced system, the AC-side line-to-line RMS output voltage $v_{LL,RMS}$ is a function of the DC-link voltage v_{dc} and of the amplitude modulation ratio m,

$$v_{LL,RMS} = \frac{\sqrt{3}}{\sqrt{2}} m \frac{v_{dc}}{2} \tag{3.1}$$

with $0 \leq m \leq 1$. In order to keep low switching losses, it is desired to operate with a DC-link voltage as low as possible. But accounting for grid fluctuations, line reactor voltage drop and operation reliability, the reference DC-link voltage v_{dc}^* is chosen as,

$$v_{dc}^* = x \ \frac{2\sqrt{2}}{\sqrt{3}} v_{LL,RMS,max} \tag{3.2}$$

where x is an overvoltage factor, and $v_{LL,RMS,max}$ is the maximum between the grid and the generator nominal line-to-line RMS voltage. For low voltage system, x is 1.1. For medium voltage system, x is 1.15 [8; 12].

3.1.2 DC-link capacitor

The selection of the DC-link capacitor of a back-to-back converter is a trade-off between voltage ripple, lifetime and fast control of the DC-link voltage. Considering this, the DC-link capacitance C is chosen as [10],

$$C = \frac{S}{4\pi f_{min} \ v_{dc}^* \ \Delta v_{dc}} \tag{3.3}$$

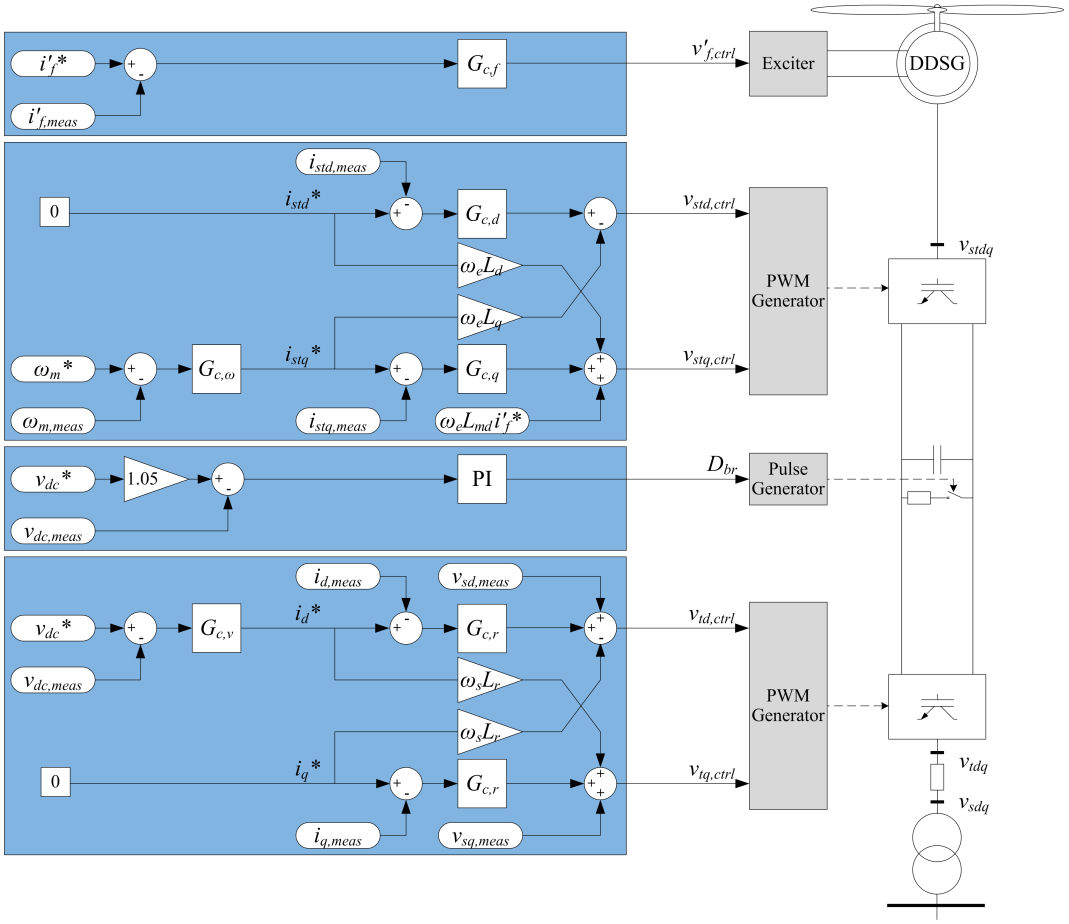

Figure 3.1: WECS control overview.

where S is the apparent converter power, f_{min} is the minimum between the grid and the generator nominal electrical frequency, and ΔV_{DC} is the allowed steady-state peak-to-peak voltage ripple in the DC-link. Typically Δv_{dc} is 2% of v^*_{dc} [11].

3.2 WECS control

In this section, first, we design the back-to-back converter controllers. Then, we systematically calculate their PI parameters using the symmetrical optimum method. An overview of the controller is shown on Fig.3.1. Sign conventions are shown on Fig.3.2.

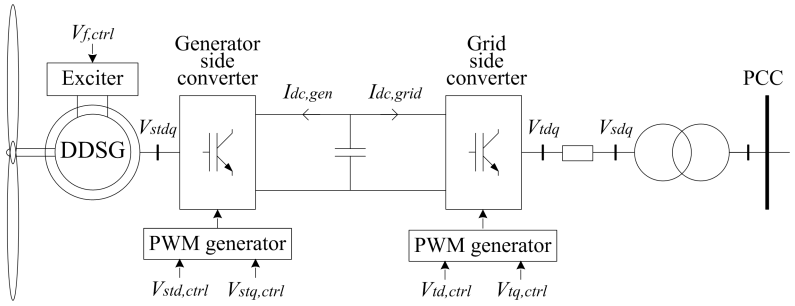

Figure 3.2: Overview of the WECS model.

3.2.1 VSC and exciter equations

From a control point of view, the VSCs and the exciter systems are taken into account by means of a first order transfer function $G_d(s)$ [16; 17],

$$G_d(s) = \frac{v_{out}}{v_{ctrl}} = \frac{1}{1 + T_a s} \tag{3.4}$$

where v_{ctrl} is the input control voltage, and v_{out} is the output voltage. T_a is the time delay due to the computation and generation time. To simplify, we take $T_a = 1/f_{PWM}$ for both systems.

3.2.2 Grid-side equations

In terms of instantaneous variables, with positive currents going from the converter to the grid, the grid-side circuit equations are,

$$\mathbf{v}_{tabc} - \mathbf{v}_{sabc} = \mathbf{R}_r \ \mathbf{i}_{abc} + \frac{d\boldsymbol{\lambda}_{abc}}{dt} \tag{3.5}$$

$$\boldsymbol{\lambda}_{abc} = \mathbf{L}_r \ \mathbf{i}_{abc} \tag{3.6}$$

where $\mathbf{R}_r$ and $\mathbf{L}_r$ are the line reactor resistance and inductance diagonal matrices. Triphasic variables can be transformed from the stationary circuit to a

synchronous-rotating dq reference frame by using the qdo-transformation [66],

$$\mathbf{f}_{qdo} = [K(\theta_s)]\,\mathbf{f}_{abc} \tag{3.7}$$

$$[K(\theta)] = \frac{2}{3}\begin{bmatrix} cos\theta & cos(\theta - \frac{2\pi}{3}) & cos(\theta + \frac{2\pi}{3}) \\ sin\theta & sin(\theta - \frac{2\pi}{3}) & sin(\theta + \frac{2\pi}{3}) \\ \frac{1}{2} & \frac{1}{2} & \frac{1}{2} \end{bmatrix} \tag{3.8}$$

where θ_s is the synchronous angular position of the dq reference frame. By applying this transformation on Eqs.3.5 and 3.6, the grid-side circuit equations in the dq reference frame are,

$$\mathbf{v}_{tqdo} - \mathbf{v}_{sqdo} = \mathbf{R}_r\ \mathbf{i}_{qdo} + \omega_s \boldsymbol{\lambda}_{dq} \frac{d\boldsymbol{\lambda}_{qdo}}{dt} \tag{3.9}$$

$$\boldsymbol{\lambda}_{qdo} = \mathbf{L}_r\ \mathbf{i}_{qdo} \tag{3.10}$$

where ω_s is the synchronous angular speed of the dq reference frame and,

$$\boldsymbol{\lambda}_{dq}^T = [\lambda_d\ \ -\lambda_q\ 0] \tag{3.11}$$

Under the assumption that the system has no zero sequence component, in the dq reference frame, the grid-side circuit equations become [14],

$$\frac{d}{dt}\begin{bmatrix} i_q \\ i_d \end{bmatrix} = \begin{bmatrix} -\frac{R_r}{L_r} & -\omega_s \\ \omega_s & -\frac{R_r}{L_r} \end{bmatrix}\begin{bmatrix} i_q \\ i_d \end{bmatrix} + \frac{1}{L_r}\begin{bmatrix} v_{tq} - v_{sq} \\ v_{td} - v_{sd} \end{bmatrix} \tag{3.12}$$

Note the cross-coupling terms $-\omega_s i_d$ and $\omega_s i_q$ between the two axis. A decoupling can be obtained by defining Δv_q and Δv_d as [13],

$$\Delta v_q = v_{tq} - v_{sq} - \omega_s L_r i_d \tag{3.13}$$

$$\Delta v_d = v_{td} - v_{sd} + \omega_s L_r i_q \tag{3.14}$$

Then i_q and i_d respond to Δv_q and Δv_d respectively, through a simple first-order

transfer function $F_r(s)$,

$$F_r(s) = \frac{i_q}{\Delta v_q} = \frac{i_d}{\Delta v_d} = \frac{1}{R_r}\frac{1}{1+\tau_r s} \tag{3.15}$$

where $\tau_r = L_r/R_r$.

3.2.3 Grid power equations

The AC active and reactive powers expressed in the grid voltage-oriented dq reference frame are,

$$P_{ac} = \frac{3}{2}\, v_{sd} i_d \tag{3.16}$$

$$Q_{ac} = -\frac{3}{2}\, v_{sd} i_q \tag{3.17}$$

3.2.4 DC-link equations

The AC and DC sides of the grid-side VSC are related through the power balance on an instantaneous basis. With the convention shown in Fig.3.2, from Eq.(3.16),

$$v_{dc} i_{dc,grid} = \frac{3}{2} v_{sd} i_d \tag{3.18}$$

And the DC-link voltage equation is,

$$C\frac{dv_{dc}}{dt} = -i_{dc,grid} - i_{dc,gen} \tag{3.19}$$

To design the DC-link voltage controller, we insert (3.18) into the right side of (3.19), we consider $i_{dc,gen}$ as a disturbance and we approximate $v_{sd} \approx v_{dc}/2$ [16; 18; 21]. Then v_{dc} responds to i_d through a simple first-order transfer function $G_v(s)$,

$$G_v(s) = \frac{v_{dc}}{i_d} = -\frac{3}{4C}\frac{1}{s} \tag{3.20}$$

Note that, when considering 3-level NPC converter (see section 2.3.1.4), the DC-link voltage controller should be able to equalize the voltages of the two DC-link capacitors. To this end, a modified form of Eq.3.20 has been introduced by

Yazdani *et al.* [14].

3.2.5 Generator-side equations

From a control point of view, the generator linear dq-model is considered. In the rotor position-oriented dq reference frame, in motor convention, the dynamic model of the machine is [66, p. 201,Eqs.(5.5-8)-(5.5-21)],

$$L_q \frac{di_{stq}}{dt} = -R_s i_{stq} - \omega_e L_d i_{std} - \omega_e L_{md} i'_f + v_{stq} \tag{3.21}$$

$$L_d \frac{di_{std}}{dt} = -R_s i_{std} + \omega_e L_q i_{stq} - L_{md} \frac{di'_f}{dt} + v_{std} \tag{3.22}$$

$$L_f \frac{di'_f}{dt} = -R'_f i'_f - L_{md} \frac{di_{std}}{dt} + v'_f \tag{3.23}$$

where ω_e is the angular electrical speed of the rotor, $L_d = L_{ls} + L_{md}$, $L_q = L_{ls} + L_{mq}$, and $L_f = L'_{lf} + L_{md}$. Note that rotor quantities are referred to the stator-side. If the closed loop system is stable and if the field current is kept constant, $\frac{di_{std}}{dt}$ and $\frac{di'_f}{dt}$ become zero after transients. Eqs.(3.21), (3.22) and (3.23) can then be approximated and rewritten as,

$$\frac{d}{dt}\begin{bmatrix} i_{stq} \\ i_{std} \end{bmatrix} = \begin{bmatrix} -\frac{R_s}{L_q} & -\frac{\omega_e L_d}{L_q} \\ \frac{\omega_e L_q}{L_d} & -\frac{R_s}{L_d} \end{bmatrix} \begin{bmatrix} i_{stq} \\ i_{std} \end{bmatrix} + \begin{bmatrix} \frac{v_{stq}}{L_q} - \frac{\omega_e L_{md} i'_f}{L_q} \\ \frac{v_{std}}{L_d} \end{bmatrix} \tag{3.24}$$

$$L_f \frac{di'_f}{dt} = -R'_f i'_f + v'_f \tag{3.25}$$

Note the cross-coupling terms $-\frac{\omega_e L_d}{L_q}$ and $\frac{\omega_e L_q}{L_d}$ between the two axis. A decoupling can be obtained by defining Δv_{stq} and Δv_{std} as [14],

$$\Delta v_{stq} = v_{stq} - \omega_e L_d i_{std} - \omega_e L_{md} i'_f \tag{3.26}$$

$$\Delta v_{std} = v_{std} + \omega_e L_q i_{stq} \tag{3.27}$$

Then i_{stq} and i_{std} respond to Δv_{stq} and Δv_{std} respectively, through simple first-

order transfer functions $F_q(s)$ and $F_d(s)$,

$$F_{stq}(s) = \frac{i_{stq}}{\Delta v_{stq}} = \frac{1}{R_s}\frac{1}{1+\tau_q s} \tag{3.28}$$

$$F_{std}(s) = \frac{i_{std}}{\Delta v_{std}} = \frac{1}{R_s}\frac{1}{1+\tau_d s} \tag{3.29}$$

where $\tau_q = L_q/R_s$ and $\tau_d = L_d/R_s$. Eq.(3.25) shows that i'_f responds to v'_f through a simple first-order transfer function $F_f(s)$,

$$F_f(s) = \frac{i'_f}{v'_f} = \frac{1}{R'_f}\frac{1}{1+\tau_f s} \tag{3.30}$$

where $\tau_f = L_f/R'_f$.

3.2.6 Generator mechanical equations

The machine speed is related to the resulting torque, in motor convention, by the mechanical equation,

$$J\frac{dw_m}{dt} = T_m + T_e + T_{damp} \quad [N.m] \tag{3.31}$$

where J is the moment of inertia, w_m is the machine mechanical speed, T_m is the externally applied mechanical torque, T_e is the electromagnetic torque developped by the machine, and T_{damp} is the damping torque. A positive resulting torque $dT = T_m + T_e + T_{damp}$ acts to turn the rotor in the direction of increasing θ. T_e is positive when the machine is motoring and negative when the machine is generating. T_m is negative when the machine is motoring and positive when the machine is generating.

The machine electromagnetic torque expressed in the rotor position-oriented dq reference frame, in motor convention, is [66, p. 206 Eq.(5.6-2)],

$$T_e = \frac{3}{2}P\left[L_{md}i'_f i_{stq} + (L_{md} - L_{mq})i_{std}i_{stq}\right] \quad [N.m] \tag{3.32}$$

where P is the number of pole pairs. If i_{std} is regulated to zero and if the field

current is kept constant to $i_f'^*$, T_e is a linear function of i_{stq}.

To design the speed controller, we neglect the damping torque and we consider the mechanical torque as a disturbance. As a result, the machine mechanical speed responds to the q-axis current through a simple first-order transfer function $G_w(s)$,

$$G_w(s) = \frac{w_m}{i_{stq}} = \frac{3PL_{md}i_f'^*}{2J}\frac{1}{s} \tag{3.33}$$

3.2.7 Grid-side converter control strategy

First, in order to guarantee that all the active power coming from the generator-side converter is instantaneously transfered to the grid, the DC-link voltage must be kept constant. Secondly, in order to be able to support actively the grid, the converter should be able to regulate the reactive power fed to the grid. Taking this into account, the objectives of the grid-side converter controls are:

1. DC-link voltage control (Active power control)

2. Reactive power control

A vector-control approach done in the grid voltage-oriented dq reference frame is adopted. Following Eqs.(3.16) and (3.17), the d-axis current contributes to the instantaneous active power and the q-axis current to the instantaneous reactive power. The controller has a cascaded structure. A fast inner current loop controls the converter d- and q-axis currents. An outer slower loop controls the DC-link voltage to its reference value by the d-axis current, and the reactive power by the q-axis current.

3.2.8 Grid-side converter control design

A decoupled control is obtained by defining the feedback loops and controller $G_{c,r}(s)$ as,

$$v_{tq,ctrl} = G_{c,r}(s)(i_q^* - i_{q,meas}) + \omega_s L_r i_d^* + v_{sq,meas} \tag{3.34}$$

$$v_{td,ctrl} = G_{c,r}(s)(i_d^* - i_{d,meas}) - \omega_s L_r i_q^* + v_{sd,meas} \tag{3.35}$$

The grid-side inner open loop transfer function is,

$$H_{OL,r}(s) = G_d(s)F_r(s) = \frac{\frac{1}{R_r}}{(1+T_a s)(1+\tau_r s)} \tag{3.36}$$

For the design of the outer controller, the grid-side inner closed loop transfer function is approximated by a first order transfer function [22],

$$\begin{cases} H_{eq,r}(s) = \frac{iq}{iq^*} = \frac{id}{id^*} = \frac{1}{1+T_{eq,r}s} \\ T_{eq,r} = t_{s,10}/2.3 \end{cases} \tag{3.37}$$

where $t_{s,10}$ is the 10% settling time of the grid-side inner closed loop transfer function. The control is obtained by defining the feedback loops and controller $G_{c,v}(s)$ as,

$$i_d^* = G_{c,v}(s)(v_{dc}^* - v_{dc,meas}) \tag{3.38}$$

The grid-side d-axis outer open loop transfer function is,

$$H_{OL,r}(s) = G_v(s)H_{eq,r}(s) = \frac{-\frac{3}{4C}}{(1+T_{eq,r}s)\,s} \tag{3.39}$$

3.2.9 Generator-side converter control strategy

First, in order to maximize the power extracted, the generator speed must be regulated to its optimal value (MPPT). Secondly, as shown in section 3.2.5, in order to control the generator speed, i_{std} must be regulated to zero. Taking this into account, the objectives of the generator-side current controls are:

1. MPPT
2. d-axis current control

A vector-control approach done in the rotor position-oriented dq reference frame is adopted. The controller has a cascaded structure. A fast inner current loop controls the converter current in d- and q-axis currents. An outer slower loop controls the machine torque to its optimal reference value by the q-axis current, while the d-axis current is kept to zero.

3.2.10 Generator-side converter control design

Following a procedure similar to section 3.2.8, a decoupled control is obtained by defining the feedback loops and controllers $G_{c,q}(s)$ and $G_{c,d}(s)$ as,

$$v_{stq,ctrl} = G_{c,q}(s)(i^*_{stq} - i_{stq,meas}) + \omega_e L_d i^*_{std} + \omega_e L_{md} i'^*_f \tag{3.40}$$

$$v_{std,ctrl} = G_{c,d}(s)(i^*_{std} - i_{std,meas}) - \omega_e L_q i^*_{stq} \tag{3.41}$$

The generator-side inner open loop transfer functions are,

$$H_{OL,q}(s) = G_d(s)F_{stq}(s) = \frac{\frac{1}{R_s}}{(1 + T_a s)\,(1 + \tau_q s)} \tag{3.42}$$

$$H_{OL,d}(s) = G_d(s)F_{std}(s) = \frac{\frac{1}{R_s}}{(1 + T_a s)\,(1 + \tau_d s)} \tag{3.43}$$

The field current control is obtained by defining the feedback loop and controller $G_{c,f}(s)$ as follow,

$$v'_{f,ctrl} = G_{c,f}(s)(i'^*_f - i'_{f,meas}) \tag{3.44}$$

The field open loop transfer function is,

$$H_{OL,f}(s) = G_d(s)F_f(s) = \frac{\frac{1}{R'_f}}{(1 + T_a s)\,(1 + \tau_f s)} \tag{3.45}$$

Following a procedure similar to section 3.2.8, the control is obtained by defining the feedback loop and controller $G_{c,w}(s)$ as,

$$i^*_{stq} = G_{c,w}(s)(w^*_m - w_{m,meas}) \tag{3.46}$$

The generator-side q-axis outer open loop transfer function is,

$$H_{OL,w} = G_w(s)H_{eq,q}(s) = \frac{\frac{3PL_{md}i'^*_f}{2J}}{(1 + T_{eq,q}s)\,s} \tag{3.47}$$

3.2.11 Symmetrical optimum method

Consider an open loop transfer function of the form,

$$H_{OL}(s) = \frac{K}{(1 + T_\alpha s)\, s} \tag{3.48}$$

The controller tuning can be done using the symmetrical optimum method. The method has the advantage of maximizing the phase margin and therefore the system can withstand more delay. Besides it has good disturbance rejection compared to modulus optimum method and it is possible to specify the open loop crossover frequency [22; 23]. The parameters of the PI controller,

$$G_c(s) = K_p \frac{1 + T_i s}{T_i s} \tag{3.49}$$

can be found with [23],

$$\{a, T_i, K_p\} = \left\{ \frac{1}{\omega_c T_\alpha}, a^2 T_\alpha, \frac{1}{a T_\alpha K} \right\} \tag{3.50}$$

where ω_c is the open loop crossover frequency, and a is a design parameter in the range $\{2, 4\}$. An higher value of a leads to better damping but slower response.

Consider an open loop transfer function of the form,

$$H_{OL}(s) = \frac{K}{(1 + T_\alpha s)\,(1 + T_\beta s)} \tag{3.51}$$

with $T_\beta >> T_\alpha$. The controller tuning can be done using the symmetrical optimum method around crossover frequency by approximating $\frac{1}{1+T_\beta s} \approx \frac{1}{T_\beta s}$ [22].

3.2.12 Controllers tuning

As the inner and outer open loop transfer functions of the system are all of the form of Eqs.(3.48) or (3.51), all the controllers can be tuned using the symmetrical optimum method. The tuning goals are:

(i) inner loop/field closed loop bandwidth one order of magnitude smaller than the switching frequency of the converter/PWM to avoid noise.

Table 3.1: Controller tuning

	ω_c (rad.s^{-1})	a –	K_p (si)	T_i (s)
$G_{c,r}$	$\frac{2\pi f_{PWM}}{20}$	$\frac{1}{\omega_c T_a}$	$\frac{\tau_r R_r}{aT_a}$	$a^2 T_a$
$G_{c,v}$	–	3	$-\frac{4C}{3}\frac{1}{aT_{eq,r}}$	$a^2 T_{eq,r}$
$G_{c,d}$	$\frac{2\pi f_{PWM}}{20}$	$\frac{1}{\omega_c T_a}$	$\frac{\tau_d R_s}{aT_a}$	$a^2 T_a$
$G_{c,q}$	–	4	$\frac{\tau_q R_s}{aT_a}$	$a^2 T_a$
$G_{c,f}$	$\frac{2\pi f_{field}}{20}$	$\frac{1}{\omega_c T_a}$	$\frac{\tau_f R_f}{aT_a}$	$a^2 T_a$
$G_{c,w}$	–	4	$\frac{2J}{3PL_{md}i_f^*}\frac{1}{aT_{eq,q}}$	$a^2 T_{eq,q}$

(ii) the generator-side d-axis and field current loops are designed to be fast in comparison to the generator-side q-axis loop to guaranty that T_e is a linear function of i_{stq} in Eq.(3.32).

(iii) slow outer loops in comparison to the inner loops.

(iv) the generator-side outer loop is designed to limit the mechanical stress on the machine.

To achieve (i), we use Eq.(3.50) to calculate the minimal value of a that meets the bandwidth requirement for the grid-side inner loops, the generator-side d-axis inner loop, and the field loop. To achieve (ii), we set $a = 4$ for the generator-side q-axis inner loop to obtain the slowest response. To achieve (iii) for the grid-side converter, we set $a = 3$ for the outer loop as a compromise between performance and overshoot. To achieve (iii) and (iv) for the generator-side converter, we set $a = 4$ for the outer loop to obtain the slowest response. Analytical formulas for the systematic tuning of the PI controllers are summarized in Table 3.1.

3.2.13 Discussion

We would like to emphasize the main advantages of our WECS controller tuning method.

User-centered: The aim of this work is not to give an optimal design for the system, but to provide a step-by-step method that can be used to build a working model that can be used as a reference model for future studies.

Systematical: The systematic determination of controller parameters enable to avoid the time-consuming trial-and-error approach.

Tolerance: By using the symmetrical optimum method to tune the converter PI controllers, we ensure good delay tolerance and good disturbance rejection.

Delay: The controller design takes into consideration the time delay due to the computation time and the generation time.

Inner loop bandwidth: The adopted method ensures that the inner loops closed loop bandwidth are one order of magnitude smaller than the switching frequency of the converter to avoid noise.

Outer loop bandwidth: The adopted method ensures that the outer loops are slow in comparison to the inner loops.

The main drawback of our reference WECS model control and design method is that it is assumed that the system state variable are know. Nevertheless, we estimate that sensor effect integration or sensorless control are advanced control techniques that are out of the scope of this thesis.

3.3 Reference WECS model

In this section, we simulate a WECS using a 2 MW conventional generator. First, it allows us to evaluate the performance of the adopted power converter topology, excitation system with their associated control strategies. Secondly, this simulation will be used as a reference WECS model for comparison with WECS using superconducting generator.

3.3.1 Model and sequence

In the reference simulation, the generator is modeled using the dq-model. The averaged full WECS model is used. The grid-side reactive power reference is set to 0 pu. The back-to-back converter parameters are summarized in Table A.1. The generator parameters are summarized in Table B.1. The PI controller parameters are summarized in Table B.2. Note that the tuning goals defined

in section 3.2.12 are respected with the calculated parameters. The simulation sequence is described in details in Appdx A.2: startup from t= 0 s to t= 30 s, sudden wind variations from t= 30 s to t= 50 s, and low-voltage ride-through t= 50 s to t= 60 s.

3.3.2 Simulation results

Simulation results are shown on Figs.3.4 and 3.3. *wind* is the wind speed. P_m is the mechanical power extracted from the wind. P_e and Q_e is the generator active and reactive power (from the machine to the converter). ω_m is the rotor mechanical speed. i_{std} and i_{stq} are the d- and q-axis current of the generator stator. $dT = T_m + T_e$ is the resulting torque on the machine shaft neglecting T_{damp}. i_f is the field current. v_{dc} is the DC-link voltage. P_{chop} is the power dissipated in the breaking resistor used for DC-link protection. P_{grid} and Q_{grid} are the active and reactive power transferred to the grid. i_d and i_q are the d- and q-axis current of the grid. V_{grid} is the grid peak voltage.

3.3.2.1 Startup

At t= 1 s, the grid-side converter is switched on: the DC-link voltage is regulated to its nominal value. At t= 2.1 s, the generator-side converter is switched on: the turbine speed increases, the power capture increases and is transmitted to the grid. In steady-state, the wind speed is at rated output speed, the MPPT controller controls the turbine speed to 1 pu, the generator operates at rated power, the grid-side converter controls the active power injected to the grid to 1 pu by keeping the DC-link voltage to its nominal value, while the reactive power is maintained to 0 pu.

3.3.2.2 Sudden wind variations

At t= 32 s, the wind suddenly drops from 12 m/s to 7 m/s. The power capture is reduced, and the MPPT controller sets the new optimal speed. The DC-link voltage is regulated to its nominal value. Then at t= 40 s, the wind increases from 7 m/s to 12 m/s. The MPPT controller regulates the power transfer to 1 pu. Here again, the system reaches its new equilibrium.

3.3.2.3 Low-voltage ride-through

At t= 50.5 s, the grid voltage drops, the grid-side converter increases its d-axis current in order to be able to go on transferring all the power from the generator. But the rating of the converter limits the converter maximum power transfer. And as the power extracted from the wind P_m cannot be reduced instantaneously because of the slow dynamic of the wind turbine, there is a power imbalance. The excess power from the generator flows into the DC-link capacitor whose voltage increases. When the DC-link voltage rises, the LVRT protection scheme is activated: the excess energy is dissipated in the breaking resistor P_{chop} instead of charging the DC-link capacitor. The DC-link overvoltage is strictly limited. At t= 52 s, the grid voltage returns to 1 pu, the grid-side converter operates in saturation mode till the DC-link capacitor has been regulated to its nominal value. Thus the system can stay online, ride through the dip voltage and operate safely.

3.4 Summary

In this chapter, we have presented a step-by-step method for the design and control of variable speed wind turbine generators using direct-drive electrically excited synchronous machines connected to the grid through a full-scale back-to-back converter. We dimensioned the DC-link voltage and capacitor. We modeled in details the electrical and mechanical parts of the system from a control point of view. We designed a cascaded-loop controller for both generator-side and grid-side converter. We calculated the controller PI parameters in a systematical way by using the symmetrical optimum method.

Finally, we evaluated the performances of a conventional 2 MW wind turbine generator with the designed converter during startup, sudden wind variations and low-voltage ride-through.

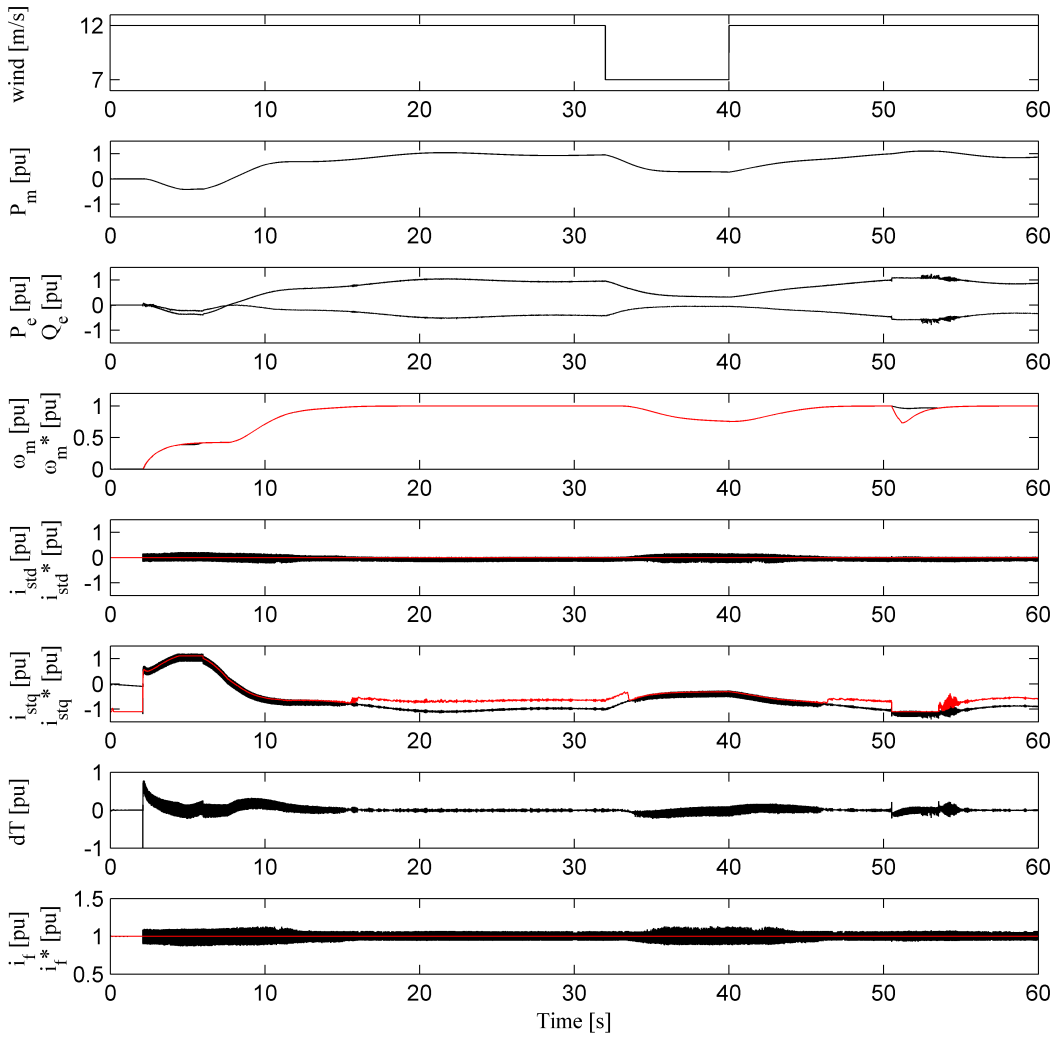

Figure 3.3: Reference 2 MW WECS model - Generator-side converter simulation results.

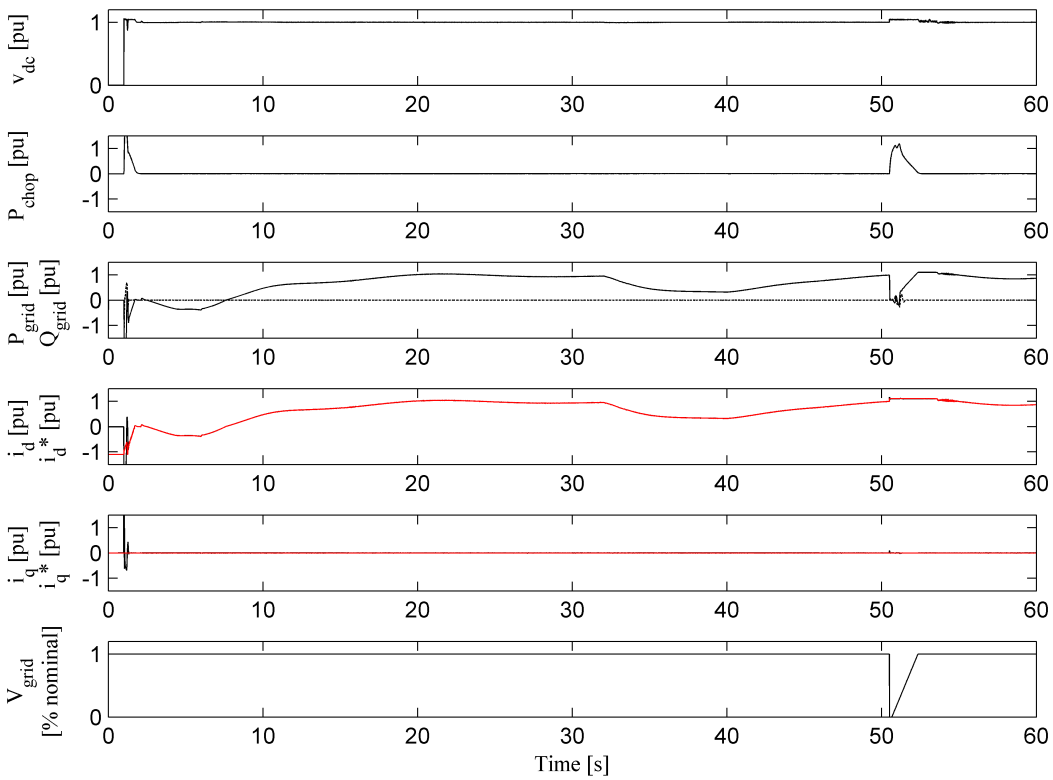

Figure 3.4: Reference 2 MW WECS model - Grid-side converter simulation results.

Chapter 4

Nonlinear coupled FE phase-domain model

Objectives: Report on a novel general and flexible implementation of the phase-domain model using N-dimensional lookup tables.

Motivations: Need for a lumped-parameter machine model that could represent naturally and accurately both space harmonics and (cross-)saturation (see section 1.3.5).

Contributions: Comparison of various implementations of the linear phase-domain model with the dq-model, discussion on the choice of the phase-domain model state variables, study on the implementation of the linear phase-domain model with lookup tables, clarification of the nonlinear model equations, implementation of a general nonlinear phase-domain model using N-dimensional lookup tables, and comparison of the nonlinear phase-domain model with the FE model.

4.1 Phase-domain model

In this section, we introduce the phase-domain model and propose an implementation using lookup tables. Note that this chapter deals with the modeling of superconducting synchronous machines with the understanding that the analysis of almost any kind of rotating machine can be performed similarly [66].

4.1.1 Mathematical model

We use here the motor convention, meaning that positive currents enter the machine terminals (Fig.4.1). Using matrix notation, the phase-domain model is expressed in terms of physical variables as,

$$\mathbf{v} = \mathbf{R}\ \mathbf{i} + \frac{d\boldsymbol{\lambda}}{dt} \tag{4.1}$$

$$\boldsymbol{\lambda} = f(\theta, \mathbf{i}) \tag{4.2}$$

$$J\frac{d^2\theta}{dt^2} = T_m + T_e + T_{damp} \tag{4.3}$$

$$T_e = h(\theta, \mathbf{i}) \tag{4.4}$$

where $\mathbf{v}$, $\mathbf{i}$, and $\boldsymbol{\lambda}$ are the instantaneous voltage, current and flux linkage vectors of the stator and rotor windings, respectively. θ is the rotor mechanical angle. $\mathbf{R}$ is the resistance matrix of the windings. J is the moment of inertia. And T_m, T_e and T_{damp} are the mechanical torque, the electromagnetic torque and the damping torque, respectively. In the general case, the flux linkage and the electromagnetic torque are not explicitly given, as they are nonlinear functions of rotor position and currents.

4.1.2 Integrability

The integrability of such a system cannot be assured *a priori*. It depends on the existence of a bijective relationship between the currents $\mathbf{i}$ and the flux linkages

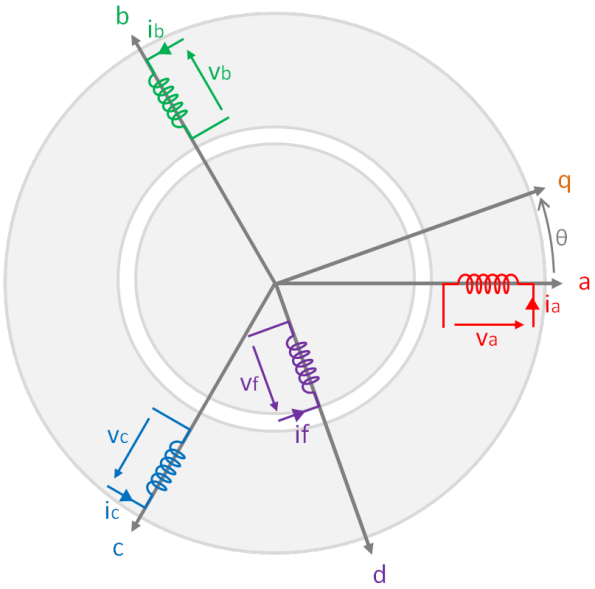

Figure 4.1: Three-phase synchronous machine.

$\boldsymbol{\lambda}$. If this bijection exists, there is a function g such as,

$$\mathbf{i} = g(\theta, \boldsymbol{\lambda}) \tag{4.5}$$

In that case, a change of variable can be done between $\mathbf{i}$ and $\boldsymbol{\lambda}$, and both of them can be used as state variables of the system. In this paper, to guarantee the existence of this bijection, we make the hypothesis that the losses of the coupling field (eddy current, hysteresis, or dielectric losses) are neglectable [66], and that the windings are not closely coupled. Note that these are the only hypothesis needed to derive the general nonlinear phase-domain model.

4.1.3 Lookup Tables

The functions f (or g) and h can be determined by analytical formulas, numerical calculations, or measurements. Both numerical calculations and measurements will result in a discrete data set. An efficient way to deal with this data set without making any further approximation is to use lookup tables (LUTs).A N-dimensional (N-D) lookup table is a structured representation of a discrete

function of N variables. It uses N breakpoint data sets to index a table data set, and relates an input vector to an output value by looking up or interpolating the table data set. Common interpolation methods are linear and cubic-spline. If the table inputs are out of range, the lookup table can extrapolate the output value too. LUTs are particulary adapted to describe complex nonlinear relationships, for to retrieve a value from memory is often faster than to compute a complex function. Nevertheless, there are limitations such as the available amount of memory, and the time necessary to first construct the table.

Note that, if no analytical formula is available, only $f(\theta, \mathbf{i})$ and $h(\theta, \mathbf{i})$ can be obtained directly. Indeed, experimentally, it is only possible to fix the currents for a given rotor position and then to measure the flux linkage [37]. For the same reason, the finite element model and reluctance model permit only the direct determination of f and h. In that case, h can be determined using the Maxwell stress tensor, for example. Therefore, $g(\theta, \boldsymbol{\lambda})$ has to be obtained indirectly from $f(\theta, \mathbf{i})$ (See section 4.3.2.3).

4.2 Linear phase-domain model

In this section, we develop the equations of the linear phase-domain model and discuss its implementation.

4.2.1 Linear equations

In the linear case, a simple expression for Eq.4.2 and Eq.4.4 can be derived by using the concept of inductance and the global virtual work method [66],

$$\boldsymbol{\lambda} = \mathbf{L}(\theta)\ \mathbf{i} \tag{4.6}$$

$$T_e = \frac{1}{2}\mathbf{i}^T \frac{d\mathbf{L}(\theta)}{d\theta}\mathbf{i} \tag{4.7}$$

where $\mathbf{L}(\theta)$ is the stator and rotor windings inductance matrix.

The linear phase-domain model can be implemented by using the current $\mathbf{i}$ as

a state variable (PD-i). In that case, Eqs.4.1 and 4.6 can be written,

$$\frac{d\mathbf{i}}{dt} = \mathbf{L}(\theta)^{-1}\left[\mathbf{v} - \mathbf{R}\ \mathbf{i} - \omega\frac{d\mathbf{L}(\theta)}{d\theta}\mathbf{i}\right] \tag{4.8}$$

where ω is the rotor mechanical speed. Another option is to choose the flux linkage λ as a state variable (PD-λ). In that case, Eqs.4.1 and 4.6 can be written,

$$\frac{d\boldsymbol{\lambda}}{dt} = \mathbf{v} - \mathbf{R}\ \mathbf{L}(\theta)^{-1}\boldsymbol{\lambda} \tag{4.9}$$

4.2.2 Implementation

4.2.2.1 Bloc Implementation

Block implementations of the PD-i and PD-λ models are shown in Fig.4.2(a) and Fig.4.2(b). Note that even if the flux linkage is used as state variable, the current is still available as output. The phase-domain inductance matrix and its derivative with respect to θ are built with the same analytical equations used to derive the SimPowerSystems dq-model (dq-SPS) [66]. Thus, the three models are analytically equivalent. The matrices are built using function blocks and concatenation blocks to take advantage of their symmetry. Finally, both models are embedded in a Simulink SimPowerSystems toolbox block. In the following, the machine is used as a generator. Its input mechanical speed is 1 pu and its load is 1 pu resistive. Simulation parameters are: simulation time 0.1 s in steady-state, relative and absolute error tolerance 10^{-6}, maximum and minimum time step limits 10^{-3} and 10^{-10}, and ode23t variable-step mod. stiff / trapezoidal solver. We use a personal computer (Intel i5, 2.53 GHz) with standard (not compiled, non-real-time) Simulink. We use the Simulink profiler to capture data while each model runs. The execution time does not include the initialization or termination time.

4.2.2.2 State Variable Choice

The choice of the phase-domain state variable has an influence on the computation speed as shown in Table 4.1. Clearly, the PD-λ model is faster than the PD-i model. First, there are fewer steps. Since the maximum rate of change of

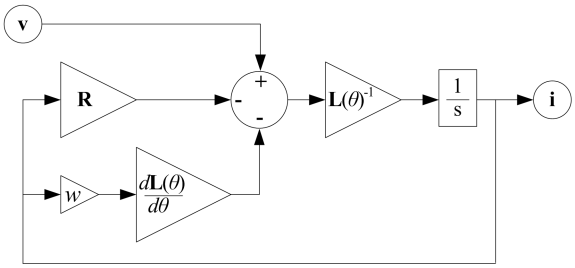

(a) PD-i model

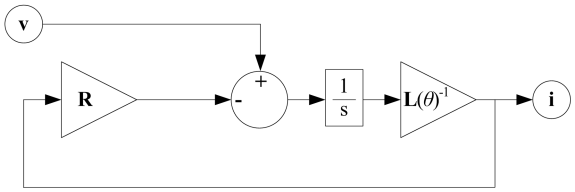

(b) PD-λ model

Figure 4.2: Block implementation of the linear phase-domain model.

Table 4.1: Model efficiency comparison

Model	dq-SPS	PD-λ	PD-i
Execution time (s)	0.51	7.57	83.66
No. of steps	100	2641	11877
Time per step (ms)	5.1	2.9	7.0

the flux linkage is lower than that of the current, the integration step can be longer. Secondly, it takes less time per step. This is because there is no need to calculate the derivative of the inductance matrix as a function of the rotor angle as in Eq.4.8. Note that in our implementation, as opposed to dq-SPS, the stator neutral point is not necessarily grounded. Making such approximation could further decrease the phase-domain computation time [33]. Nevertheless, the execution time per step of the PD-λ model is lower than the dq-SPS model, which could reduce the total computation time for fixed step or multi-machine simulations. Finally, we underline that although the implementation is different, our results are consistent with those reported by Wang *et al.* [29].

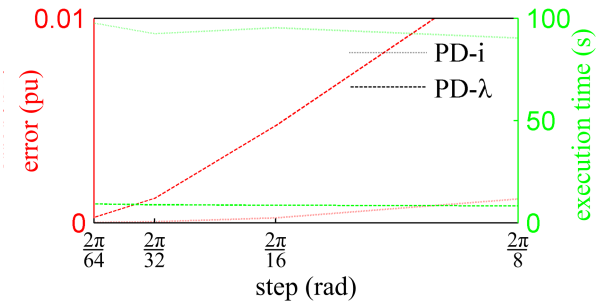

Figure 4.3: Implementation of the PD current equations with LUTs. Step is in electrical radians.

4.2.2.3 Electric Equations with LUTs

When the space harmonics content is high, the inductance matrix in Eqs.4.8 and 4.9 is a complex function of θ. This matrix can then simply be implemented by using 1-D lookup tables retrieved in terms of rotor angle. To determine the error introduced by LUTs, we calculate the coefficients of $\mathbf{L}(\theta)$ and $\frac{d\mathbf{L}(\theta)}{d\theta}$, with the same analytical formulas used to derive the dq-SPS model. We calculate coefficients for θ from 0 to 2π eletrical radian and store them in fifteen 1-D lookup tables. The inductance matrix is then built by using 1-D lookup table blocks and concatenation blocks. Fig.4.3 shows the absolute error and the execution time of each model as a function of the discretization step using cubic-spline interpolation. Even if the PD-λ model is more efficient, the error introduced by the lookup table can be significant for large discretization steps. Although not reported here due to space limitation, LUTs with linear interpolation lead to significant errors. Moreover, the execution time does not necessarily decrease; for in order to achieve a given accuracy, linear interpolation might require more steps than its cubic-spline counterpart.

4.2.2.4 Torque Equation with LUTs

Following Eq.4.7, the electromagnetic torque can be obtained by multiplying the derivative of the inductance by the current. There are two possibilities. One is to store in 1-D lookup tables the coefficients of $\frac{d\mathbf{L}(\theta)}{d\theta}$. Then at each time step, the tables are retrieved in terms of rotor angle and the product is performed. The

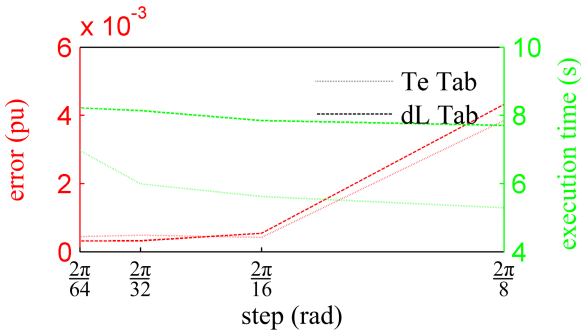

Figure 4.4: Implementation of the PD torque equation with LUTs.
Step is in electrical radians.

other possibility is to store directly in a N-D lookup table the product T_e. In that case, the T_e value is directly retrieved at each time step in terms of rotor angle and currents. To compare both methods, we calculate the coefficients of $\frac{d\mathbf{L}(\theta)}{d\theta}$ and T_e, with the same analytical formulas used to derive the dq-SPS model. On the one hand, we calculate $\frac{d\mathbf{L}(\theta)}{d\theta}$ coefficients for θ from 0 to 2π eletrical radian and store them in fifteen 1-D lookup tables. On the other hand, we calculate T_e for θ from 0 to 2π eletrical radian and for currents from -2 to 2 pu in steps of 4 pu and store the values in one 7-D lookup table. Note that only two values of the current are required in the linear case. Fig.4.4 shows the relative error and the execution time for each method as a function of the discretization step by using cubic-spline interpolation. For both methods, the error introduced by LUTs is negligible. The T_e method is advantageous in computation time, because the 7-D table requires shorter search time compared to searching all fiftheen 1-D lookup tables.

4.3 Nonlinear phase-domain model

In this section, we develop the equations of the nonlinear phase-domain model and discuss its implementation.

4.3.1 Nonlinear equations

In the nonlinear case, the concept of inductance can be misleading because different definitions lead to different results. Therefore, one has to distinguish between the apparent inductance L^a and the differential inductance L^d. References [30] and [31] give a rigorous formulation of L^a and L^d, and summarize calculation methods from finite element analysis by using energy-perturbation or flux linkage. References [36] and [37] report another approach to calculate L^d based on approximation by an analytical function of the d and q-axis flux linkage. From the above references, the flux linkage $\boldsymbol{\lambda}$ is related to the current $\mathbf{i}$ by the apparent inductance matrix $\mathbf{L}^a$ with,

$$\boldsymbol{\lambda} = \mathbf{L}^a(\theta, \mathbf{i})\ \mathbf{i} \tag{4.10}$$

or by the differential inductance matrix $\mathbf{L}^d$ with,

$$\frac{d\boldsymbol{\lambda}}{dt} = \mathbf{L}^d(\theta, \mathbf{i})\ \frac{d\mathbf{i}}{dt} + \frac{\partial \boldsymbol{\lambda}}{\partial \theta}\frac{d\theta}{dt} \tag{4.11}$$

Here again, the current or the flux linkage can be used as state variables. If the current $\mathbf{i}$ is chosen (PD-i), inserting Eqs.4.10 and 4.11 into Eq.4.1 gives,

$$\frac{d\mathbf{i}}{dt} = \mathbf{L}^d(\theta, \mathbf{i})^{-1}\left[\mathbf{v} - \mathbf{R}\ \mathbf{i} - \omega\frac{\partial \mathbf{L}^a(\theta, \mathbf{i})}{\partial \theta}\mathbf{i}\right] \tag{4.12}$$

When choosing the flux linkage $\boldsymbol{\lambda}$ as a state variable (PD-λ), Eqs.4.1 and 4.10 can be written,

$$\frac{d\boldsymbol{\lambda}}{dt} = \mathbf{v} - \mathbf{R}\ \mathbf{L}^a(\theta, \mathbf{i})^{-1}\boldsymbol{\lambda} \tag{4.13}$$

4.3.2 Implementation

4.3.2.1 Block Implementation

Note the similarity between Eq.4.8 and Eq.4.12. The block implementation of nonlinear PD-i model is therefore similar to Fig.4.2(a) by replacing $\mathbf{L}(\theta)$ with $\mathbf{L}^d(\theta, \mathbf{i})$, and $\frac{d\mathbf{L}(\theta)}{d\theta}$ with $\frac{\partial \mathbf{L}^a(\theta, \mathbf{i})}{\partial \theta}$. In the same way, the block implementation of the nonlinear PD-λ model is similar to Fig.4.2(b) by replacing $\mathbf{L}(\theta)$ with $\mathbf{L}^a(\theta, \mathbf{i})$. If

an implementation with LUTs is considered, N-D lookup tables have to be used instead of 1-D ones. As a result, total calculation time increases, but conclusions from section 4.2 are still valid. Implementations of the nonlinear phase-domain model using the inductance concept have been reported by various authors [32; 34; 35]. Therefore, these implementations are not discussed further in this thesis.

4.3.2.2 About Nonlinear Inductances

We would like to point out the main limitations of the inductance concept in the nonlinear case. First, the necessary distinction between apparent inductance and differential inductance is error-prone during both implementation and parameter calculations. Secondly, the differential inductance matrix contains partial derivatives of the flux linkages with respect to the currents. The numerical derivation increases both computation time and numerical errors. Thirdly, as the inductance matrix is symmetric, an n coils system requires the specification of $(n^2 + n)/2$ inductances, each of which is a function of the rotation angle θ and the n currents. Handling such a volume of data further increases the complexity of the model. Therefore, we investigate here the possibility of directly using flux linkage instead of inductance. In that case, an n coils system requires only the specification of n flux linkages, each of which is a function of θ and n currents. The nonlinear PD-λ model can be then derived from Eqs.4.1 and 4.5 as,

$$\frac{d\boldsymbol{\lambda}}{dt} = \mathbf{v} - \mathbf{R}\; g(\theta, \boldsymbol{\lambda}) \tag{4.14}$$

4.3.2.3 Construction of g Lookup Table

The integration of Eq.4.14 is straightforward, as long as the function $g(\theta, \boldsymbol{\lambda})$ has been specified. As $g(\theta, \boldsymbol{\lambda})$ is not directly available, it must be obtained from $f(\theta, \mathbf{i})$. This has been reported by Stephenson *et al.* [39] in the limited case, where each flux linkage depends only on the rotor angle and one current. But to our knowledge, this procedure has not yet been extended to the general case, where the n flux linkages of the n windings depend on the rotor angle and on their n currents.

For the purpose of discussion, we consider a two coils system, where each flux

linkage depends on the rotor angle θ and on the two currents. For a given angle θ_0, $f(\theta, \mathbf{i})$ and $g(\theta, \boldsymbol{\lambda})$ can be seen as two sets of two sufaces,

$$f(\theta_0, \mathbf{i}) = \begin{cases} \lambda_a(\theta_0, i_a, i_b) \\ \lambda_b(\theta_0, i_a, i_b) \end{cases} \tag{4.15}$$

$$g(\theta_0, \boldsymbol{\lambda}) = \begin{cases} i_a(\theta_0, \lambda_a, \lambda_b) \\ i_b(\theta_0, \lambda_a, \lambda_b) \end{cases} \tag{4.16}$$

From the two surfaces corresponding to $f(\theta_0, \mathbf{i})$, one could construct the two surfaces corresponding to $g(\theta_0, \boldsymbol{\lambda})$ by simple inversion. This inversion permits visualizing the surfaces, but it cannot be used to build a lookup table, because for a given input vector (λ_a, λ_b), the output vector (i_a, i_b) is not always defined [40]. This is illustrated in Fig.4.5. The inversion produces two surfaces similar to Figs.4.5(c) and 4.5(d). On these surfaces, the output vector (i_a, i_b) is defined at the grid intersections with points and is undefined at the grid intersections without points. To build a lookup table, we need (i_a, i_b) to be defined at every grid intersection. This can be solved by using 2-D interpolation to approximate (i_a, i_b) at every undefined grid intersection. Using interpolation and extrapolation, we can even define new breakpoint data sets that would be evenly spaced as shown on Figs.4.5(e) and 4.5(f). This procedure, repeated for each rotor angle, permits to obtain the two 3-D lookup tables defining $g(\theta, \boldsymbol{\lambda})$ from the two 3-D lookup tables defining $f(\theta, \mathbf{i})$. Note that $f(\theta, \mathbf{i})$ does not need to have a lookup table structure because the interpolation can be done from a set of scattered points.

The procedure introduced above can be straighforwardly applied to an n coils system, where each flux linkage depends on the rotor angle θ and on the n currents. In that case, an n-D interpolation must be used for each angle to obtain the n $(n+1)$-D lookup tables defining $g(\theta, \boldsymbol{\lambda})$ from the n $(n+1)$-D lookup tables defining $f(\theta, \mathbf{i})$.

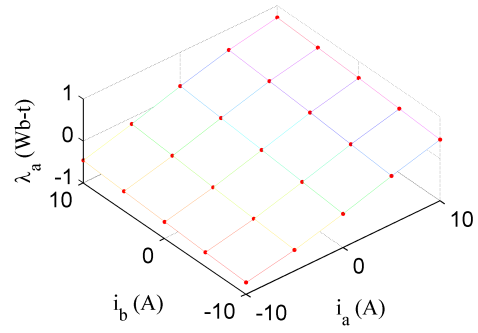

(a) $\lambda_a(\theta_0, i_a, i_b)$ before inversion

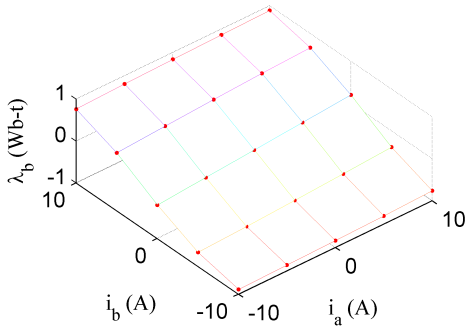

(b) $\lambda_b(\theta_0, i_a, i_b)$ before inversion

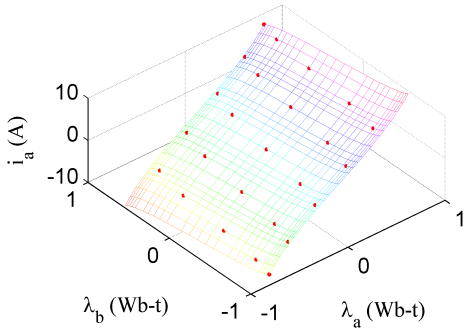

(c) $i_a(\theta_0, \lambda_a, \lambda_b)$ after inversion

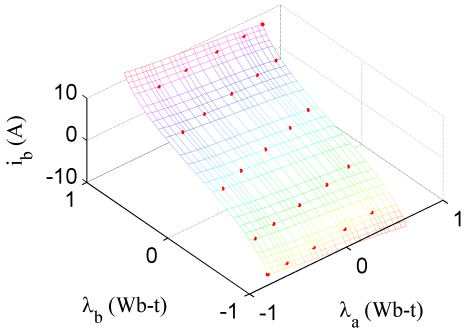

(d) $i_b(\theta_0, \lambda_a, \lambda_b)$ after inversion

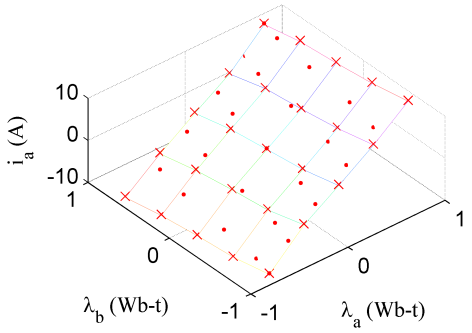

(e) $i_a(\theta_0, \lambda_a, \lambda_b)$ after interpolation

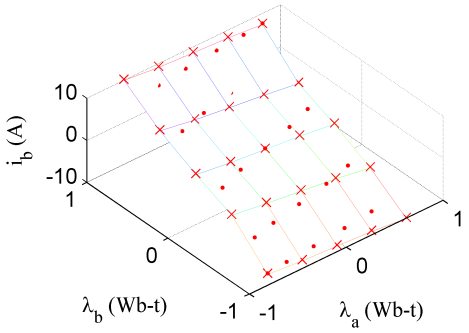

(f) $i_b(\theta_0, \lambda_a, \lambda_b)$ after interpolation

Figure 4.5: Construction of $g(\theta_0, \boldsymbol{\lambda})$ from $f(\theta_0, \mathbf{i})$, case n=2.

4.4 Finite element calculation of phase-domain parameters

In this section, we summarize the formulas used to calculate the parameters of the phase-domain model by 2D finite element analysis.

4.4.1 Flux linkage

Following Eq.(4.2), the flux linkage $\boldsymbol{\lambda}$ can generally be described using n nonlinear functions, each of which is a function of θ and n currents.

In this work, we use the vector potential to calculate the flux linkage. This method is a variant of the method presented in [31; 88; 89]. The magnetic flux linkage of a winding for a given rotor angle and a given set of currents is given by,

$$\lambda = L_{eff} N \sum_{k=1}^{2} \beta_k A_{z,k}^{ave} \tag{4.17}$$

where L_{eff} is the machine effective length, N is the winding number of turns, $\beta_k = \pm 1$ according to the orientation of the winding side k, and $A_{z,k}^{ave}$ is the average vector potential on the winding side k.

The advantage of this method is that the expression of the flux linkage is obtained as a surface integral of the vector potential over the winding cross section. It allows for simple and quick calculation from the linear or nonlinear magnetostatic field solution.

Note that self and mutual inductances in Eq.4.6 can be calculated using the above expression. The self inductance L_{11} of a winding is obtained by exciting a current I_1 through it and by measuring the flux linkage λ_1 of this winding. The self inductance for a given rotor angle is then given by,

$$L_{11} = \frac{\lambda_1}{I_1} \tag{4.18}$$

where I is the current in the winding. The mutual inductance L_{12} between two windings is obtained by exciting a current I_2 through one winding and by measuring the flux linkage λ_1 of the other winding. The mutual inductance for a

given rotor angle is then given by,

$$L_{12} = \frac{\lambda_1}{I_2} \tag{4.19}$$

4.4.2 Electromagnetic torque

Following Eq.(4.4), the electromagnetic torque T_e can generally be described using a nonlinear function, which is a function of θ and n currents.

There are several methods to calculate it using the finite element method. A review and comparison of them can be found in [86]. In this work, we use the magnetostatic Maxwell stress tensor method for electrical rotating machine. A complete development can be found in [87]. The electromagnetic torque for a given rotor angle and a given set of currents is given by,

$$T_e = \frac{L_{eff}\ r_{Te}^2}{\mu_0} \int_0^{2\pi} B_r B_\theta\ d\theta \tag{4.20}$$

where L_{eff} is the machine effective length, μ_0 is the magnetic permeability of the vacuum, r_{Te} is the radius of the circle taken as the integration path, and B_r and B_θ are the radial and tangential components of the magnetic flux density $\mathbf{B}$. Note that the integration path should be defined inside the airgap.

The advantage of this method is that the expression of the torque is obtained as a line integral of the magnetic flux density along the airgap. It allows for simple and quick calculation from the linear or nonlinear magnetostatic field solution. Theoretically, if the field solution is exact, the torque value computed with the above expression is independant of the radius r_{Te}. In practice, with typical FE solutions, the variation of the torque as a function of r_{Te} may be important. Improved methods have been introduced by various authors [85; 86].

4.5 Coupled finite element phase-domain model

The phase-domain electric equation (Eq.4.1) and mechanical equation (Eq.4.3) of a three-phase electrically-excited synchronous machine have been implemented using Matlab/Simulink blocs and the SimPowerSystem toolbox. The general

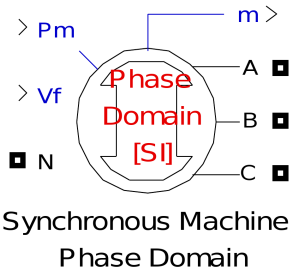

Figure 4.6: Coupled FE phase-domain Matlab/Simulink SimPowerSystem toolbox bloc.

nonlinear flux linkage (Eq.4.2) is calculated using Eq.4.17 and stored in four 5-D lookup tables. The general nonlinear electromagnetic torque (Eq.4.4) is calculated using Eq.4.20 and stored in one 5-D lookup tables. The N-D lookup tables are retrieved in terms of rotor angle and windings currents. The resulting bloc is shown on Fig.4.6.

4.6 Comparison with finite element model

In this section, we compare our implementation of the general nonlinear coupled finite element phase-domain model with the finite element model.

4.6.1 Finite element model

To show the effectiveness of the proposed coupled FE phase-domain model using N-D lookup table, we consider the machine shown in Fig.4.6.4. The machine has one field coil and three armature windings, and therefore a 5-D table is used for the phase-domain model. The armature windings are connected to a three phase resistive load. We do not use inductive load to ensure that the current/voltage waveforms harmonics are due only to space harmonics and saturation. For simplicity, we use the full 2D FE model for both the FE transient analysis and the calculation of the phase-domain model parameters.

4.6.2 Without magnetic material

First, we consider a machine without magnetic material. Therefore, the machine is in linear operation. The field current is set to 1064 A, the resisitive load is 2.4 Ω. Fig.4.7(a) shows the magnetic flux density distribution. Fig.4.7(b) compares the armature voltage obtained by transient finite element method with the proposed phase-domain model. The lookup table is built by varying the rotor angle from 0 to 180 deg in steps of 3.75 deg, the field current from 1010.8 to 1117.2 A in steps of 106.4 A, and the phase currents from -4 to 4 A in steps of 8 A. Note that, in this case, the current/voltage harmonics are the consequence of the space harmonics linked to the discrete nature of the windings (and their respective position).

4.6.3 With non-saturated magnetic material

Secondly, we consider a machine with magnetic iron. The machine is in linear operation: the field current is set to 1064 A, the resisitive load is 2.4 Ω, the maximal flux density is under 1 T. Fig.4.8(a) shows the magnetic flux density distribution. Fig.4.8(b) compares the armature voltage obtained by transient finite element method with the proposed phase-domain model. The lookup table is built by varying the rotor angle from 0 to 180 deg in steps of 3.75 deg, the field current from 1010.8 to 1117.2 A in steps of 106.4 A, and the phase currents from -100 to 100 A in steps of 200 A. Note that, in this case, the current/voltage harmonics are the consequence of the space harmonics linked to the discrete nature of the windings, the slotting, and the saliency.

4.6.4 With saturated magnetic material

Thirdly, we consider the nonlinear operation: the field current is set to 2128 A, the resisitive load is 24 Ω, the maximal flux density is over 1 T. Fig.4.9(a) shows the magnetic flux density distribution. Fig.4.9(b) compares the armature voltage obtained by transient finite element method with the proposed phase-domain model. The lookup table is built by varying the rotor angle from 0 to 180 deg in steps of 3.75 deg, the field current from 2021.6 to 2234.4 A in steps of 212.8 A, and the phase currents from -30 to 30 A in steps of 60 A. Note the saturation of

the stator teeths. In this case, the current/voltage harmonics are the consequence of the space harmonics linked to the discrete nature of the windings, the slotting, the saliency and the saturation.

4.7 Discussion

We would like to emphasize the main advantages of our implementation of the phase-domain model.

Implementation: The implementation with LUTs is straightforward in comparison to the implementation of the classical dq-model.

Nonlinearities: Space harmonics and saturation are naturally and easily included in the model by using lookup tables.

Flexibiliy: By embedding the coupled FE phase-domain into Matlab/Simulink SimPowerSystem bloc, we can perform with great flexibility simulations of the machines connected to external mechanical and electrical systems with associated control strategies.

General: The modeling method proposed here is totally independant of the machine geometry and materials.

The main drawback of the approach using N-D lookup tables is the time necessary to first fill up the table. Finally, we underline that the calculation of the machine N-D lookup tables is performed only once for a given machine design. Afterwards, for any operating conditions, the machine steady-state and transient characteristics can be determined. Thus in comparison with a full finite element model, it is particularly efficient and adapted for the integrated design of electrical machines. Moreover some considerations can help to decrease the number of computations.

Symmetries: For n-phase machines, each armature phase winding is generally identical and offset by $2\pi/n$ electrical degree. As a consequence, assuming core anisotropy, the lookup table can be entirely filled up by calculating only the flux linkages for a rotor angle from 0 to $2\pi/n$ electrical degree.

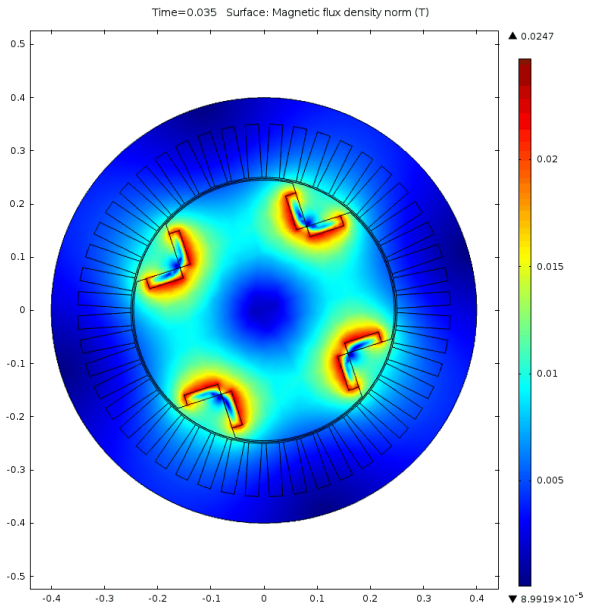

(a) Magnetic flux density distribution

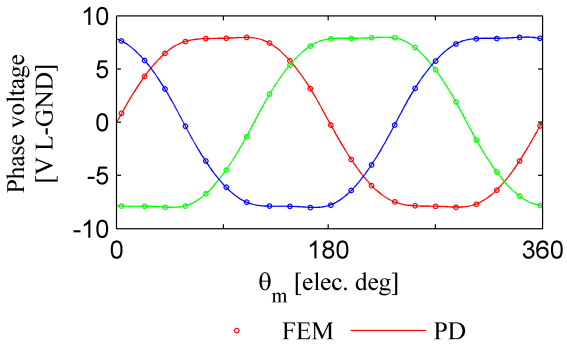

(b) Stator voltage

Figure 4.7: Comparison of the FEM and PD model - Linear case 1.

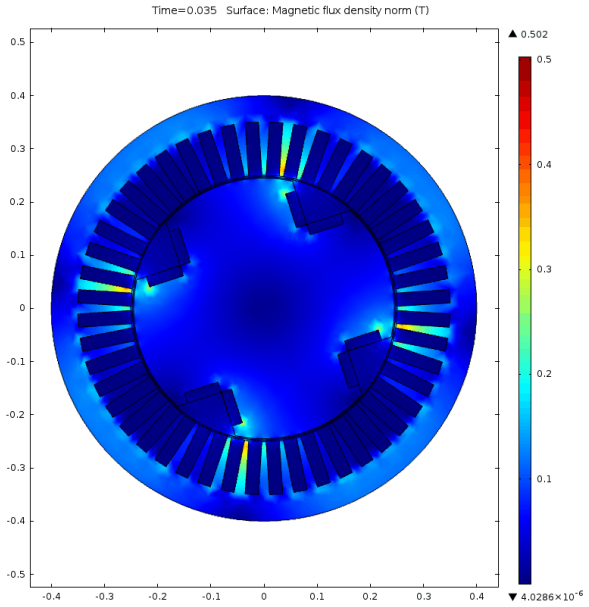

(a) Magnetic flux density distribution

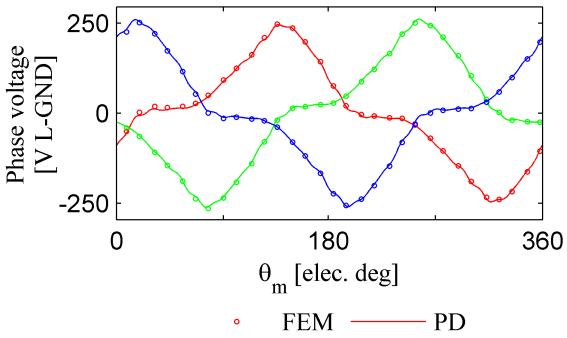

(b) Stator voltage

Figure 4.8: Comparison of the FEM and PD model - Linear case 2.

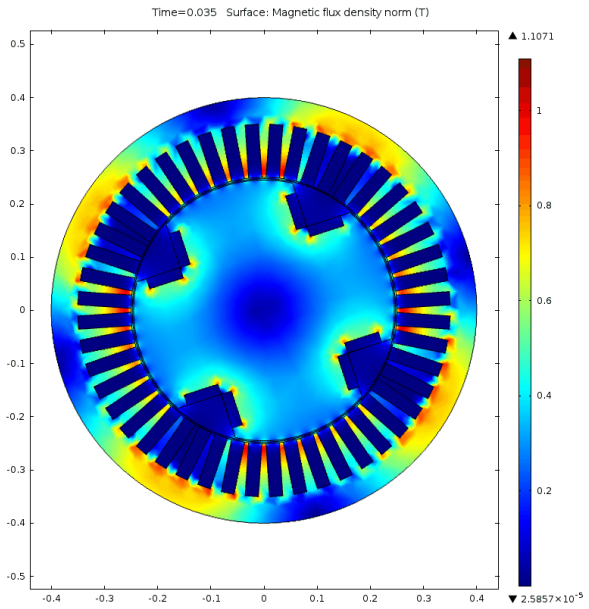

(a) Magnetic flux density distribution

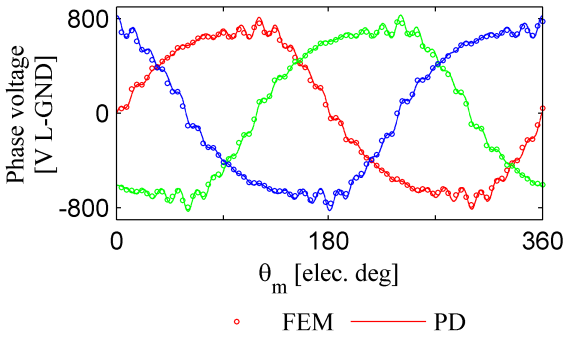

(b) Stator voltage

Figure 4.9: Comparison of the FEM and PD model - Nonlinear case.

Other symmetries considerations have been discussed by Poltschak *et al.* [32].

Stator neutral point connection: Usually armatures windings are delta or wye with the neutral point not grounded. In that case, it is possible to reduce the dimension of the current vector by one. For example, a three-phase electrically-excited machine will require only four 4-D lookup tables.

Operating conditions: Only the points corresponding to the possible operating conditions need to be calculated. For example, when the field current is tightly regulated to 1 pu (See section 3.2.5), there is probably no need to fill up the lookup table for field current values under 0.8 pu. Or in the case of speed control: when the d-axis current is regulated to 0 pu (See section 3.2.5, there is generally no need to fill up the lookup table for d-axis current values over 0.2 pu.

4.8 Summary

In this chapter, we discussed the implementation of the phase-domain model with lookup tables.

In the linear case, we have shown that the implementation with flux linkage as state variable is the fastest in terms of computation speed. An efficient and accurate way to represent the space harmonics is to use 1-D lookup table for the rotor angle dependant inductance matrix and N-D lookup table for the electromagnetic torque. We have examined the execution time and the error introduced by the lookup tables taking the classical dq-model as reference.

In the nonlinear case, to overcome difficulties linked with the inductance concept, we have investigated an implementation with an N-D lookup table. This table describes the winding currents as function of the rotor angle and the winding flux linkages. It has been constructed from the N-D lookup table describing the winding flux linkages as function of the rotor angle and the winding currents. We use a N-D lookup table for the electromagnetic torque.

We also summarized the expressions that have been used to calculate the phase-domain parameters (flux linkage and electromagnetic torque) with the fi-

nite element method. Then, we have presented a flexible implementation of this model into Matlab/Simulink. Finally, we have validated both linear and nonlinear models through comparison with a finite element model.

Chapter 5

Grid-connected superconducting wind turbine generator simulation and analysis

Objectives: Simulate and analyze grid-connected superconducting wind turbine generators.

Motivations: Absence of guidelines for superconducting machine designers (see section 1.1).

Contributions: Analysis of grid-connected superconducting wind turbine generator transient behavior, discussion on the resulting torque, discussion on transient current margins, estimation of the steady-state AC losses.

5.1 Resulting torque

In sections 2.2.1.3 & 2.2.1.5, we underlined that there are concerns that the space harmonics, the time harmonics and the low synchronous reactance might lead to mechanical vibrations or high transient resulting torque dT on the shaft of the machine. This could damage the generator if the machine shaft is not designed to withstand such efforts on a daily basis.

We examine here the mechanical vibrations and transient resulting torque of the two grid-connected superconducting wind turbine generators described in section 2.4.

5.1.1 Model and sequence

We use only the WECS model. It is modeled with the averaged full WECS model described in section 2.3.2. The simulation sequence is the same as the one described in Appendix A.2: startup from t= 0 s to t= 30 s, sudden wind variations from t= 30 s to t= 50 s, and low-voltage ride-through t= 50 s to t= 60 s. The WECS model time step is set to 5e-5 s.

5.1.2 Results

Generator-side converter waveforms are shown on Fig.5.1 for the ironless generator, and on Fig.5.2 for the non-salient pole generator. They can be compared to the reference 2 MW model on Fig.3.3. Grid-side converter waveforms are similar to the reference model (Fig.3.4) and are not included here. P_m is the mechanical power extracted from the wind. P_e and Q_e are the generator active and reactive power (from the machine to the converter). ω_m is the rotor mechanical speed. i_f is the field current.

Fig.5.1.2 shows the mechanical torque T_m, the electromagnetic torque T_e and the resulting torque $dT = T_m + T_e$ (T_{damp} is neglected), for the two generators during the whole sequence.

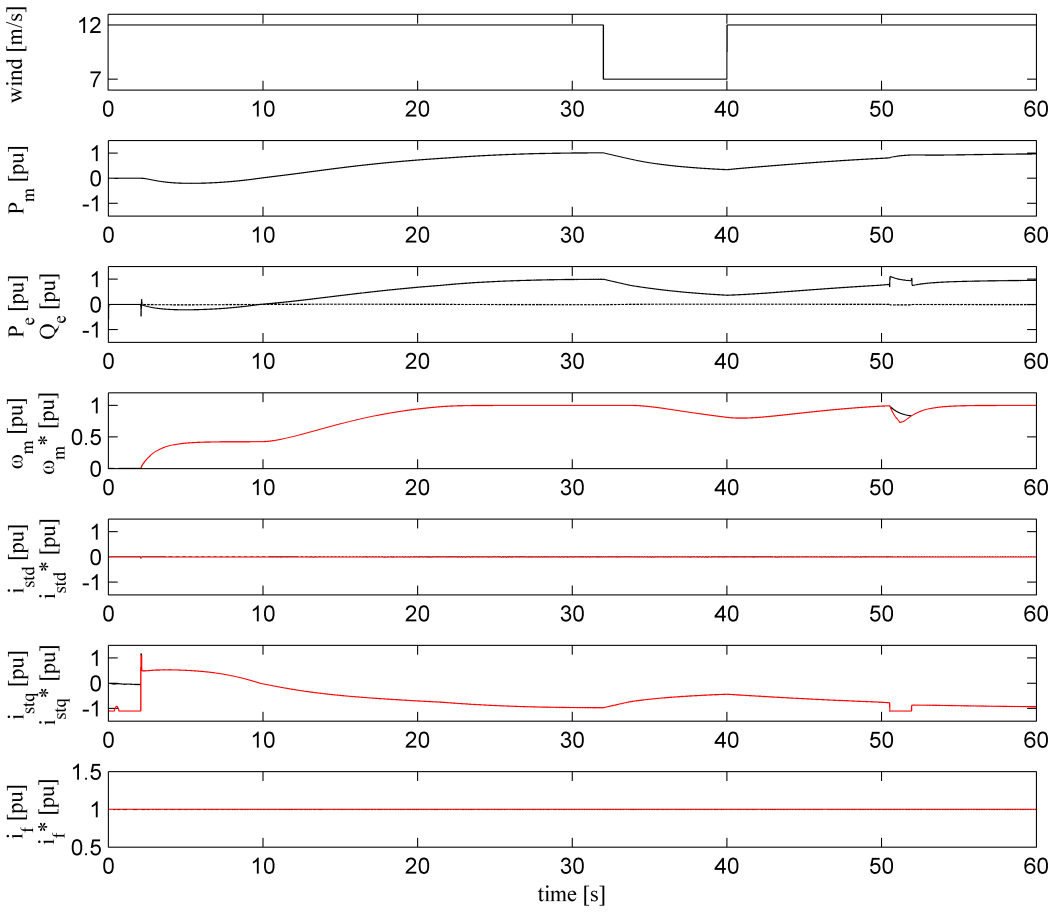

Figure 5.1: Analysis of the mechanical vibrations - Ironless generator.

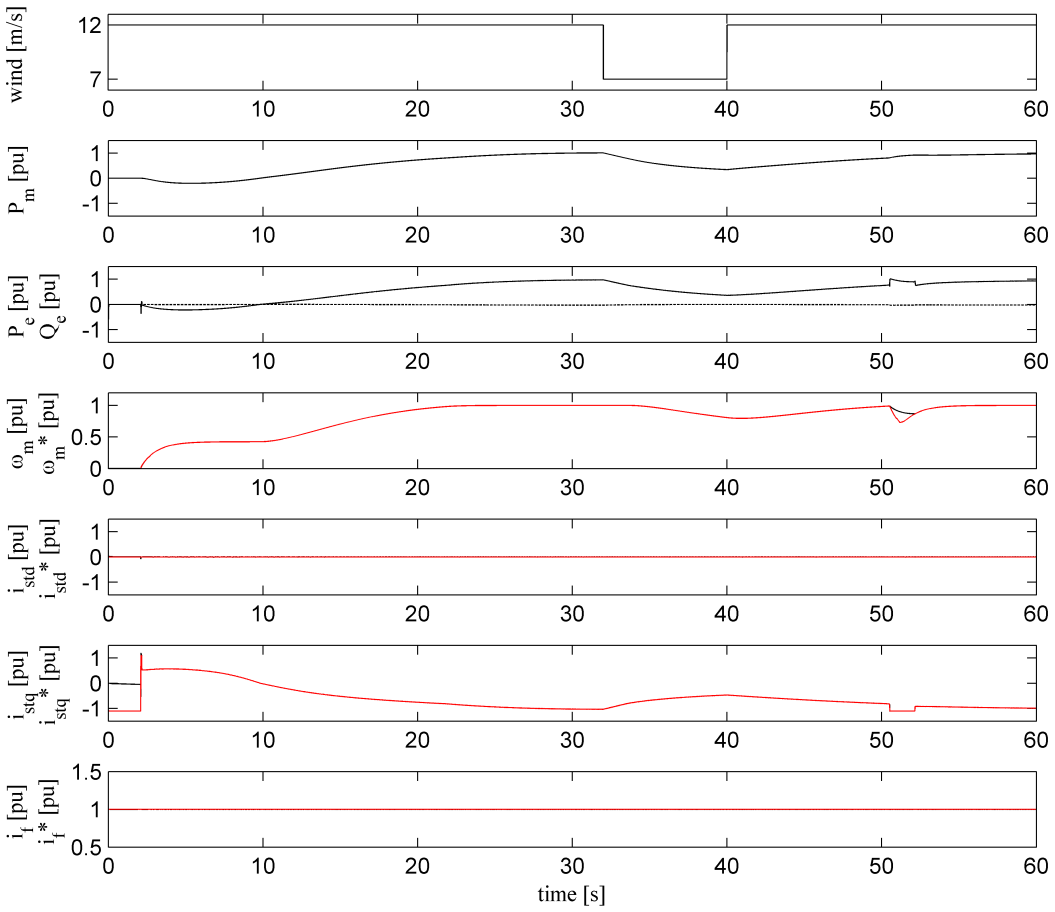

Figure 5.2: Analysis of the mechanical vibrations - Non-salient pole generator.

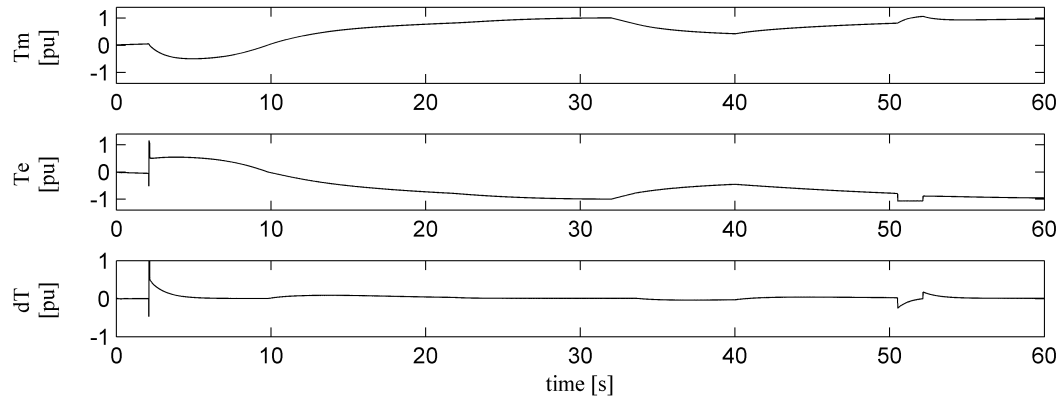

(a) Ironless generator

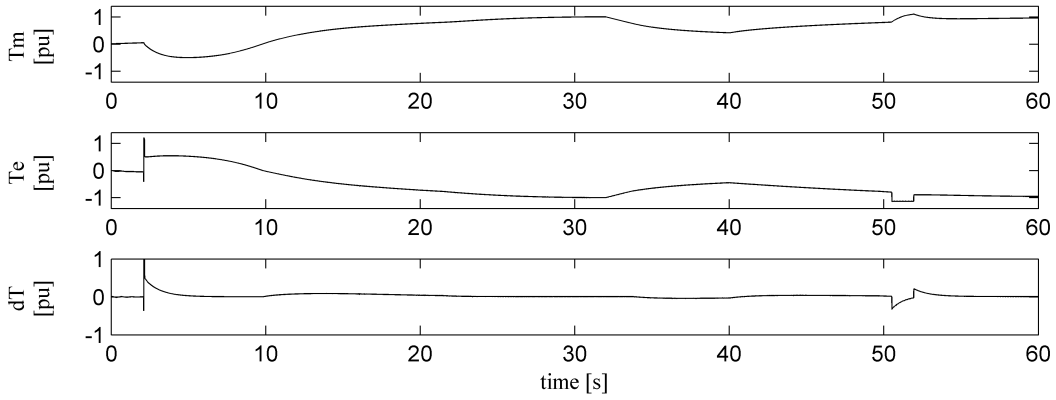

(b) Non-salient pole generator

Figure 5.3: Analysis of the transient resulting torque.

5.1.3 Discussion

We observe no mechanical oscillations for the two generator designs. The generator speed follows tightly the speed reference. Besides, we observe a good decoupling between the d- and q-axis of the machine in comparison with the reference 2 MW model (Fig.3.3). This is attributed to the low value of the d- and q-axis magnetizing inductances. We underline that these results include the impact of the generator space harmonics and saturation (phase-domain model), the time constants associated with the power electronics (averaged model), the turbine inertia and the drive train stiffness (two-mass model drive train).

Following Fig.5.1.2, the maximal dT is experienced at startup. It reaches 1.26 pu for the ironless generator and 1.2 pu for the non-salient pole generator. It results from the q-axis current reference step when the converter is switched on. A smoother starting procedure could reduce the mechanical stress during startup. During sudden wind variations, the resulting torque results from the quick mechanical torque variation. It stays under 0.1 pu. But, during LVRT, the resulting torque results from the quick electromagnetic torque variation. It reaches -0.33 pu for the ironless generator and -0.26 pu for the non-salient pole generator. This should be taken into account when designing the mechanical part of the generator.

5.2 Transient current margins

In sections 2.2.1.1 & 2.2.1.2, we underlined that the field current is a critical parameter for the safe operation of superconducting machines. Indeed to ensure that the machine will operate in superconducting state, the winding maximal current I_{max} must stay under the critical current I_c, the maximal magnetic flux density seen locally by the winding B_{max} must stay under the critical magnetic flux density B_c, and the winding maximal local temperature T_{max} must stay under the critical temperature T_c. Taking this into consideration, the designers usually first set the operating temperature. Then to ensure that both $I_{max} < I_c$ and $B_{max} < B_c$ will be respected in transient conditions, they set the superconductor nominal current applying a safety factor called current margin. As there is yet

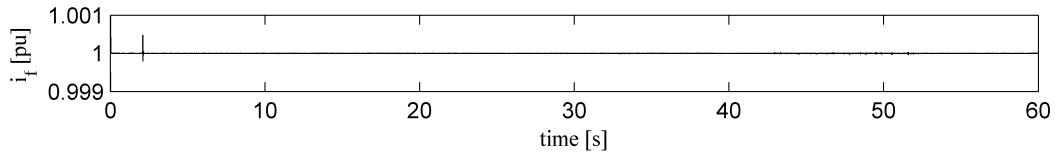

(a) Ironless generator

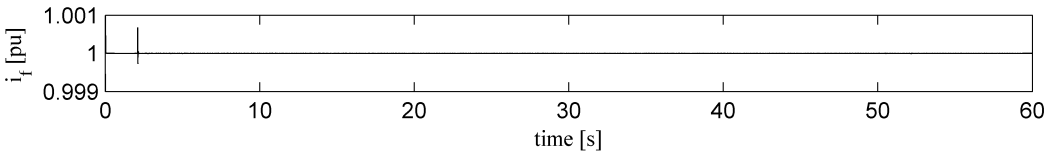

(b) Non-salient pole generator

Figure 5.4: Analysis of the current margins.

no guideline on how to choose the current margin, the nominal current is usually arbitrarily set to 0.8 I_c [76]. The larger the current margin, the higher the required tape length and thus the price of the generator. Therefore the choice of the current margin has a significant impact on the generator cost.

We estimate here the transient current margins of the two grid-connected superconducting wind turbine generators described in section 2.4.

5.2.1 Model and sequence

Model and sequence are similar to section 5.1.

5.2.2 Results

Fig.5.2.2 shows the field current i_f, for the two generators during the whole sequence.

5.2.3 Discussion

Following Fig.5.2.2, it is shown the field current can be tightly regulated to the nominal current for all the operating conditions by controlling the field current with the exciter. Assuming constant operating temperature, we can conclude that the superconducting coil operating point stays within safety margins, and

that it can be protected from quench and thermal run away even during severe transients.

5.3 Steady-state AC losses

In sections 2.2.1.1, 2.2.1.2 & 2.2.1.6, we underlined that the heating losses induced in the superconducting windings from AC currents and fields (AC losses) are a critical parameter for the design of superconducting machines. At the conception level, an estimation of the steady-state AC losses would enable a more precise estimation of the total system efficiency and weight (including cryocoolers). Such an estimation could allow machine designers to develop advanced machine designs and AC losses mitigation techniques. However, to our knowledge, a method to quantitatively estimate steady-state AC losses of a superconducting wind turbine generator has not yet been reported.

We estimate the steady-state AC losses of the two grid-connected superconducting wind turbine generators described in section 2.4.

5.3.1 Model and sequence

The models used in this section are WECS model, the machine model and the HTS tape model described in section 2.3.2. The WECS is modeled with the detailed half WECS model described in section 2.3.2. The exciter is modeled with an average model. Thus, the high frequency harmonics linked to the exciter power electronics are not included. But the time constant linked to the exciter controller is included. The generator-side converters is modeled with a detailed model. Thus, the high frequency harmonics linked to the pulse width modulation (PWM) are included as well as the time constants linked to the controllers. The generator is modeled with the nonlinear phase-domain model. Thus, effects linked to both space harmonics and saturation are included.

We are interested only in the steady-state AC losses. From startup to steady-state, the WECS simulated time is 31 s. Considering the machine model symmetries, we export only one third of the electrical period, ie. 0.33 s, from the WECS model. This steady-state sequence is called T_C. But to ensure that $\nabla.B$=0 with

the H-formulation, zero field is required at the simulation startup t_0. This means $H_x(t_0)$=0, $H_y(t_0)$=0 and $i_t(t_0)$=0 for the HTS tape model. This is obtained when $i_{abc}(t_0)$=0 and $i_f(t_0)$=0 in the machine model. Therefore, we build two artificial sequences T_A and T_B for both the machine model and the HTS tape model. T_A is an initialization sequence of 0.01 s during which i_{abc} and i_f increase from zero to their steady-state values. This creates an artificial increase of the dissipated power. Therefore we insert a waiting sequence T_B of 2.29 s to allow for flux relaxation [91; 92] before starting the steady-state sequence T_C. Fig.5.5 shows the full sequence for the ironless generator.

The highest frequency of interest is the PWM frequency f_{PWM}. Therefore the WECS model output time step, the machine model solver time step and the tape model solver time step are set to $\frac{1}{4f_{PWM}}$ Hz.

5.3.2 Results

We calculate the dissipated power during the whole sequence for each one of the selected $n_{t,0}$ tapes. We selected 264/40204 tapes for the ironless generator and 135/17625 tapes for the non-salient pole generator (see Appendix C and D).

Fig.5.6 illustrates the dissipated power during T_C for three selected tapes for the ironless generator. We observe that the dissipated power is positive at the begining of T_C and has a negative derivative. This can be explained by considering the tape current distribution and the E-J law. When the field coil current is ramped up, the coil self field changes, and intra-tape screening currents are induced. The magnitude of these screening currents varies with the position of the tape within the coil, and tends to increase in the tapes situated near the edges. This mechanism is similar to the one causing coupling currents in LTS magnets [93; 94; 95]. After the ramping up, the superposition of screening currents and transport current leads to an inhomogeneous current distribution. We plot in Fig.5.7 the current distribution averaged over the tape thickness for the three tapes. The dissipated power is then obtained from the current distribution and the E-J law. As we use an E-J power law, the product $E_z J_z$ is never zero (positive dissipated power), and decays slowly because of flux creep (negative derivative) [92; 96].

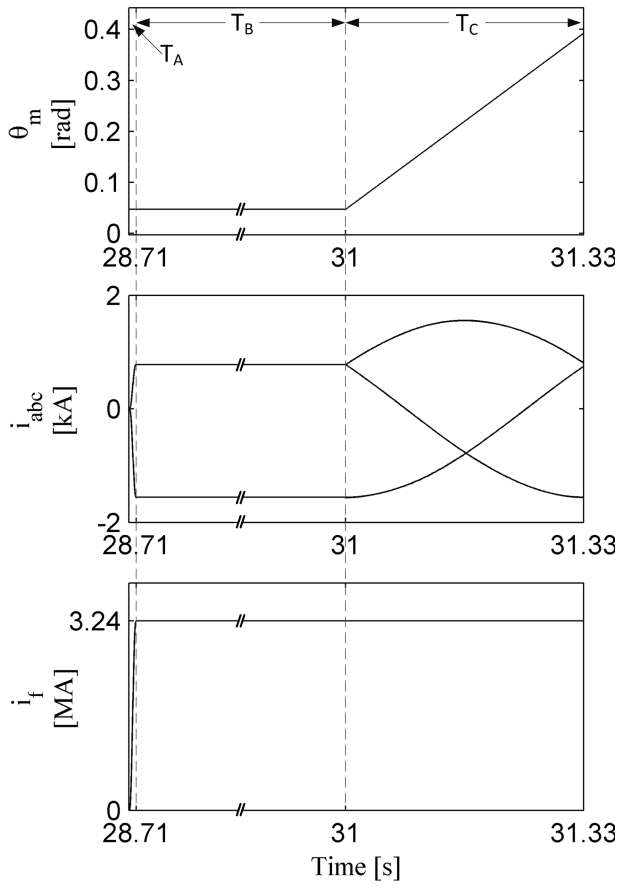

Figure 5.5: Sequence for machine model and HTS tape model for AC losses calculation - Ironless generator.

Here, we explain how to estimate the AC losses from the dissipated power. The dissipated power has two components. The first component is linked to the machine operating point, its history and to the real E-J relationship. In our simulation, this component is similar to the "offset" plotted by dashed line in Fig.5.6. The second component is linked to the time-varying transport current and applied field: this is the instantaneous AC losses. The "offset" influences the AC losses and vice versa. But to simplify, we assume that the dissipated losses are the sum of the two components [97; 98]. Then, the instantaneous AC losses can be approximated by substracting the "offset" from the dissipated power (Fig.5.8). Note that by doing this, we tend to overestimate the instantaneous AC losses.

After calculating the instantaneous AC losses for the $n_{t,0}$ tapes, we take the average AC losses over one cycle, and we interpolate the results to the other tapes of the coil. Resuls are shown in Fig.5.9 for the ironless generator and in Fig.5.10 for the non-salient pole generator. (i,j) is the position of the tape within the coil cross section. The markers show the position of the three tapes in Figs.5.6 and 5.8. Note that AC losses are larger in the tapes located near the stator. Finally, we calculate the average AC losses for the coil cross section by adding all the average tape AC losses.

For the ironless generator, the estimated average AC losses for the coil cross section are 2.1 W/m. The generator has 12 poles and an effective length of 1.2 m. Thus, the steady-state average AC losses for the ironless generator are about 60.5 W. For the non-salient pole generator, the estimated average AC losses for the coil cross section are 2.6 W/m. The generator has 12 poles and an effective length of 1.6 m. Thus, the steady-state average AC losses for the non-salient pole generator are about 99.8 W.

We use a personal computer (Intel XEON X5650, 2.67 GHz, 2 processors). The computation time for the WECS model and the machine model are about 20 minutes (sequence length 1 s from steady-state) and 20 minutes, respectively. The computation time for the HTS tape model is about 380 s per tape (export, postprocessing and one AC losses calculation on one processor). Therefore the total computation time is about 14.5 hours for the ironless generator and 8 hours for the non-salient pole generator.

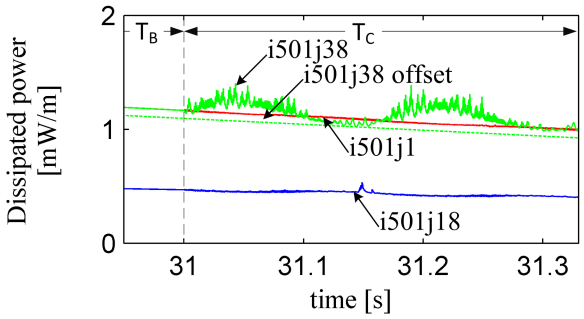

Figure 5.6: Tape dissipated power - Ironless generator.

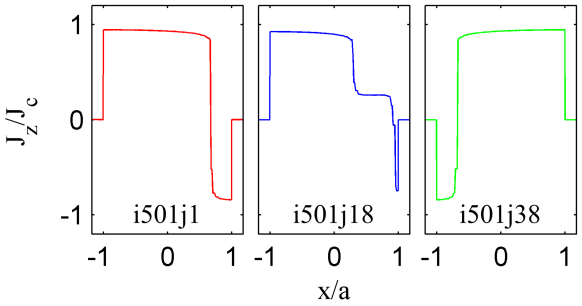

Figure 5.7: Tape current distribution - Ironless generator.
This is the current distribution at t=31 s averaged over the tape thickness.

5.3.3 Discussion

The machine model assumes uniform current density over the whole coil cross section, while the HTS tape model considers the actual tape geometry and current distribution. Besides, the coupling boundary is close to the tape. Therefore the imposed boundary condition might lead to divergeance of the HTS tape model if the model does not have enough degrees of freedom. The choice of the mesh and the element order is a compromise between stability and computation time. We found that the by using a single layer rectangular mesh with 75 elements in the superconducting region and first order elements [59; 64], our model converged for 93% of the tapes. When it did not converge, we determined the tape average AC losses value by interpolation along the column.

The adopted method allows us to include the contribution of the other tapes current and field when calculating AC losses of each tape. But it doesn't allow us to include effects linked to the fact that the other tapes are superconducting : the

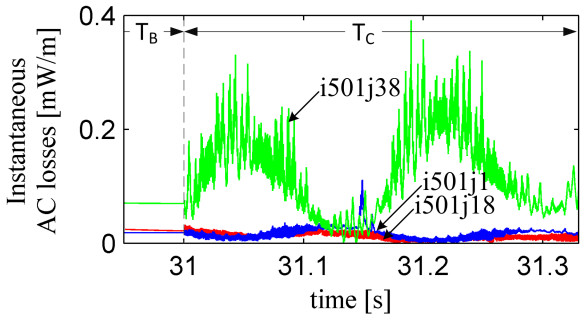

Figure 5.8: Tape instantaneous AC losses - Ironless generator.

tapes in the middle of a stack should have lower AC losses than the tapes at the extremities [58]. For a 20-tape stack having small intertape distance, Prigozhin *et al.*[61] showed that the AC transport current losses of the top/bottom tapes can be 15% higher than the ones in the middle of the stack. Therefore, we might overestimate the AC losses by neglecting the "stack effect". However, the influence of the combination of the DC transport current and the applied magnetic field on the AC losses of an array of tapes should be investigated properly. Besides, Iwakuma *et al.*[99] used such kind of approximation -but neglecting the transport current- for a 1 MVA superconducting transformer using Bi2223 conductors. They reported that measured AC losses and estimated AC losses agreed within an error of 30%. As transformer and machines have different operating conditions, the proposed method should be seen as an hypothesis that needs to be confirmed by experiment.

The main advantage of our method is that it uses the results of conventional electromagnetic FE analysis as input for AC losses calculation. Estimation of AC losses only requires several solutions of the HTS tape model. We would like to add that this method could be used as it is for the calculation of AC losses during a transient response : sudden wind change, stator fault, grid fault, converter failure, etc. The unique limitation would be the total calculation time.

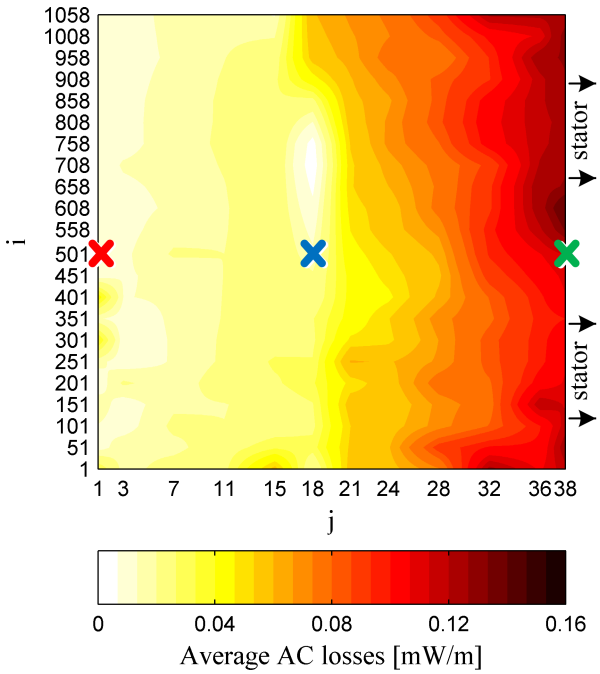

Figure 5.9: Tape average AC losses - Ironless generator.

5.4 Other possible applications

In this section, we discuss the other possible applications or extensions of such a multiscale simulation.

Special worst case scenario: The worst case scenarios considered in this thesis are scenarios that could happen every day. The wind turbine could have start everyday following the wind conditions or the grid requirements, winds are constantly fluctuating, and grid codes require low-voltage ride-through capability. Such a multiscale simulation could be used to study special worst case scenarios too, such as a fault between the machine stator and the generator-side converter.

HTS tape with magnetic substrate: In this thesis, we modeled only the HTS layer in the HTS tape model. We underline that the H-formulation can include magnetic substrates [90].

Transient AC losses: The method could be used as it is for the calculation of

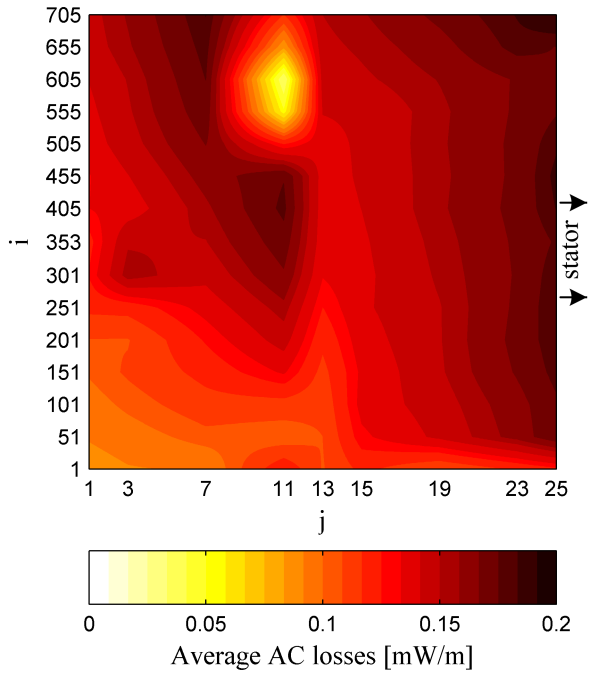

Figure 5.10: Tape average AC losses - Non-salient pole generator.

AC losses during a transient response including sudden wind change, stator fault, grid fault, converter failure, etc. The unique limitation would be the total calculation time.

Damper design: Dampers could help to reduce the steady-state AC losses by providing a shield against the AC fields coming from the stator side. Dampers effectiveness as well as other AC losses mitigation techniques could be evaluated with such a tool.

Thermal model: The estimation of the current margins in section 5.2 assumes that the operating temperature of the machine is constant. A thermal model could be coupled to the multiscale simulation to determine if the winding maximal local temperature stays under the critical temperature.

Mechanical model: The estimation of the resulting torque on the shaft of the machine in section 5.1 could be used as input of a mechanical model of the machine shaft.

Machines drives analysis: The method can be extended to any machine drive system to study the impact of external mechanical and electrical systems on the machine operation: losses associated to PWM, magnet demagnetization, etc.

Advanced control: Thanks to the capability of nonlinear phase-domain model in representing the machine model with accuracy in the WECS model, the unidirectional coupling stays valid for any machine. Therefore, this method can be used to design advanced controller for machines having space harmonics and saturation.

5.5 Summary

In this chapter, we evaluated the transient behavior of grid-connected direct-drive 10 MW class superconducting wind turbine generators during startup, sudden wind variations and low-voltage ride-through. Analysis focused on three key parameters for the design of superconducting wind turbine generators.

First, we considered the resulting torque on the shaft. We did not observe mechanical oscillations during transients for the given generators. But we have underlined that the shaft of the machines can endure high resulting torque during transients, and therefore needs to be designed adequately.

Secondly, we investigated the transient current margins for the superconducting coil. We have demonstrated that the current variations in the superconducting coil can be kept very low, and therefore that it can be protected from quench and thermal run away.

Thirdly, we calculated the steady-state AC losses in the superconducting windings.

We underline that the estimation includes effects linked to the turbine inertia, the shaft stiffness, the generator space harmonics and saturation, the exciter control, and the AC/DC/AC converter PWM and control.

Finally, we discussed the other possible applications or extensions of such a method: damper design, fully superconducting generator AC losses estimation, advanced controller design, etc.

Chapter 6

Conclusions

Superconducting machines have been proposed to solve the problem of upscaling wind turbine generators. Considering the need for superconducting machine designers of an accurate, efficient and flexible tool to study the interactions between the machine and external systems, we developed a numerical model for the steady-state and transient analysis of grid-connected superconducting wind turbine generators.

The adopted method is a multiscale simulation constituted by three models with unidirectional couplings: a lumped-parameter wind energy conversion system model, a FE machine model and a FE HTS tape model. The multiscale simulation allows us to obtain the desired level accuracy, while the unidirectional couplings bring high efficiency. The models have been implemented in a flexible way using commercial softwares (Matlab/Simulink and Comsol Multiphysics), a key to bringing development of superconducting machines from the laboratory scale to the industrial level.

To model the wind energy conversion systems, we used Matlab/Simulink. The model includes the wind turbine generator, the external mechanical systems, the external electrical circuits and associated control strategies. First, we summarized special characteristics of superconducting machines, particular needs of offshore wind farms and grid regulations. From this, we determined that a full-scale 3-level NPC back-to-back converter would be an adapted configuration for the correct operation and optimal grid integration of superconducting wind turbine generators. Secondly, we summarized the equations for the systematic design

and control of a back-to-back converter for direct-drive electrically-excited synchronous generator-based WECS. We used it to build a reference 2 MW WECS model. And we evaluated its performances for three worst case scenarios: startup, sudden wind variations and low-voltage ride-through.

To model the superconducting machine in the time domain transients simulation, we used a nonlinear coupled finite element phase-domain model. On the one hand, the machine parameters are obtained from static nonlinear finite element analysis (Comsol Multiphysics). On the other hand, the machine is represented by a lumped-parameter phase-domain model (Matlab/Simulink). This approach offers two main advantages. First, as opposed to the classical dq-model, the phase-domain model can naturally include both space harmonics and saturation, two important features of multi-MW superconducting wind turbine generators. Secondly, it provides a reasonable simulation speed with the same accuracy as a full finite element model. Previous implementations of the phase-domain model being rather complex because of the use of the inductance concept, we proposed a novel general nonlinear phase-domain model using N-dimensional lookup tables. The lookup tables describe the winding currents as function of the rotor angle and the winding flux linkages. They are constructed by N-dimensional interpolation from the lookup tables which describe the winding flux linkages as function of the rotor angle and the winding currents. The flux linkage is calculated using the vector potential. Another lookup table describes for the electromagnetic torque. It is directly calculated using the Maxwell stress tensor. We presented a flexible implementation of this model into Matlab/Simulink/SimPowerSystem. And we validated it through comparison with the dq-model and the finite element model.

The HTS tape model is a finite element model of only one tape with H-formulation and edge elements implemented with Comsol Multiphysics PDE mode application. It takes into consideration the properties and the real thickness of the tape.

Finally, we demonstrated the versatility of the adopted method by simulating two different grid-connected 10 MW class superconducting wind turbine generators. The analysis focused on estimating critical parameters for the design of the machine such as resulting torque, transient current margins, and steady-state AC losses. We underlined that the shaft of the machine can endure high result-

ing torque during transients, and therefore needs to be designed adequately. We demonstrated that the current variations in the superconducting coil can be kept very low with the adopted power electronics, and therefore that it can be protected from quench and thermal run away. We calculated the steady-state AC losses in the superconducting windings, including effects linked to the exciter, the AC/DC/AC converter PWM and the control strategy. To solve the problem linked with the high number of tapes in the superconducting coil cross section, we considered that the AC losses calculated for several tapes only could be interpolated to the others. Finally, we have discussed the other possible applications of such a method: damper design, advanced controller design, etc.

Appendix A

WECS data

A.1 Back-to-back converter data

A.2 Reference WECS scenarios

We define three operating scenarios: startup, sudden wind variations and low-voltage ride-through. They are designed as worst case scenarios that could happen on a daily basis.

A.2.1 Startup

During the whole startup sequence, the wind speed is set to the rated speed 12 m/s, and the grid voltage is set to 1 pu. Initially, the generator speed is zero and the DC-link capacitor is discharged. We suppose that the field coil has already been energized. At t= 1 s, the grid-side converter is switched on. At t= 2 s, the generator-side switch is opened. At t= 2.1 s, the generator-side converter is switched on. To reach steady-state (t= 30 s), the generator-side controller will need to increase the generator speed from 0 pu to 1 pu. The grid-side converter will need to keep the DC-link voltage to its nominal value.

Table A.1: Back-to-Back Converter Parameters

Name	Parameter	Value
Power converter nominal power	P_{nom}	$P_{nom,gen}$
Grid-side converter nominal voltage	$v_{nom,grid}$	$v_{nom,gen}$
Grid-side converter nominal frequency	$f_{nom,grid}$	60 Hz
Line reactor resistance	R_r	$0.15/f_{nom,grid}$ pu
Line reactor inductance	L_r	0.15 pu
PWM frequency	f_{PWM}	1080 Hz
Exciter frequency	f_{field}	f_{PWM}
Wind turbine inertia constant	H_{tur}	4.32 s
Shaft spring constant	K_{tur}	0.3 pu
Shaft mutual damping	D_{tur}	1.5 pu

A.2.2 Sudden wind variations

During the whole sudden wind variations sequence, the grid voltage is set to 1 pu. Initially, the system is in steady-state operation as described above. Large artificial wind steps are introduced. At t= 32 s, the wind suddenly drops from 12 m/s to 7 m/s. Then at t= 40 s, the wind increases from 7 m/s to 12 m/s. The generator-side controller will need to adapt the generator speed to maximize the power capture (MPPT). The grid-side converter will need to keep the DC-link voltage to its nominal value.

A.2.3 Low-voltage ride-through

One of the most restrictive requirement of new grid codes is the low-voltage ride-through (LVRT) capability. It implies that when there is a transformer high side fault, the wind turbine generator must stay online, ride through the fault, and be able to recover quickly to full rated power when the fault is cleared. This is particularly meaningful for the operation stability of power systems with high percentage of wind power penetration.

The grid code used in this study is similar to the one of E.On Netz in Germany [52]. Wind turbines must remain connected when the voltage at the onshore grid coupling point stays above the line shown on Fig.A.1. As the VSC-HVDC will facilitate the compliance to the LVRT requirements, we consider that the worst

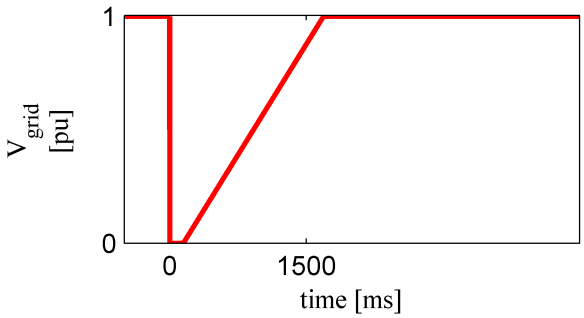

Figure A.1: Low-voltage ride-through grid code.

case scenario is when the offshore grid voltage follows the line on Fig.A.1. Note that we do not consider operation for prolongated low grid voltage.

During the whole LVRT sequence, the wind speed is set to the rated speed 12 m/s. Initially, the system is in steady-state operation as described above. During the fault, this situation represents the worst case scenario because the difference between the power extracted from the wind P_m and the power transferred to the grid P_{grid} is maximal. At t= 50.5 s, the grid voltage drops. At t= 52 s, the grid voltage returns to 1 pu. The converter will have to ensure that the system can stay online, and ride through the dip voltage.

Appendix B

2 MW conventional generator data

B.1 dq-model parameters

Note that the rotor quantities are referred to stator.

B.2 WECS tuning

The PI parameters are obtained from Tab.3.1 and summarized in Tab.B.2.

ω_c is the open loop crossover frequency, a is a design parameter in the range $\{2, 4\}$, f_b is the -3 dB bandwidth frequency of the closed loop transfer function. Note that the tuning goals (see section 3.2.12) are respected.

Table B.1: Reference WECS Parameters

Parameter	Value
$P_{nom,gen}$	2 MW
$v_{nom,gen}$	690 $V_{LL,RMS}$
$f_{nom,gen}$	60 Hz
R_s	0.006 pu
L_{ls}	0.18 pu
L_{md}	1.125 pu
L_{mq}	0.294 pu
R'_f	7.4103 $.10^{-4}$ pu
L'_{lf}	0.1293 pu
P	60
H_{gen}	0.62 s
F	0.01 pu

Table B.2: Controller Parameters

	ω_c (rad.s^{-1})	a –	K_p (si)	T_i (s)	f_b (Hz)
$G_{c,r}$	339	3.18	3.2 $.10^{-2}$	9.4 $.10^{-3}$	87
$G_{c,v}$	48	3	-5.5	62.5 $.10^{-3}$	12.5
$G_{c,d}$	339	3.18	105.4	9.4 $.10^{-3}$	87
$G_{c,q}$	270	4	30.5	14.8 $.10^{-3}$	65.6
$G_{c,f}$	339	3.18	0.3	9.4 $.10^{-3}$	87
$G_{c,w}$	27	4	10.0 $.10^4$	0.15	6.5

Appendix C

10 MW ironless generator data

C.1 Geometry

An overview of the ironless generator is shown on Fig.C.1. Details on the dimensions of the generator can be found in [55].

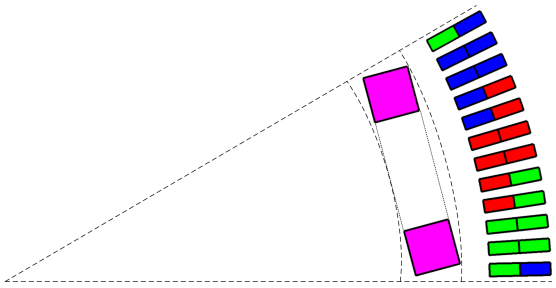

Figure C.1: Overview of the ironless generator.

C.2 Coupled FE phase-domain model

For the N-dimensional lookup tables of the phase-domain model, we calculated the flux linkage and the electromagnetic torque for a rotor angle from 0 to 60 deg in steps of 1.25 deg, a field current from 3078000 to 3402000 A in steps of 324000 A,

and phase currents from -1633 to 1633 A in steps of 3266 A. Fig.C.2 compares the armature voltage obtained by transient finite element method (FEM) with the dq-model (dq), and the coupled FE phase-domain model (PD).

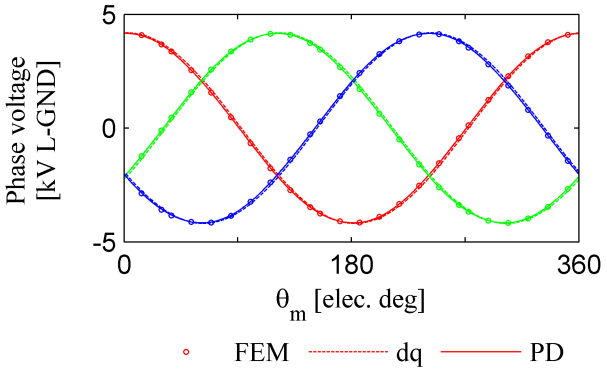

Figure C.2: Comparison of FEM, dq and PD model - ironless generator.

C.3 dq-model parameters

The machine dq-model parameters are approximated by finite element analysis. Note that the rotor quantities are not referred to stator. R_f is the equivalent resistance of the field coil. The superconducting coil itself has no resistance, but exciter switches and connections do have resistance. R_f is set to $1e-4\ \Omega$ [84].

C.4 Superconducting coil properties

For this generator, the field coil has a cross section of 180 mm x 180 mm. Considering the HTS tape model described in section 2.5, there are 40204 turns (38 x 1058 tapes). The field coil current is 3.24e6 A ($J_{e,op}$ = 1e8 A/m^2). Therefore each tape carries a current of 80.6 A. At 22 K, this is 56 % of the tape critical current [63].

For the AC losses calculation, we calculated 264 times the AC losses of one tape alone, and we interpolate the results to the other 38940 tapes. The 264 tapes are selected arbitrarly. Considering the coil cross section, the tapes have

Table C.1: Machine dq-model Parameters

Parameter	Value
$P_{nom,gen}$	10 MW
$v_{nom,gen}$	5 $kV_{LL,RMS}$
$f_{nom,gen}$	1 Hz
R_s	0.008 pu
L_{ls}	0.0402 pu
L_{md}	0.0063 pu
L_{mq}	0.0063 pu
R_f	4 $.10^{-5}$ pu
L_{lf}	3.265 $.10^{-6}$ pu
P	6
H_{gen}	0.62 s
F	0.01 pu

an array structure. Let their position be numeroted from the bottom left corner by two indices (i,j). We select tapes (i,j) $\in$ {1 51 101 151 201 251 301 351 401 451 501 558 608 658 708 758 808 858 908 958 1008 1058}x{1 3 7 11 15 18 21 24 28 32 36 38}.

Appendix D

10 MW non-salient pole generator data

D.1 Geometry

An overview of the non-salient pole generator is shown on Fig.D.1. Details on the dimensions of the generator can be found in [76].

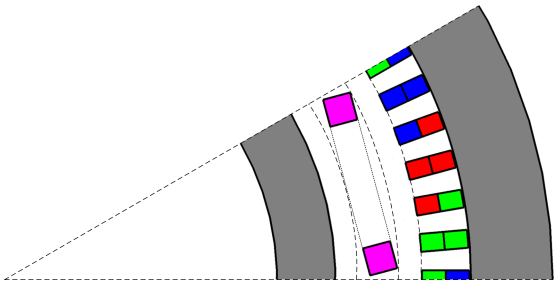

Figure D.1: Overview of the non-salient pole generator.

D.2 Coupled FE phase-domain model

For the N-dimensional lookup tables of the phase-domain model, we calculated the flux linkage and the electromagnetic torque for a rotor angle from 0 to 60 deg in steps of 2.5 deg, a field current from 1983600 to 2192400 A in steps of 208800 A, and phase currents from -2474.2 to 2474.2 A in steps of 4948.4 A. Fig.D.2 compares the armature voltage obtained by transient finite element method (FEM) with the dq-model (dq), and the coupled FE phase-domain model (PD). The saturation is included in the dq-model by using the open-circuit saturation curve [66] obtained by FE analysis.

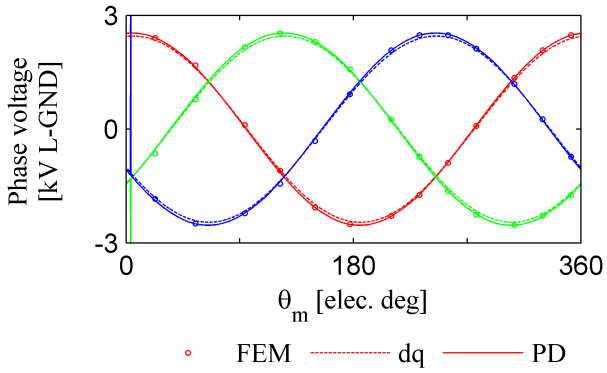

Figure D.2: Comparison of FEM, dq and PD model - non-salient pole generator.

D.3 dq-model parameters

The machine dq-model parameters are approximated by finite element analysis. Note that the rotor quantities are not referred to stator. R_f is the equivalent resistance of the field coil. The superconducting coil itself has no resistance, but exciter switches and connections do have resistance. R_f is set to $1e-4\ \Omega$ [84]. As the machine operates in saturated conditions, we used $L_{md,lin}$ and $L_{mq,lin}$ instead of L_{md} and L_{mq} for the controller decoupling and PI tuning. $L_{md,lin}$ and $L_{mq,lin}$ are the magnetizing inductances linearized around the steady-state operation point considering the open-circuit saturation curve [66].

Table D.1: Machine dq-model Parameters

Parameter	Value
$P_{nom,gen}$	10 MW
$v_{nom,gen}$	3.3 $kV_{LL,RMS}$
$f_{nom,gen}$	1 Hz
R_s	0.022 pu
L_{ls}	0.0265 pu
L_{md}	0.0122 pu
L_{mq}	0.0122 pu
$L_{md,lin}$	0.0102 pu
$L_{mq,lin}$	0.0102 pu
R_f	9.183 $.10^{-5}$ pu
L_{lf}	1.132 $.10^{-5}$ pu
P	6
H_{gen}	0.62 s
F	0.01 pu

D.4 Superconducting coil properties

For this generator, the field coil has a cross section of 120 mm x 120 mm. Considering the HTS tape model described in section 2.5, there are 17625 turns (25 x 705 tapes). The field coil current is 2.088e6 A ($J_{e,op}$ = 1.45e8 A/m^2). Therefore each tape carries a current of 118.5 A. At 22 K, this is 82 % of the tape critical current [63].

For the AC losses calculation, we calculated 135 times the AC losses of one tape alone, and we interpolate the results to the other 17490 tapes. The 135 tapes are selected arbitrarly. Considering the coil cross section, the tapes have an array structure. Let their position be numeroted from the bottom left corner by two indices (i,j). We select tapes (i,j) $\in$ {1 51 101 151 201 251 301 353 405 455 505 555 605 655 705}x{1 3 7 11 13 15 19 23 25}.

Publications and conferences

Papers

- **L. Queval**, H. Ohsaki, "AC losses of a grid-connected superconducting wind turbine generator," *IEEE Trans. on Applied Superconductivity*, accepted for publication, 2012.

- **L. Queval**, M. Sekino, H. Ohsaki, "A coupled FE phase-domain model for superconducting synchronous machine," *IEEE Trans. on Applied Superconductivity*, vol. 22, no. 3, pp. 52008+4, 2012.

International conferences

- **L. Queval**, H. Ohsaki, "Back-to-back converter design and control for synchronous generator-based wind turbines," *Int. Conf. on Renewable Energy Research and Applications (ICRERA2012)*, Nagasaki, Japan, Nov. 2012.

- **L. Queval**, H. Ohsaki, "Study on the implementation of the phase-domain model for rotating electrical machines," *15th Int. Conf. on Electrical Machines and Systems (ICEMS2012)*, Sapporo, Japan, Oct. 2012.

- **L. Queval**, H. Ohsaki, "AC losses of a grid-connected superconducting wind turbine generator," *2012 Applied Superconductivity Conf. (ASC2012)*, id. 4LPE-02, Portland, USA, Oct. 2012.

- **L. Queval**, H. Ohsaki, "Grid integration of offshore superconducting wind turbine generators," *15th Int. Power Electronics and Motion Control Conf. (EPE-PEMC2012)*, id. 207, Novi Sad, Serbia, Sept. 2012.

- **L. Queval**, M. Sekino, H. Ohsaki, "A coupled FE phase-domain model for superconducting synchronous machine," *22nd Int. Conf. on Magnet Technology (MT22)*, id. 2EP5-5, Marseille, France, Sept. 2011.

National conferences

- **L. Queval**, H. Ohsaki, "LVRT capability of superconducting wind turbine generator," *2012 IEE-Japan Industry Applications Society Conf. (JIASC2012)*, id. R3-1-3-2, Chiba, Japan, Aug. 2012.

- **L. Queval**, M. Sekino, H. Ohsaki, "Modeling of grid-connected superconducting synchronous machines," *Proc. 85th Meeting on Cryogenics and Superconductivity in Japan (CSJ85)*, id. 2P-p09, p. 126, Kanazawa, Japan, Nov. 2011.

- **L. Queval**, M. Sekino, H. Ohsaki, "A phase-domain model for superconducting synchronous machines," *Proc. 84th Meeting on Cryogenics and Superconductivity in Japan (CSJ84)*, id. 2A-a03, p. 91, Tsukuba, Japan, May 2011.

Bibliography

[1] "World energy outlook 2011," IEA, 2011. ix, 1, 2

[2] "Global wind energy outlook 2012," GWEC, 2012. ix, 1, 2

[3] "The European offshore wind industry key trends and statistics 2010," EWEA, 2011. 1

[4] "Design limits and solutions for very large wind turbines," UpWind, 2011. 1, 25

[5] S.A. Herman, "DOWEC cost model, Implementation, DOWEC-068," DOWEC project, 2003. ix, 2

[6] L.W.M.M. Rademakers, H. Braam, M.B. Zaaijer, G.J.W. van Bussel, S.A. Herman, "Assessment and optimisation of operation and maintenance of offshore wind turbines," DOWEC project, 2003. ix, 3

[7] K. Akatsu, R.D. Lorenz, "Comparing coupled analysis with experimental results for an interior PM machine," *IEEE Trans. on Industry Applications*, vol. 45, no. 1, pp. 178-185, 2009. 27

[8] M. Liserre, F. Blaabjerg, A. Dell'Aquila, "Step-by-step design procedure for a grid-connected three-phase PWM voltage source converter," *Int. J. Electronics*, vol. 91, no. 8, pp. 445-460, 2004. 35

[9] S. Achilles, M. Poller, "Direct drive synchronous machine models for stability assessment of wind farms," *Proc. 4th Int. Workshop on Large Scale*

Integration of Wind Power and Transmission Networks for Offshore Windfarms, Billund, Denmark, 2003. 6

[10] G. Michalke, Variable Speed Wind Turbines, "Modelling, Control, and Impact on Power Systems," PhD Thesis, Darmstadt Technical University, Germany, 2008. 25, 35

[11] M Jasinski, M. P. Kazmierkowski, "Power Electronics and Motor Drives, Second edition," CRC Press, pp. 16-33, 2011. 36

[12] B. Backlund, M. Rahimo, S. Klaka, J. Siefken, "Topologies, voltage ratings and state of the art high power semiconductor devices for medium voltage wind energy conversion," *Power Electronics and Machines in Wind Applications 2009*, IEEE, pp. 1-6, 24-26 June 2009. 35

[13] C. Schauder, F. Mehta, "Vector analysis and control of advanced static VAR compensator," *IEE Proceedings-C*, vol. 140, no. 4, 1993. 7, 38

[14] A. Yazdani, R. Iravani, "A neutral-point clamped converter system for direct-drive variable-speed wind power unit," *IEEE Trans. on Energy Conversion*, vol. 21, no. 2, pp. 596-607, 2006. 6, 7, 25, 38, 40

[15] K. Maleckian, A. Shirvani, U. Schmidt, W. Schufft, "Detailed modeling of wind power plants incorporating variable-speed synchronous generator," *IEEE Electrical Power & Energy Conf. (EPEC)*, 2009. 7

[16] C. Bajracharya, M. Molinas, J.A. Suul, T.M. Undeland, "Understanding of tuning techniques of converter controllers for VSC-HVDC," *Nordic Workshop on Power and Industrial Electronics (NORPIE)*, 9-11 June 2008. 7, 37, 39

[17] G.A. Radacu, "Control of grid side inverter in a B2B configuration for WT application," Master Thesis, Aalborg University, 2008. 37

[18] R. Teodorescu, M. Liserre, P. Rodriguez, "Grid converters for photovoltaic and wind power systems," John Wiley & Sons, p. 217, 2011. 7, 39

[19] M. Liserre, R. Cardenas, M. Molinas, J. Rodriguez, "Overview of multi-MW wind turbines and wind parks," *IEEE Trans. on Industrial Electronics*, vol. 58, no. 4, pp. 1081-1095, 2011. 3, 6, 13, 21, 22

[20] A. Nabavi-Niaki, M.R. Iravani, "Steady-state and dynamic models of unified power flow controller (UPFC) for power system studies," *IEEE Trans. on Power Systems*, vol. 11, no. 4, pp. 1937-1943, 1996.

[21] A. Yazdani, R. Iravani, "Voltage Sourced Converters in Power Systems," John Wiley & Sons, 2010. 39

[22] O. Aydin, A. Akdag, P. Stefanutti, N. Hugo "Optimum controller design for a multilevel AC-DC converter system," *Applied Power Electronics Conf. (APEC)*, vol. 3, pp. 1660-1666, March 6-10 2005. 43, 45

[23] S. Preitl, R.-E. Precup, "An extension of tuning relations after symmetrical optimum method for PI and PID controllers," *Automatica*, vol. 35, pp. 1731-1736, 1999. 45

[24] J.F. Conroy, R. Watson, "Low-voltage ride-through of a full converter wind turbine with permanent magnet generator," *IET Renewable Power Generation*, vol. 1, no. 3, pp. 182-189, 2007. 6, 22, 25

[25] H. Polinder, F.F.A. van der Pijl, G.-J. de Vilder, P.J. Tavner, "Comparison of direct-drive and geared generator concepts for wind turbines," *IEEE Trans. on Energy Conversion*, vol. 21, no. 3, pp. 725-733, 2006.

[26] H. Chong, D.E. Martin, M.R. Lezama, "Transient over-voltage (TOV) and its suppression for a large wind farm utility interconnection," *Proc. Int. Conf. on Sustainable Power Generation and Supply (SUPERGEN09)*, pp. 1-7, Apr. 6-7 2009. 26

[27] D. A. Torrey, X. -M. Niu, E.J. Unkauf, "Analytical modelling of variable-reluctance machine magnetisation characteristics," *IEE Proc. Electric Power Applications*, vol. 142, no. 1, pp. 14-22, Jan. 1995.

[28] L. Wang, J. Jatskevich, H. W. Dommel, "Re-examination of synchronous machine modeling techniques for electromagnetic transient simulations," *IEEE Trans. on Power Systems*, vol. 22, no. 3, pp. 1221-1230, Aug. 2007. 27, 28

[29] L. Wang, J. Jatskevich, V. Dinavahi, H. W. Dommel, J. A. Martinez, K. Strunz, M. Rioual, G. W. Chang, R. Iravani, "Methods of interfacing rotating machine models in transient simulation programs," *IEEE Trans. on Power Delivery*, vol. 25, no. 2, pp. 891-903, Apr. 2010. 57

[30] N. A. Demerdash, T. W. Nehl, "Electric machinery parameters and torques by current and energy perturbations from field computations - part I: theory and formulation," *IEEE Trans. on Energy Conversion*, vol. 14, no. 4, pp. 1507-1513, Dec. 1999. 60

[31] R. Escarela-Perez, E. Campero-Littlewood, M.A. Arjona-Lopez, A. Laureano-Cruces, "Comparison of two techniques for two-dimensional finite-element inductance computation of electrical machines," *IEE Proc. Electric Power Applications*, vol. 152, no. 4, pp. 855-861, July 2005. 60, 64

[32] F. Poltschak, W. Amrhein, "A dynamic nonlinear model for permanent magnet synchronous machines," *IEEE Int. Symposium on Industrial Electronics (ISIE 2008)*, pp. 724-729, July 2008. 8, 28, 61, 72

[33] O. A. Mohammed, S. Liu, Z. Liu, "Physical modeling of PM synchronous motors for integrated coupling with machine drives," *IEEE Trans. on Magnetics*, vol. 41, no. 5, pp. 1628-1631, May 2005. 28, 57

[34] O. A. Mohammed, S. Liu, Z. Liu, "A phase variable model of brushless dc motors based on finite element analysis and its coupling with external circuits," *IEEE Trans. on Magnetics*, vol. 41, no. 5, pp. 1576-1579, May 2005. 8, 28, 61

[35] E. Deng, N. A. Demerdash, "A coupled finite-element state-space approach for synchronous generators. I. model development," *IEEE Trans. on Aerospace and Electronic Systems*, vol. 32, no. 2, pp. 775-784, Apr. 1996. 8, 28, 61

[36] Y. Kano, K. Watanabe, T. Kosaka, N. Matsui, "A new modeling approach for circuit-field-coupled time-stepping electromagnetic analysis of saturated interior permanent magnet synchronous motors," *Electrical Engineering in Japan*, vol. 174 , no. 1, pp. 49-58, 2011. 60

[37] B. Stumberger, G. Stumberger, D. Dolinar, A. Hamler, M. Trlep, "Evaluation of saturation and cross-magnetization effects in interior permanent-magnet synchronous motor," *IEEE Trans. on Industry Applications*, vol. 39, no. 5, pp. 1264-1271, Sept.-Oct. 2003. 27, 55, 60

[38] J. R. Marti, K. W. Louie, "A phase-domain synchronous generator model including saturation effects," *IEEE Trans. on Power Systems*, vol. 12, no. 1, pp. 222-229, Feb. 1997.

[39] J. M. Stephenson, J. Corda, "Computation of torque and current in doubly salient reluctance motors from nonlinear magnetisation data," *Proc. of the Institution of Electrical Engineers*, vol. 126, no. 5, pp. 393-396, May 1979. 61

[40] H. L. Nakra, T. H. Barton, "The dynamics of coupled circuits with ferromagnetic non-linearity," *IEEE Trans. on Power Apparatus and Systems*, vol. PAS-90, no. 5, pp. 2349-2358, Sept. 1971. 62

[41] Y. Terao, M. Sekino, H. Ohsaki, "Short-circuit characteristic analysis of 10 MW class superconducting wind turbine generators," *Proc. ICEC24 - ICMC2012*, Fukuoka (Japan), May 14-18 2012.

[42] C. Meyer, M. Hoing, A. Peterson, R.W. De Doncker, "Control and design of DC grids for offshore wind farms," *IEEE Trans. on Industry Applications*, vol. 43, no. 6, 2007, pp. 1475-1482. 6

[43] N. Flourentzou, V.G. Agelidis, G.D. Demetriades, "VSC-based HVDC power transmission systems: an overview", *IEEE Trans. on Power Electronics*, vol. 24, no. 3, 2009, pp. 592-602. 6, 24

[44] L. Xu, B.R. Andersen, "Grid connection of large offshore wind farms using HVDC," *Wind Energ.*, vol. 9, no. 4, 2006, pp. 371-382. 6, 23, 24

[45] W. Lu, B.T. Ooi, "Optimal acquisition and aggregation of offshore wind power by multiterminal voltage-source HVDC," *IEEE Trans. on Power Delivery*, vol. 18, no. 1, 2003, pp. 201-206. 24

[46] D. Jovcic, "Offshore wind farm with a series multiterminal CSI HVDC," *Electric Power Systems Research*, vol. 78, no. 4, 2008, pp. 747-755. 24

[47] C. Lewis, J. Muller, "A direct drive wind turbine HTS generator," *IEEE Power Engineering Society General Meeting*, 24-28 June 2007, pp. 1-8. 3, 4, 5, 12

[48] G.-H. Kim, N. Kim, K.-M. Kim, M. Park, I.-K. Yu, S. Lee, T.-J. Park, "EMTDC based simulation of 10 MW class grid-connected superconducting wind turbine generator," *IEEE Trans. on Applied Superconductivity*, vol. 22, no. 3, 2012. 4, 5

[49] N. Mijatovic, A.B. Abrahamsen, C. Traeholt, E. Seiler, M. Henriksen, V.M. Rodriguez-Zermeno, N.F. Pederson, "Superconducting generators for wind turbines: design considerations," *J. Phys.: Conf. Ser.*, vol. 234, 2010. 5, 12, 15, 18

[50] K. Sivasubramaniam, X. Huang, E.T. Laskaris, T. Zhang, J.W. Bray, J.M. Forgarty, R.A. Nold, "Performance of an HTS generator field coil under system fault conditions," *IEEE Trans. on Applied Superconductivity*, vol. 16, no. 4, 2006, pp. 1971- 1975. 5, 13

[51] T.M. Flynn, "Cryogenic Engineering," CRC Press, Boca Raton, FL, 2005. 12

[52] "Grid Code: High and extra high voltage," E. On Netz GmbH Std., Sept. 2006. 23, 94

[53] "Grid Code: Requirements for offshore grid connections in the E.ON Netz network," E. On Netz GmbH Std., Apr. 2008. 23

[54] D. Finney, "Variable frequency AC motor drive systems," IET, 1988. 13, 21

[55] H. Ohsaki, Y. Terao, R. M. Quddes, M. Sekino, "Electromagnetic characteristics of 10 MW class superconducting wind turbine generators," *Proc. Int. Conf. on Electrical Machines and Systems (ICEMS2010)*, pp. 1303-1306, 10-13 Oct. 2010. 4, 14, 16, 18, 19, 28, 98

[56] A.B. Abrahamsen, N. Mijatovic, E. Seiler, T. Zirngibl, C. Traeholt, P.B. Norgard, N.F. Pederson, N.H.Andersen, J. Ostergard, "Superconducting wind turbine generators," *Superconductor Science and Technology*, vol. 23, no. 3, 2010. 3, 4, 14, 16, 18

[57] K. Sivasubramaniam, X. Huang, D. Ryan, K. Weeber, J.W. Bray, E.T. Laskaris, L. Tomaino, J.M. Fogarty, S. Ashworth, "AC losses in a high temperature superconducting generator," *IEEE Trans. on Applied Superconductivity*, vol. 15, no. 2, 2005, pp. 2162- 2165. 5, 12

[58] Z. Hong, T.A. Coombs, "Numerical modelling of AC loss in coated conductors by finite element software using H formulation," *Journal of Superconductivity and Novel Magnetism*, vol. 23, no. 8, 2010, pp. 1551- 1562. 6, 86

[59] V.M. Rodriguez-Zermeno, N. Mijatovic, C. Traeholt, T. Zirngibl, E. Seiler, A. B. Abrahamsen, N. F. Pedersen, M.P. Sorensen, "Towards faster FEM simulation of thin film superconductors: a multiscale approach," *IEEE Trans. on Applied Superconductivity*, vol. 21, no. 3, 2011, pp. 3273- 3276. 6, 29, 85

[60] J.R. Clem, J.H. Claassen, Y. Mawatari, "AC losses in a finite Z stack using an anisotropic homogeneous-medium approximation," *Superconductor Science and Technology*, vol. 20, no. 12, pp. 1130-1139, 2007. 6

[61] L. Prigozhin, V. Sokolovsky, "Computing AC losses in stacks of high-temperature superconducting tapes," *Superconductor Science and Technology*, vol. 24, no. 7, pp. 075012-12. 6, 86

[62] Z. Chen, J.M. Guerrero, F. Blaabjerg, "A review of the state of the art of power electronics for wind turbines," IEEE Trans. on Power Electronics, vol. 24, no. 8, 2009, pp. 1859-1875. 6

[63] D.W. Hazelton, "2G HTS Applications Developments," *Symposium on Superconducting Devices for Wind Energy*, Feb. 25, 2011, Barcelona, Spain. 29, 99, 103

[64] M. Zhang, J.-H. Kim, S. Pamidi, M. Chudy, W. Yuan, T.A. Coombs, "Study of second generation, high-temperature superconducting coils: Determination of critical current," *Journal of Applied Physics*, vol. 111, no. 8, 2012, pp. 083902-8. 29, 85

[65] F. Grilli, S.P. Ashworth, "Measuring transport AC losses in YBCO-coated conductor coils," *Superconductor Science and Technology*, vol. 20, no. 6, 2007, pp. 794-799. 29

[66] P.C. Krause, O. Wasynczuk, S.D. Sudhoff, *Analysis of electric machinery and drive systems*, IEEE Press, 2002. 27, 32, 38, 40, 41, 53, 54, 55, 56, 102

[67] V.M. Rodriguez-Zermeno, A. Abrahamsen, N. Mijatovic, M.P. Sorensen, B.B. Jensen, N.F. Pedersen, "Simulation of an HTS synchronous superconducting generator," *Physics Procedia*, vol. 36, pp. 786-790, 2012. 6, 32

[68] N. Maki, T. Takao, S. Fuchino, H. Hiwasa, M. Hirakawa, K. Okumura, M. Asada, R. Takahashi, "Study of practical applications of HTS synchronous machines," *IEEE Trans. on Applied Superconductivity*, vol. 15, no. 2, 2005, pp. 2166-2169. 3

[69] S.S. Kalsi, K. Weeber, H. Takesue, C. Lewis, H.W. Neumueller, R.D. Blaugher, "Development status of rotating machines employing superconducting field windings," *Proc. IEEE 92*, 2004, p. 1688. 3

[70] S.M. Muyeen, R. Takahashi, T. Murata, J. Tamura, M.H. Ali, "Transient stability analysis of permanent magnet variable speed synchronous wind generator," *Proc. Int. Conf. on Electrical Machines and Systems (ICEMS2007)*, pp. 288-293, 2007.

[71] S.M. Muyeen, M.H. Ali, R. Takahashi, T. Murata, J. Tamura, Y. Tomaki, A. Sakahara, E. Sasano "Comparative study on transient stability analysis

of wind turbine generator system using different drive train models," *IET Renewable Power Generation*, vol. 1(2), pp. 131-141, 2007. 25

[72] Z. Q. Zhu, Z.P. Xia, L. J. Wu, G.W. Jewell, "Analytical modelling and finite element computation of radial vibration force in fractional slot permanent magnet brushless machines," *IEEE Int. Electric Machines and Drives Conf. (IEMDC2009)*, Florida USA, May 3-6, 2009, pp.157-164. 17

[73] K. Yamazaki, H. Ishigami, "Rotor-shape optimization of interior-permanent-magnet motors to reduce harmonic iron losses," *IEEE Trans. on Industrial Electronics*, vol. 57, no. 1, pp. 61-69, 2010. 17

[74] J. Wang, Z.P. Xia, D. Howe, S.A. Long, Comparative study of 3-phase permanent magnet brushless machines with concentrated, distributed and modular windings," *3rd IET Int. Conf. on Power Electronics, Machines and Drives*, pp. 489-493, 2006. 17

[75] G. Dajaku, D. Gerling, "Different novel methods for reduction of low space harmonics for the fractional slot concentrated windings." *Proc. 15th Int. Conf. on Electrical Machines and Systems (ICEMS2012)*, 2012. 17

[76] Y. Terao, M. Sekino, H. Ohsaki, "Comparison of conventional and superconducting generator concepts for offshore wind turbines," *Proc. 2012 Applied Superconductivity Conference (ASC2012)*, Portland, USA, 2012. ix, 3, 4, 16, 18, 20, 28, 80, 101

[77] A. Doi, S. Kim, "Fundamental study on conceptual design for medium class superconducting synchronous motor," *Abstracts of CSJ Conference*, vol. 85, p. 124, 2011. 18

[78] J.R. Bumby, "Superconducting rotating electrical machines," Clarendon press, Oxford, 1983. 18

[79] M.R. Quddes, M. Sekino, H. Ohsaki, N. Kashima, S. Nagaya, "Electromagnetic design study of transverse flux enhanced type superconducting wind turbine generators," *IEEE Trans. on Applied Superconductivity*, vol. 21, no. 3, pp. 1101-1104, 2011. 19

[80] H. Ohsaki, Y. Terao, M. Sekino, "Wind turbine generator using superconducting coils and bulks," *J. Phys.: Conf. Ser.*, vol. 234, part. 3, 2010. 19

[81] G. Klaus, M. Wilke, J. Frauenhofer, W. Nick, H.W. Neumuller, "Design challenges and benefits of HTS synchronous machines," *IEEE PES General Meeting*, Tampa, USA, 2007. 4

[82] B. Lukasik, K.F. Goddard, J.K. Sykulski, "Finite element assisted method of estimating equivalent circuit parameters for a superconducting synchronous generator with a coreless rotor," *IEEE Trans. on Applied Superconductivity*, vol. 45, no. 3, 2009. 4

[83] J. Frauenhofer, J. Grundmann, G. Klaus, W. Nick, "Basic concepts, status, opportunities and challenges of electrical machines utilizing high-temperature superconducting windings," *Journal of Physics, Conference Series 97*, 2008. 4

[84] A.J. Forsyth, , C. Jia, D. Wu, C.H. Tan, S. Dimler, Y. Yang, W. Bailey, "Cryogenic converter for superconducting coil control," *Power Electronics, IET*, vol. 5, no. 6, pp. 739-746, 2012. 22, 99, 102

[85] M. Popescu, "Prediction of the electromagnetic torque in synchronous machines through Maxwell stress harmonic filter (HFT) method," *Electrical Engineering (Archiv fur Elektrotechnik)*, vol. 89, no. 2, pp. 117-125, 2006. 65

[86] N. Sadowski, Y. Lefevre, M. Lajoie-Mazenc, J. Cros, "Finite element torque calculation in electrical machines while considering the mouvement," *IEEE Trans. on Magnetics*, vol. 28, no. 2, pp. 1410-1413, 1992. 65

[87] J.P.A. Bastos, N. Sadowski, "Electromagnetic modeling by finite element methods," CRC press, 2003. 65

[88] D.A. Lowther, P.P. Silvester, "Computer-aided design in magnetics," Springer-Verlag New York, 1986. 64

[89] L. Chang, "An improved FE inductance calculation for electrical machines," *IEEE Trans. on Magnetics*, vol. 32, no. 4, pp. 3237-3245, Jul. 1996. 64

[90] M.D. Ainslie, V.M. Rodriguez-Zermeno, Z. Hong, W. Yuan, T.J. Flack, T.A. Coombs, "An improved FEM model for computing transport AC loss in coils made of RABiTS YBCO coated conductors for electric machines," *Supercond. Sci. Technol.*, vol. 24, no. 4, pp. 5005-8, 2011. 87

[91] Z. Hong, W. Yuan, M. Ainslie, Y. Yan, R. Pei, T.A. Coombs, "AC losses of superconducting racetrack coil in various magnetic conditions," *IEEE Trans. on Applied Superconductivity*, vol. 21, no. 3, pp. 2466-2469, 2011. 82

[92] V. Lahtinen, A. Stenvall, "The difficulty of modeling ripple field losses in superconductors using the eddy current model," *IEEE Trans. on Applied Superconductivity*, vol. 23, no. 3, pp. 4900505+5, 2013. 82

[93] T. Hamajima, S. Hanai, Y. Wachi, M. Kyoto, M. Shimada, M. Ono, K. Shimada, L. Kushida, M. Tezukab, N. Martovetsky, J. Zbasnik, J. Moller, N. Hirano, K. Shinoda, M. Yamamoto, I. Takano, T. Himeno, T. Satow, "Test results of the 100 kWh SMES model coilAC loss performance," *Cryogenics*, vol. 39, no. 11, pp. 947-953, 1999. 82

[94] A.P. Verweij, "Modelling boundary-induced coupling currents in Rutherford-type cables," *IEEE Trans. onApplied Superconductivity*,vol. 7, no. 2, pp. 723-726, 1997. 82

[95] A.K. Ghosh, K.E. Robins, W.B. Sampson, "The ramp rate dependence of the sextupole field in superconducting dipoles," IEEE Trans. onMagnetics, vol. 30, no. 4, pp. 1718-1721, 1994. 82

[96] E.H. Brandt, "Universality of flux creep in superconductors with arbitrary shape and current-voltage law," *Physical review letters*, vol. 76, no. 21pp. 4030-4033, 1996. 82

[97] N. Magnusson, "Semi-empirical model of the losses in HTS tapes carrying AC currents in AC magnetic fields applied parallel to the tape face," *Physica C: Superconductivity*, vol. 349, no. 3, pp. 225-234, 2001. 84

[98] N. Schoenborg, S. Hoernfeldt, "Losses in a high-temperature superconductor exposed to AC and DC transport currents and magnetic fields," *IEEE Trans. on Applied Superconductivity*, vol. 11, no. 3, pp. 4086-4090, 2001. 84

[99] M. Iwakuma, *et al.*, "AC loss properties of a 1MVA single-phase HTS power transformer," *IEEE Trans. on Applied Superconductivity*, vol. 11, no. 1, pp. 1303-1306, 2001. 86